Transverse Slot Antenna with a Stepped Groove Gap Waveguide Feeding Network

Amirmohammad Chitsaz

A Thesis

In the Department

Of

Electrical and Computer Engineering

Presented in Partial Fulfillment of the Requirements

For the Degree of

Master in Applied Science (Electrical and Computer Engineering) at

Concordia University

Montreal, Quebec, Canada

July 2025

© Amirmohammad Chitsaz 2025

CONCORDIA UNIVERSITY

SCHOOL OF GRADUATE STUDIES

This is to certify that the thesis prepared

By: Amirmohammad Chitsaz

Entitled: Transverse Slot Antenna with a Stepped Groove Gap Waveguide Feeding Network and submitted in partial fulfillment of the requirements for the degree of

Master of Applied Science (Electrical and Computer Engineering)

Complies with the regulations of this University and meets the accepted standards with respect to originality and quality.

gned by the i	inal examining committee:	
		_ Chair
Dr. Ahı	med A. Kishk	
		_Examiner
Dr. Chr	ristopher W. Trueman	
		Examiner
Dr. Ahı	med A. Kishk	
		_Supervisor
Dr. Abo	del Razik Sebak	
proved by:		
	Dr. Abdelwahab Hamou-Lhadj,	
	Chair of Department of Electrical and Computer	Engineering
aly 21, 2025		_
	Dr. Mourad Debbabi	
	Dean of Gina Cody School of Engineering and Cor	nputer Science

Abstract

Transverse Slot Antenna with a Stepped Groove Gap Waveguide Feeding Network

Amirmohammad Chitsaz

Concordia University

This thesis investigates the performance enhancement of transverse slot antennas using Groove Gap Waveguide technology. It focuses on improving bandwidth, gain, and radiation characteristics for modern wireless communication systems, particularly in the sub-6 GHz and millimeter-wave bands for 5G and beyond. The study begins with a comprehensive review of GGW technology, Electromagnetic Band Gap structures, and slotted antenna designs, highlighting their significance in overcoming challenges such as high path loss, limited penetration, and narrow bandwidth in high-frequency applications.

A simple single GGW slotted antenna is designed and analyzed, operating in the 3.1–4.6 GHz range with an impedance bandwidth of 38%, achieving a highest gain of 7 dBi. To enhance performance, rectangular corrugations are incorporated into the top layer, extending the matching impedance bandwidth to 54% and a highest gain of 10.3 dBi is achieved by introducing a step under the slot at the GGW-to-slot transition, resulting in a remarkable 77% impedance bandwidth while maintaining a gain of 10.3 dBi. The measurement results closely align with simulations, demonstrating a 73% matching impedance bandwidth. The scalability of the stepped design is also explored, showing that the 77% impedance bandwidth is preserved when scaled to center frequencies of 30 GHz and 60 GHz, making it highly suitable for mm-wave applications.

Simulations using CST Studio and HFSS validate the designs, with detailed analyses of S_{11} , gain, radiation patterns, and E-field distributions. The results underscore the effectiveness of GGW technology, EBG structures, corrugations, and steps in addressing the limitations of traditional slotted antennas, offering a robust solution for wideband, high-gain antennas in next-generation wireless networks. This research contributes to advancing antenna design for 5G, radar, and satellite communications, providing a foundation for future developments in scalable, high-frequency antenna systems.

Table of Contents

Chapter I	: Introduction 1
1.1.	Sub-6GHz band and Applications1
1.2.	Motivations and Problem Statement2
1.3.	Objectives3
1.4.	Methodology4
1.5.	Overview of Thesis 6
Chapter I	I: Literature Review 7
2.1.	Groove Gap Waveguide (GGW)7
2.2.	Slotted Antennas12
2.3.	Corrugations15
2.4.	Coaxial to GGW Transition16
Chapter I	II: Design and Simulation of GGW using EBG18
3.1.	Introduction18
3.2.	Unit Cell EBG19
3.3.	GGW Design26
3.4.	Vertical Transition from Coaxial Cable to GGW:35
Chapter I	V: Transverse Slot Antenna Based on GGW47
4.1.	Introduction47
4.2.	Design and Analysis of a Simple Single-Groove Gap Waveguide Slotted Antenna48
4.3.	Design and Analysis of a Groove Gap Waveguide Slotted Antenna with Rectangular
Corrug	ations51
	Design and Analysis of a Groove Gap Waveguide Slotted Antenna with a Step Under the
4.5.	Comparison of Simple, Corrugated, and Stepped GGW Slotted Antennas57

4.6.	Prototyping and Measurement Results	59
4.7.	Design and Analysis of a 1x4 GGW Slotted Antenna Array with Stepped Design	66
4.8.	Scaling Analysis for Higher Frequencies	69
4.9.	Conclusion	71
Chaptei	· V: Conclusion and Future Works	73
5.1.	Conclusion	73
5.2.	Future Works	74
Referen	ces	75

Table of Figures

Figure 1.1. The heterogeneous mm-Wave and sub-6GHz network [2]
Figure 2.1. Artificially Soft and Hard Surface [18]
Figure 3.1. Groove gap waveguide using metal pins EBG
Figure 3.2. Metal Pin EBG Structure
Figure 3.3. EBG Dispersion Diagram
Figure 3.4. Dispersion Diagram, Effect of Air Gap size reduction a) ag=0.588 mm, b) ag=3 mm,
and c) ag=5.88 mm
Figure 3.5. Dispersion Diagram, Effect of Cell Size reduction a) p=14.7 mm, b) p=12.25 mm,
and c) p=10.4 mm
Figure 3.6. Dispersion Diagram, Effect of Pin Size reduction a) a=5.8 mm, b) a=4.8 mm, and c)
a=3.8 mm
Figure 3.7. Dispersion Diagram, Effect of Pin Height Reduction: a) $d=14.7$ mm, b) $d=15.8$ mm,
and c) d=16.9 mm
Figure 3.8. Various shapes of Nails: a) Cylindrical, b) Octagonal, and c) Square
Figure 3.9. Dispersion Diagram, Different Shapes: a) Square, b) Cylindrical, and c) Octagonal 25
Figure 3.10. Groove Gap Waveguide: a) Front View, b) Perspective View
Figure 3.12. GGW Unit Cell
Figure 3.11. Eigenmode Solver Modes and EBG Stopband a) w=62 mm, b) w=58 mm, and c)
w=52 mm
Figure 3.13. Modes of Electric Field Distribution a) Mode 5, b) Mode 6, and c) Mode 7 29
Figure 3.14. Electric Field Distribution a) From the port b) Field Distribution along GGW (Top
layer is hidden)
Figure 3.15. GGW Field Distribution from 2 to 10 GHz (Top view)
Figure 3.16. Simulated (a) RWG and (b) GGW with the boundary conditions in the Eigenmode
Solver
Figure 3.17. Propagation Constant of an RWG
Figure 3.18 Propagation Constant of a GGW

Figure 3.19. 3D schematic of the transition structure (a) removed-top-layer view and (b) cross-	
sectional view	36
Figure 3.20. Port Electric Field Distribution (a) Coaxial and (b) GGW port	37
Figure 3.21. S-parameter plot showing S11 and S21 over frequency	39
Figure 3.22. Electromagnetic Field Distribution	39
Figure 3.23. S11 of Sweep Parameter d1	‡ 1
Figure 3.24. S11 of Sweep Parameter lp	12
Figure 3.25. S11 of Sweep Parameters h1 & h2	14
Figure 3.26. S11 of Sweep Parameters d2, lg & dg	16
Figure 4.1. (a) Simulated 3D of the GGW slotted antenna, (b) Cross-sectional view, and (c) S11	,
Gain, and the front-to-back ratio of the antenna	50
Figure 4.2. Cross-Sectional View of the Corrugated antenna	51
Figure 4.3. S11 and gain of the slotted GGW antenna.	52
Figure 4.4. Simulated Results of Corrugated Antenna: polar radiation pattern at (a) $\phi=0^\circ$ and	
(b) $\phi = 90^{\circ}$ at different frequencies. (c) E-Field distribution at 3.9 GHz	53
Figure 4.5. Top view of the stepped GGW slotted antenna (Top layer is hidden)	55
Figure 4.6.Cross-sectional view of the GGW slotted antenna with a step under the slot	55
Figure 4.7.Simulated performance of the GGW slotted antenna with a step under the slot: S11	
(black), and gain (red) over the 3-8 GHz range	56
Figure 4.8. E-field distribution at 3.28 GHz for the stepped GGW slotted antenna with a step	
under the slot.	57
Figure 4.9. Comparison of Simple, Corrugated, and Stepped GGW Slotted Antennas	58
Figure 4.10. The Prototyped Antenna: (a) Top View (b) Bottom View (c) Side View (d)	
Disassembled Antenna	50
Figure 4.11. (a) Comparison of measured (blue line) and simulated (red line) S11 (b) The far-	
field setup of the radiation pattern measurement.	52
Figure 4.12. Comparison of Measurement and Simulation of E-Plane pattern at (a) 3.25 GHz, (b))
5 GHz, and (c) 7.25 GHz.	54
Figure 4.13. Comparison of Measurement and Simulation of H-Plane pattern at (a) 3.25 GHz, (o)
5 GHz, and (c) 7.25 GHz.	55
Figure 4.14.Simulated 1x4 array antenna a) Perspective view b) top view (hidden top layer)	57

Figure 4.15. Active Reflection Coefficient and Gain versus frequency for the 1x4 Stepped GGV	V
slot antenna simulated in CST	58
Figure 4.16. S11 of the scaled GGW slotted antenna with a step under the slot, comparing b)	
scaling factors of 0.17 (red, 30 GHz center frequency) and c) 0.085 (black, 60 GHz center	
frequency), demonstrating invariant 77% impedance matching bandwidth	70
Figure 4.17. Active Reflection Coefficient and Gain versus frequency for the scaled 1x4 Steppe	d
GGW slot antenna simulated in CST	71

List of Tables

Table 3.1. GGW and RGW Dimensions.	34
Table 3.2. Coax-to-GGW transition dimensions	38
Table 4.1. Transverse slotted GGW antenna dimensions (Figure 4.1)	49
Table 4.2. Corrugation Dimensions	51
Table 4.3. The dimensions of the Prototyped Antenna	59
Table 4.4. Comparative results of Measured, Simulated (CST) Single Slot and 1x4 Array	
Antenna	69

Abbreviations

1D One-Dimensional 2D Two-Dimensional 3D Three-Dimensional 5G Fifth Generation 6G Sixth Generation **AMC** Artificial Magnetic Conductor AUT Antenna Under Test BWBandwidth CMM Coordinate Measuring Machine **CNC** Computer Numerical Control CST Computer Simulation Technology EBG Electromagnetic Band Gap ECAL **Electronic Calibration** EM Electromagnetic FEM Finite Element Method **GGW** Groove Gap Waveguide **HFSS** High Frequency Structure Simulator IOT **Internet Of Things** MIMO Multi-Input Multi-Output PEC Perfect Electric Conductor PMC Perfect Magnetic Conductor PNA Programmable Network Analyzer **RWG** Rectangular Waveguide SMA Subminiature Version A **SOLT** Short Open Load Through TE Transverse Electric Wave TEM Transverse Electromagnetic Wave TM Transverse Magnetic Wave

Vector Network Analyzer

VNA

Chapter I:

Introduction

1.1. Sub-6GHz band and Applications

Sub-6GHz bands and millimeter-wave (MMW) are essential in advancing wireless communication technologies, especially in 5G and beyond. The mm-wave band, typically operating at frequencies above 24 GHz, offers a significant bandwidth, which is crucial for supporting the high data rates and large-scale connectivity required by modern applications. However, mm-wave signals encounter major challenges, such as high path loss and limited penetration abilities, requiring advanced methods like beamforming and the deployment of dense small cell networks to ensure sufficient coverage and performance [1], [2], [3].

Conversely, the sub-6GHz band, which includes frequencies below 6 GHz, is characterized by better propagation characteristics, including lower path loss and better penetration through obstacles. This makes it ideal for providing reliable coverage over larger areas and supporting mobility.

The coexistence and integration of sub-6GHz and mm-wave bands are essential for achieving the desired balance between coverage and capacity in next-generation networks. Techniques such as hybrid beamforming leverage the spatial similarities between these bands to enhance system performance and reduce overhead costs [2], [4], [5].

The integration of these bands is crucial for enhancing the performance of 5G networks and paving the way for future 6G networks. This integration allows for the development of compact, dual-function antennas and advanced network architectures that can dynamically allocate resources based on user demand and network conditions [3], [6], [7]. As the demand for higher data rates and more reliable connections continues to grow, the strategic use of both mm-wave and sub-6GHz

bands will be instrumental in meeting these challenges and driving the evolution of wireless communication technologies.

This thesis focuses on developing transverse slot antennas using Groove Gap Waveguide (GGW) technology, primarily for use in advanced wireless communication systems. These antennas are designed to operate in the sub-6 GHz and MMW frequency bands, addressing essential needs in 5G networks, radar systems, and satellite communications. The designs aim to improve bandwidth,

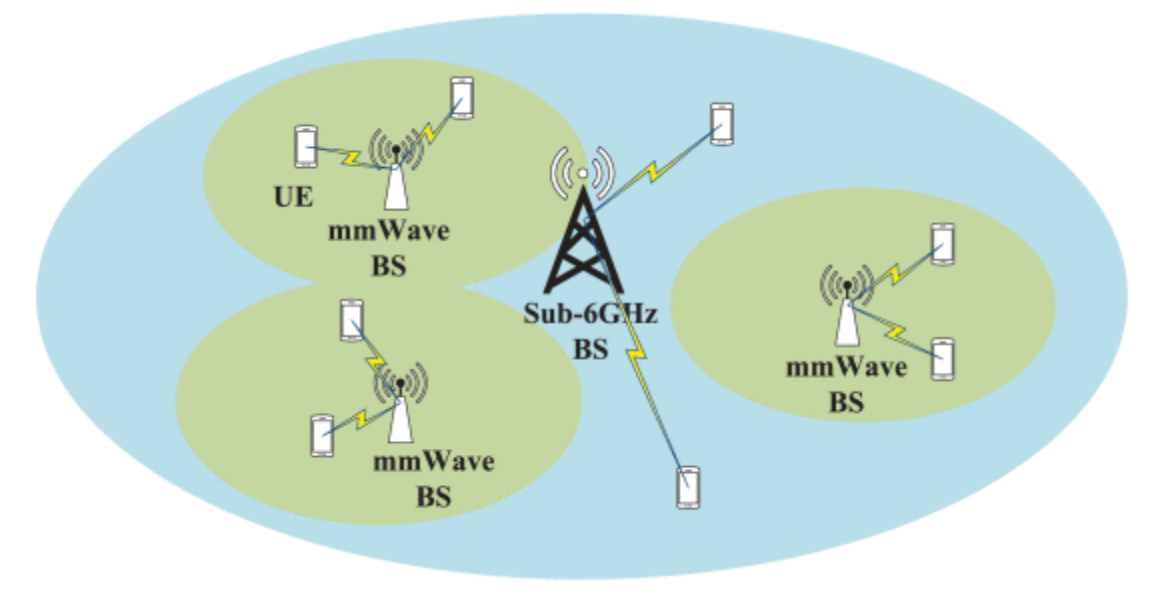


Figure 1.1. The heterogeneous mm-Wave and sub-6GHz network [2]

increase gain, and optimize radiation patterns, making them suitable for high-data-rate applications, dense urban network deployments, and scalable MMW systems vital for future-proof communication infrastructure. Furthermore, the technology has potential for integration into automotive radar for autonomous vehicles, aerospace navigation systems, and emerging Internet of Things (IoT) platforms, where compact, high-performance antennas are becoming increasingly important.

1.2. Motivations and Problem Statement

The rapid advancement of wireless communication technologies, particularly the deployment of 5G networks, necessitates the development of antennas with enhanced performance characteristics, such as increased bandwidth, higher gain, and improved radiation efficiency. The sub-6 GHz frequency band is exciting due to its favorable propagation characteristics and widespread use in mobile communications. However, achieving optimal performance in this band presents several challenges, including managing sidelobe levels, minimizing grating lobes, and

enhancing bandwidth and gain. These challenges are compounded by issues related to scalability, cost-effectiveness, and precise control over electromagnetic field distributions, which are critical for modern systems such as 5G networks, satellite communications, and radar.

Recent studies have demonstrated the potential of GGW technology in addressing these challenges. For instance, using corrugations in GGW has effectively reduced sidelobes and enhanced radiation efficiency by suppressing grating lobes, as evidenced by the development of compact slot array antennas with improved gain and sidelobe levels [8]. Additionally, GGW technology has been successfully applied in multibeam antennas to achieve high gain and radiation efficiency, further underscoring its suitability for advanced antenna designs [9].

Moreover, the integration of innovative feeding networks, such as those based on ridge gap waveguides, has been shown to enhance bandwidth and gain significantly in various antenna configurations. These networks provide low-loss pathways and enable efficient power distribution, critical for achieving the desired performance enhancements in slotted antennas [10], [11].

In this context, the proposed thesis explores groove gap waveguide feeding networks in conjunction with corrugations to enhance the performance of linear polarized sub-6 GHz slotted antennas. By leveraging the unique properties of GGW technology, the research seeks to address the existing limitations in antenna design and contribute to developing high-performance antennas for next-generation wireless communication systems.

Moreover, integrating innovative features like corrugations and stepped structures into antenna designs, while promising, introduces complexities in fabrication and performance consistency. Current designs often suffer from suboptimal sidelobe levels, reduced directivity, and sensitivity to manufacturing tolerances, which can degrade overall system reliability. This gap in achieving a balance between theoretical performance and practical implementation underscores the need for a systematic approach to designing and validating GGW slotted antennas with enhanced characteristics to meet the evolving requirements of next-generation wireless technologies.

1.3. Objectives

The primary aim of this thesis is to design, build, and assess simple, corrugated, and stepped GGW slotted antennas to improve bandwidth and radiation qualities. This involves developing innovative antenna structures that can effectively operate within the 3–8 GHz range, addressing

the limitations of traditional designs by adding novel features like corrugations and stepped configurations to boost performance. A key focus is to validate the simulated performance of these antennas through thorough experimental measurements, ensuring that the theoretical improvements are practical. This includes examining their reflection coefficients and radiation patterns to confirm enhanced performance metrics, while also noting any discrepancies that might occur due to manufacturing tolerances or environmental factors, providing a comprehensive evaluation of their real-world potential. Additionally, the study aims to assess the suitability of these antennas for actual deployment in advanced communication systems such as 5G and radar, offering insights into their manufacturability and scalability for future uses. This involves exploring the feasibility of mass production methods, analyzing cost-effectiveness, and considering their adaptability to higher frequency bands, such as MMW ranges, to meet emerging technological demands in telecommunications. Furthermore, the research intends to contribute to the wider field of antenna engineering by establishing a solid framework for designing and testing GGW-based antennas. This includes documenting the challenges faced during design and fabrication, proposing solutions to overcome these hurdles, and laying the groundwork for future versions that might incorporate advanced materials or hybrid designs to optimize performance further.

1.4. Methodology

The research methodology outlines a systematic approach to designing, simulating, fabricating, and experimentally validating the proposed GGW slotted antenna structures. This process integrates computational tools, precision manufacturing, and rigorous testing to achieve a robust antenna design.

Simulation

The design process begins with the development of an Electromagnetic Bandgap (EBG) cell, leveraging insights from previous works and their semi-analytical expressions. This initial EBG cell is optimized using CST Studio's Eigen mode solver, configured with a periodic or unit cell boundary box within the Brillouin Zone. This setup enables the determination of a suitable electromagnetic field configuration that confines waves within the desired frequency band, ensuring effective bandgap properties.

Next, the GGW is designed to feed the slot antenna, utilizing the optimized EBG cells as its foundation. This step employs CST's frequency solver with an open and Perfect Electric Conductor (PEC) boundary box to accurately model the waveguide's electromagnetic behaviour and its interaction with the slot. Following this, the slot antenna is independently studied and simulated in an open-space environment to evaluate its radiation characteristics and performance.

To enhance the reliability of the simulation results, the entire antenna structure—comprising the EBG cells, GGW, and slot—is verified using HFSS, a second computational tool. This cross-verification step ensures consistency between the two software platforms and increases confidence in the design before prototyping.

Fabrication

The antenna is fabricated using high-precision CNC milling techniques, with aluminum chosen as the material for its excellent conductivity, lightweight properties, and suitability for high-frequency applications. The fabrication process meticulously shapes the EBG pins, grooves, slots, and other structural features, adhering to the simulated design specifications. Quality control is maintained through inspections using a coordinate measuring machine (CMM) to verify dimensional accuracy.

Experimental Validation

After prototyping, the antenna undergoes experimental validation in a state-of-the-art anechoic chamber. A Vector Network Analyzer (VNA) is used to measure the reflection coefficients across the operating frequency range of 3–8 GHz, providing insight into the antenna's impedance matching. Additionally, the radiation patterns are recorded, capturing the co-polar and cross-polar components of both the E-plane and H-plane. This measurement process employs standardized probe antennas and a motorized turntable to ensure precise and automated data collection. The experimental results are compared with the simulation outcomes to validate the design and identify any discrepancies introduced by real-world conditions.

This integrated methodology—spanning design, simulation, fabrication, and measurement—provides a comprehensive framework for evaluating the GGW slotted antenna's performance, bridging theoretical predictions with practical implementation.

1.5. Overview of Thesis

This thesis is structured to comprehensively explore GGW slotted antennas, progressing from theoretical foundations to practical implementation. Chapter 2, "Literature Review," examines the evolution and key principles of Electromagnetic Band Gap (EBG) structures, gap waveguides, and slotted antennas, comparing their designs, propagation characteristics, and applications. It also explores the impact of slot thickness and corrugations on performance. Chapter 3, "Design and Simulation of GGW using EBG," details the design process of GGW structures, including EBG unit cell optimization, mode analysis, and the development of a coaxial-to-GGW transition, supported by dispersion diagrams and field distribution studies using CST Studio and HFSS. Chapter 4, "Proposed Slot Antenna Based on GGW," presents the design, simulation, and analysis of simple, corrugated, and stepped GGW slotted antennas, including a 1x4 array configuration, with performance metrics such as impedance bandwidth, gain, and radiation patterns, validated through manufacturing and measurement results. Chapter 5, "Conclusion and Future Works," summarizes the findings on bandwidth and gain enhancements, reflecting on the scalability of the designs for 5G and radar applications, and proposes future research directions, including optimization and integration with advanced technologies.

Chapter II:

Literature Review

2.1. Groove Gap Waveguide (GGW)

This section delves into the fundamental principles governing the operation of Gap Waveguide structures. It begins with a historical overview and explores their diverse applications in various fields. Furthermore, it concisely summarizes the key characteristics of Groove Gap Waveguide structures, including their unique properties and limitations. Finally, it examines different types of element shapes and their impact on the performance of Gap Waveguide structures.

Gap waveguide technology has evolved significantly since its inception, primarily driven by the need for efficient MMW transmission systems. Initially, the focus was on overcoming the limitations of traditional waveguides, such as high losses and complex manufacturing processes. The introduction of electromagnetic bandgap (EBG) structures, particularly those with glide-symmetric designs, marked a significant advancement in this field. These structures have been instrumental in reducing manufacturing costs and improving performance at high frequencies [12], [13], [14].

Gap waveguides are utilized in various applications, including antennas and circuits for MMW bands, crucial for next-generation wireless communication and radar systems. They offer robust solutions for signal transmission, even in the presence of defects and bends, making them suitable for automotive radar, 5G communication, and synthetic-aperture radar for imaging [15]. Additionally, their integration with classical transmission lines enhances their applicability in diverse electromagnetic applications [15], [16].

Groove gap waveguide (GGW) structures are characterized by their ability to confine electromagnetic waves within a groove, effectively creating a stopband that prevents wave

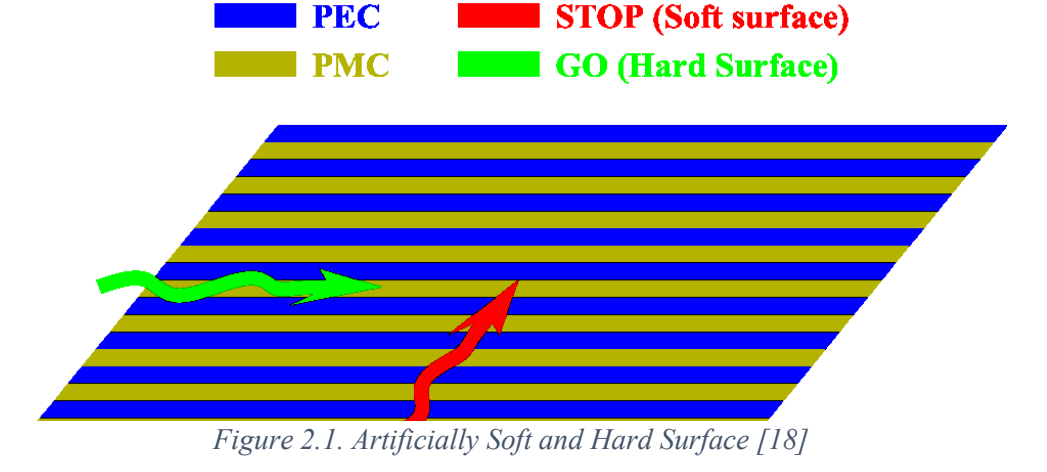
propagation outside the desired path. This is achieved through the use of periodic structures, such as glide-symmetric holey designs, which enhance the waveguide's performance by reducing losses and improving transmission efficiency [12], [14], [17]. However, these structures can be sensitive to fabrication errors, which may impact their performance [15].

The unique properties of GGW structures include their high structural strength and tunable stopband frequencies, which are advantageous for high-frequency applications. Glide-symmetric designs allow for larger periodicity, leading to higher accuracy and easier manufacturing processes [12], [17]. Despite these advantages, challenges such as reflection and scattering losses at sharp bends remain, necessitating innovative design solutions to mitigate these issues [15].

The shape of elements within gap waveguide structures significantly influences their performance. For instance, glide-symmetric holey structures can be implemented in one or two dimensions, affecting the dispersion and bandgap properties. A 1D glide symmetry is often sufficient for practical applications, while a 2D glide symmetry may be required for greater attenuation of lateral waves [18]. Additionally, using different element shapes, such as petal-shaped scatterers, can enhance vibration isolation and expand the bandgap width, offering new insights into waveguide design [19].

Artificially Soft and Hard Surfaces

Artificially soft and hard surfaces are engineered to control electromagnetic wave propagation [20], as shown in Figure 2.1. Soft surfaces, such as transversely corrugated surfaces, suppress surface wave propagation, making them useful in applications like patch antennas to improve radiation patterns by reducing edge diffraction [21], [22]. Hard surfaces, characterized by



8

longitudinal corrugations filled with dielectric material, are designed to support strong radiation fields along the surface for any polarization [22]. These surfaces are advantageous due to their polarization-independent reflection coefficients, maintaining the polarization state of circularly polarized waves upon reflection [22].

Periodic Structures (Electromagnetic Band Gap)

Periodic structures, such as Electromagnetic Band Gap (EBG), have garnered significant [20] attention due to their unique ability to manipulate electromagnetic waves. These structures exhibit fascinating properties, including frequency stop bands, passbands, and band gaps, which make them highly applicable in various technological domains. EBG structures are particularly valuable in antenna engineering, where they enhance antenna performance by suppressing surface wave propagation, thereby reducing mutual coupling and improving directivity and bandwidth [23], [24].

The versatility of EBG structures extends to numerous applications, including filter designs, frequency-selective surfaces, and photonic crystals [25], [26]. In antenna arrays, EBG structures can achieve significant mutual coupling reduction, which is crucial for maintaining high performance in compact designs [23], [27]. Additionally, EBG structures are employed in waveguide technologies, offering cost-effective solutions with improved accuracy and manufacturing ease [12].

Moreover, EBG structures are instrumental in developing advanced materials with tailored electromagnetic properties, such as negative permittivity and permeability, essential for creating novel devices with unique functionalities [25], [28]. Integrating EBG structures in communication technologies, particularly for MMW and submillimeter waves, further underscores their importance in modern engineering applications [29].

Mushroom-Type EBG: These structures are high-impedance surfaces effective at low-frequency bands but suffer from narrow bandwidths. Glide symmetry can be applied to increase their bandwidth significantly without additional manufacturing costs [30].

Corrugated and Strip-Type Soft Surfaces: By optimizing the placement of vias, these surfaces can have bandgaps at lower frequencies compared to mushroom-type EBGs [31]. They offer better miniaturization properties and improved decoupling performance in dense arrays [32].

Groove Gap Waveguide (GGW) EBG: This structure combines soft and hard surfaces with perpendicular ridges. It offers increased structural strength and tunable stopbands, making it suitable for high-frequency applications [17].

In summary, artificially soft and hard surfaces and various EBG structures offer significant advantages in controlling electromagnetic wave propagation and enhancing antenna performance. However, they also present challenges regarding manufacturing complexity and bandwidth limitations, which can be addressed through innovative design approaches.

Brillouin Zone and Its Role in Dispersion Analysis of EBG Structures

The Brillouin Zone (BZ) is a fundamental concept in the study of wave propagation in periodic structures, such as Electromagnetic Bandgap (EBG) structures. It is crucial for understanding the dispersion characteristics, which describe how wave frequencies vary with wave vectors within these structures. The irreducible Brillouin zone, a reduced portion of the BZ, is often used to simplify calculations and analyses of these dispersion relations [33], [34].

In EBG structures, the dispersion diagram is a key tool for visualizing and optimizing the bandgap properties, which are essential for applications like antenna efficiency improvement. The dispersion characteristics within the irreducible Brillouin zone help control the surface wave band gap, which is critical for suppressing unwanted surface waves in microstrip antennas [33]. The methodology for unwrapping dispersion curves using spatial Fourier transforms further enhances the understanding of wave behavior in periodic media, providing insights into the physical meaning and amplitudes of aliased wave components [35].

Moreover, the edges of the Brillouin zone are significant in determining the fundamental features of wave propagation through periodic lattice structures. However, caution is advised when plotting dispersion relations around these edges, as important modes can be missed if not handled carefully [34]. The concept of high-frequency homogenization also plays a role in analyzing the dispersion properties at the edges of the Brillouin zone, particularly in the presence of Dirac points where two branches of the dispersion diagram intersect [36].

For a rectangular or hexagonal periodic EBG lattice, the key high-symmetry points (e.g., Γ , X, M for a square lattice or Γ , K, M for a hexagonal lattice) define the principal paths along which dispersion curves are computed. These curves illustrate the presence of stopbands and passbands,

which directly influence the EBG and gap waveguide performance by determining whether unwanted modes are effectively suppressed.

By tailoring the periodicity and unit cell geometry of the EBG structure, the Brillouin Zone-based dispersion analysis enables the optimization of the transition's performance, ensuring minimal reflection, wideband operation, and efficient mode conversion. This understanding is crucial for designing next-generation low-loss, high-frequency waveguides in the MMW and sub-terahertz regimes.

In summary, the Brillouin Zone is integral to analyzing and optimizing EBG structures, providing a framework for understanding and controlling wave propagation characteristics. This understanding is crucial for designing and applying these structures in various technological fields.

Quasi-TE Modes of GGW

The quasi-TE mode in GGW arises due to the stopband properties of the EBG units, which prevent EM wave leakage outside the groove at frequencies within the stopband (e.g., 61.3 to 95.5 GHz, as observed in [16]). This confinement ensures that the wave propagates efficiently along the groove channel, mimicking the behavior of a conventional waveguide while benefiting from the air-filled, all-metal structure that eliminates dielectric losses. At lower frequencies, where the EBG units are in their passband (e.g., 0 to 61.3 GHz), the structure transitions to support a TE_{10} -like mode across the entire rectangular waveguide region, highlighting the dual-band capability of the extended Band Gap Waveguide (BGW) concept, which integrates GGW within a broader framework.

The quasi-TE mode's geometric parameters of the GGW, such as the pin height, periodicity, air gap, and groove width, influence the quasi-TE mode's characteristics. Dispersion diagrams, simulated using tools like CST and HFSS, reveal that the phase constant (β) of the quasi- TE_{10} mode increases with frequency, aligning closely with the TE mode of a rectangular waveguide at higher frequencies (e.g., above 70 GHz). This behaviour is further validated through electric field distributions, which demonstrate a concentrated transverse field near the EBG structure, ensuring single-mode operation with minimal distortion.

The significance of quasi-TE modes in GGW extends to their application in dual-band systems, enabling seamless transitions between microwave and MMW bands with large frequency ratios

(e.g., 6.8-8.05 GHz and 71-86 GHz in the prototype). This is particularly relevant for the thesis, which focuses on enhancing a sub-6 GHz slotted antenna using GGW feeding. The quasi-TE mode's ability to support wide bandwidths and low insertion losses (e.g., 0.55 ± 0.25 dB at high frequencies and 0.67 dB at low frequencies) provides a foundation for improving antenna performance metrics, such as bandwidth and gain. Moreover, the fully aperture-reused design of BGW, where the high-frequency GGW is embedded within the low-frequency structure, offers a novel approach to antenna feeding that can be adapted to incorporate corrugations and steps, as explored in this work.

In this thesis, the quasi-TE modes of GGW serve as a critical enabler for the proposed antenna enhancements. By leveraging the mode's confinement properties and tunable dispersion characteristics, integrating GGW with a slotted antenna and corrugations aims to optimize radiation patterns, increase bandwidth, and improve gain. The analytical and experimental insights from the work of [16] provide a robust theoretical backdrop, guiding the design and validation of your antenna system within the sub-6 GHz spectrum.

Comparison of Gap Waveguide and Rectangular Waveguide

Gap waveguides, such as the groove gap waveguide (GGW) and ridge gap waveguide, are designed to operate without the need for electrical contact between their components, which is a significant advantage over traditional rectangular waveguides (RWG) [37], [38], [39]. This feature simplifies the manufacturing process and reduces the need for precise assembly, which is particularly beneficial at high frequencies where ensuring proper metal contact is challenging [39], [40].

Gap waveguides, such as the GGW, have been shown to have different propagation characteristics compared to rectangular waveguides, particularly above the cutoff frequency [41]. This can lead to more efficient transmission and reduced losses in specific frequency bands. Additionally, gap waveguides can be designed to support dual-band applications, providing versatility in their use [16].

2.2. Slotted Antennas

This section explores the fundamental principles that govern the operation of Slotted antennas. It provides a historical overview of their development and explores their diverse applications in

various fields. Furthermore, this section examines the key characteristics of slotted antenna structures, including their radiation patterns, impedance characteristics, and bandwidth limitations. It also discusses the various types of slot geometries and their influence on the overall antenna performance.

Slotted antennas are characterized by slots cut into a conductive surface, which influence their radiation patterns, impedance characteristics, and bandwidth. They have evolved significantly and are used in various applications, including wireless communication and MMW technologies.

Slotted antennas have been developed to enhance bandwidth and radiation patterns for various applications, including wireless communication systems, 5G, and terahertz applications [42], [43], [44]. They are particularly valued for providing stable radiation patterns and high gain across wide frequency ranges [45], [46].

Radiation Patterns: Slotted antennas can achieve stable and omnidirectional radiation patterns, which is crucial for consistent signal coverage [45], [46], [47].

Impedance Characteristics: Optimizing slot shapes and feed methods can significantly enhance the impedance bandwidth of slotted antennas, which is crucial for achieving wideband performance [42], [45], [48].

Bandwidth Limitations: While slotted antennas can achieve wide bandwidths, the design must carefully consider slot geometry and feed mechanisms to optimize performance [42], [45], [49].

Slot Geometries and Their Impact

- Slot Shapes: Different slot shapes, such as E-shaped, cross-slotted, and non-uniform slots, can significantly affect the antenna's radiation characteristics and bandwidth. Proper selection and tuning of these shapes are essential for optimal performance [45], [46], [50].
- Feed Methods: The choice of feed methods, such as microstrip lines or coplanar waveguides, also plays a critical role in determining the antenna's impedance matching and bandwidth [45], [46].

Slot Thickness

This section delves into the fundamental principles governing slot thickness in antenna design. It begins with a brief historical overview and explores the practical implications of varying slot thickness on antenna performance. Furthermore, this section concisely summarizes the key characteristics of thick slots, highlighting their unique advantages and exploring their diverse applications in antenna systems.

The concept of slot thickness in antenna design has evolved significantly over time. Initially, the zero-thickness approximation was commonly used, often leading to inaccuracies in antenna performance predictions. For instance, in the design of radial line slot array antennas, it was found that even a small slot thickness, such as one-thirtieth of the wavelength, could lead to significant deviations from expected performance [51]. This realization prompted further research into the effects of slot thickness and the development of more accurate numerical techniques for antenna design.

Varying the slot thickness in antennas can have profound effects on their performance. For example, in terahertz slot antennas, reducing the thickness below 10 nanometers can enhance light-matter interaction, although it poses fabrication challenges [52]. Similarly, the package thickness significantly influences bandwidth in U-slot patch antennas beyond 5 G applications, with optimal performance achieved at specific thickness ranges [53]. Additionally, in leaky-wave slit antennas, substrate thickness variations can transform the antenna's characteristics, affecting gain and bandwidth [54].

Thick slots in antennas offer unique advantages, such as enhanced bandwidth and improved radiation patterns. For instance, introducing more slots in microstrip antennas can enhance bandwidth and reduce the effective area, making the design more compact and efficient [55]. Increasing substrate thickness can be achieved without compromising performance in tapered-slot antennas, allowing for more robust designs [56]. Furthermore, thick slots can improve the radiation characteristics of antennas, as seen in slotted array substrate integrated waveguide antennas, where non-uniform slot designs maintain gain and radiation patterns while achieving significant bandwidth [50].

Thick slots find diverse applications across various antenna systems. They are particularly beneficial in high-frequency applications, such as MMW and terahertz frequencies, where precise control over electromagnetic wave manipulation is crucial [57]. In phased array applications beyond 5 G and 6G technologies, thick slots contribute to achieving the desired bandwidth and performance [53]. Additionally, they are used in compact designs for 5G applications, where space and efficiency are critical [55].

In summary, the evolution of slot thickness in antenna design has led to significant advancements in performance and application diversity. By understanding and optimizing slot thickness, designers can enhance antenna capabilities, making them suitable for various modern communication technologies.

2.3. Corrugations

This section investigates the fundamental principles governing the use of corrugations in antenna design. It traces the historical development of this technique and explores its diverse applications in modern antenna systems. Furthermore, it provides a concise overview of the key properties of corrugated surfaces and discusses their significant advantages and practical applications.

The use of corrugations in antenna design is a well-established technique that has evolved significantly over time. Initially, corrugations were introduced to improve the performance of horn antennas by reducing cross-polarization and enhancing bandwidth. This technique has since been adapted and optimized for various modern applications, including satellite communications and MMW technologies.

Corrugated antennas have been developed to address specific challenges in antenna design, such as impedance matching and radiation pattern control. For instance, the integration of corrugations in horn antennas has been shown to reduce cross-polarization and improve bandwidth, making them suitable for satellite applications [58]. Similarly, using corrugations in Vivaldi antennas has enhanced their gain and bandwidth, making them practical for microwave imaging and 5G MMW applications [59], [60].

Corrugated surfaces are characterized by their ability to manipulate electromagnetic waves, resulting in improved antenna performance. The design of corrugated antennas often involves optimizing the dimensions and arrangement of the corrugations to achieve desired properties such

as gain, bandwidth, and directivity. For example, using elliptical slots in Vivaldi antennas has significantly increased gain without increasing the antenna size [61]. Additionally, incorporating Meta surface corrugations can reduce mutual coupling in MIMO systems, enhancing isolation and efficiency [62].

There are numerous advantages to using corrugated surfaces in antenna design. They include improved gain, reduced back radiation, and enhanced bandwidth. These benefits make corrugated antennas suitable for various applications, from radar systems to satellite communications. For instance, using corrugations in substrate-integrated waveguide antennas has led to compact designs with excellent isolation and gain characteristics, suitable for radar applications [63]. Moreover, groove gap waveguide technology has demonstrated the ability to suppress grating lobes and enhance radiation efficiency [8].

In summary, integrating corrugations in antenna design offers significant advantages in terms of performance enhancement and application versatility. This technique continues to be a critical area of research and development in modern antenna systems.

2.4. Coaxial to GGW Transition

This section focuses on the fundamental principles governing the transition from coaxial to groove gap waveguides. It provides a historical context, explores its practical applications, and summarizes this transition's key characteristics and advantages.

The transition from coaxial to groove gap waveguides represents a significant advancement in high-frequency waveguide technology. Coaxial lines were widely used due to their simplicity and effectiveness in various applications. However, as the demand for higher-frequency applications increased, the limitations of coaxial lines, particularly in bandwidth and loss, became apparent. The development of groove gap waveguides (GGWs) emerged as a solution to these challenges, offering improved performance in terms of bandwidth and reduced losses [64], [65], [66].

Groove gap waveguides have found numerous applications in modern high-frequency systems. They are particularly useful in environments where space is constrained, as they can be designed in compact configurations without the need for dielectric materials, which simplifies the design and reduces losses [65]. GGWs are also employed in rotary joints, crucial in systems requiring rotational movement without signal degradation, such as radar and satellite communications [66].

Additionally, GGWs are used in high-gain antenna arrays, where their ability to maintain low insertion loss and high efficiency is critical [67].

Several key advantages characterize the transition from coaxial to groove gap waveguides. GGWs can achieve wide bandwidths, which is essential for modern communication systems. For instance, some designs achieve bandwidths covering significant portions of the frequency spectrum, such as 55% bandwidth from 11 to 19.5 GHz [66]. Also, GGWs exhibit low insertion loss, crucial for maintaining signal integrity over long distances. For example, some transitions maintain insertion losses better than 0.05 dB [65]. The design of GGWs often eliminates the need for complex electrical connections, reducing mechanical complexity and fabrication costs [67]. Moreover, Many GGW designs achieve high return loss, indicating excellent impedance matching and minimal signal reflection. Some configurations achieve return losses better than 20 dB over their operational bandwidths [68], [69].

Summary

The transition from coaxial to groove gap waveguides marks a pivotal development in high-frequency waveguide technology. They offer significant improvements in bandwidth, loss, and mechanical simplicity. These advancements have enabled many practical applications, from compact antenna arrays to rotary joints, making GGWs a versatile and efficient choice for modern communication systems.

Chapter III:

Design and Simulation of GGW using EBG

3.1. Introduction

Groove Gap Waveguides (GGWs), as shown in Figure 3.1, have emerged as promising transmission lines for high-power microwave applications due to their unique characteristics, including high power handling capacity, low dispersion, and low loss. However, challenges such as surface wave propagation and mode degeneration can limit their performance. Electromagnetic Bandgap (EBG) structures, artificially engineered materials with periodic structures, offer a promising solution to mitigate these limitations.

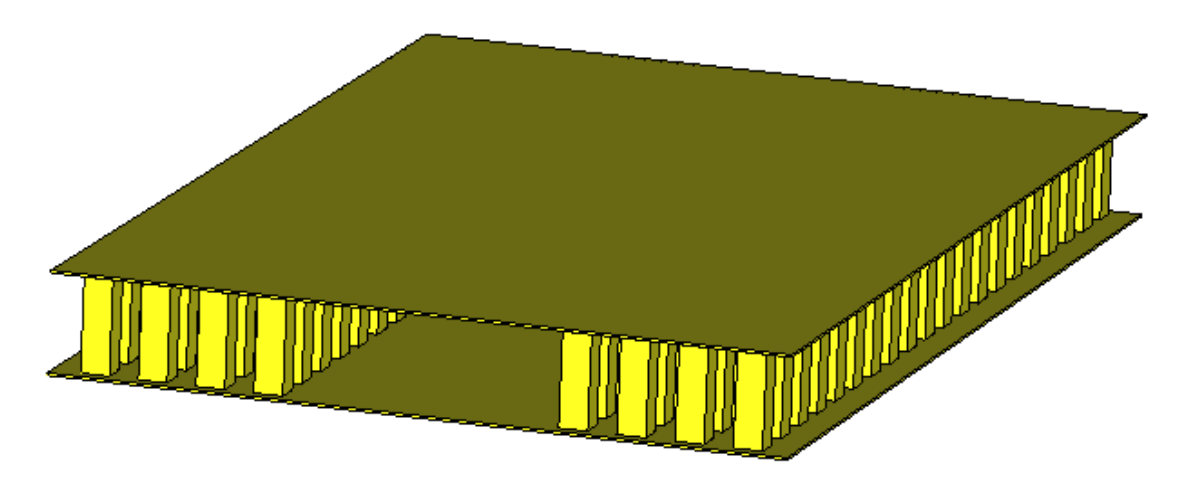


Figure 3.1. Groove gap waveguide using metal pins EBG

This chapter explores the integration of EBG structures within GGWS to enhance their performance. We begin by reviewing the fundamental principles of EBG structures, including their types, design considerations, and applications. Subsequently, we explore the challenges and opportunities of incorporating EBG structures into GGWS. This includes discussing the potential benefits of EBG integration, such as suppressing surface waves, improving mode purity, and

enhancing bandwidth. Finally, we explore various implementation techniques for integrating EBG structures into GGWs, such as embedding EBG structures within the walls of the GGW. This chapter aims to provide a comprehensive overview of integrating EBG structures into GGWs, emphasizing their potential to significantly enhance the performance of these vital transmission lines for high-power applications.

3.2. Unit Cell EBG

Figure 3.2 illustrates the individual unit cells of the pin structure, which are then periodically arranged to form the complete EBG structure. To determine the frequency range where wave propagation is prohibited (the stopband), we analyzed the dispersion characteristics of the unit cells using the eigenmode solver within CST Studio Suite. The initial dimensions of the unit cell were chosen based on established design guidelines [70], [71]. Specifically, the pin height (d) and period (p) were set to 14.7 mm (equivalent to 0.25λ at 5.1 GHz), and the pin width (a) was set to 0.1λ at 5.1 GHz. The air gap height (ag) was minimized to 0.588 mm to ensure a wide stopband.

CST's Eigenmode Solver analyzes the EBG structure by solving Maxwell's equations as an eigenvalue problem using FEM, applying periodic boundary conditions and phase sweeps across the Brillouin Zone. It computes the eigenfrequencies and field distributions of the modes, generating a dispersion diagram to identify the stopband.

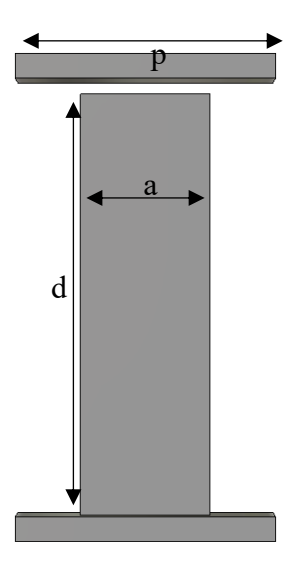


Figure 3.2. Metal Pin EBG Structure

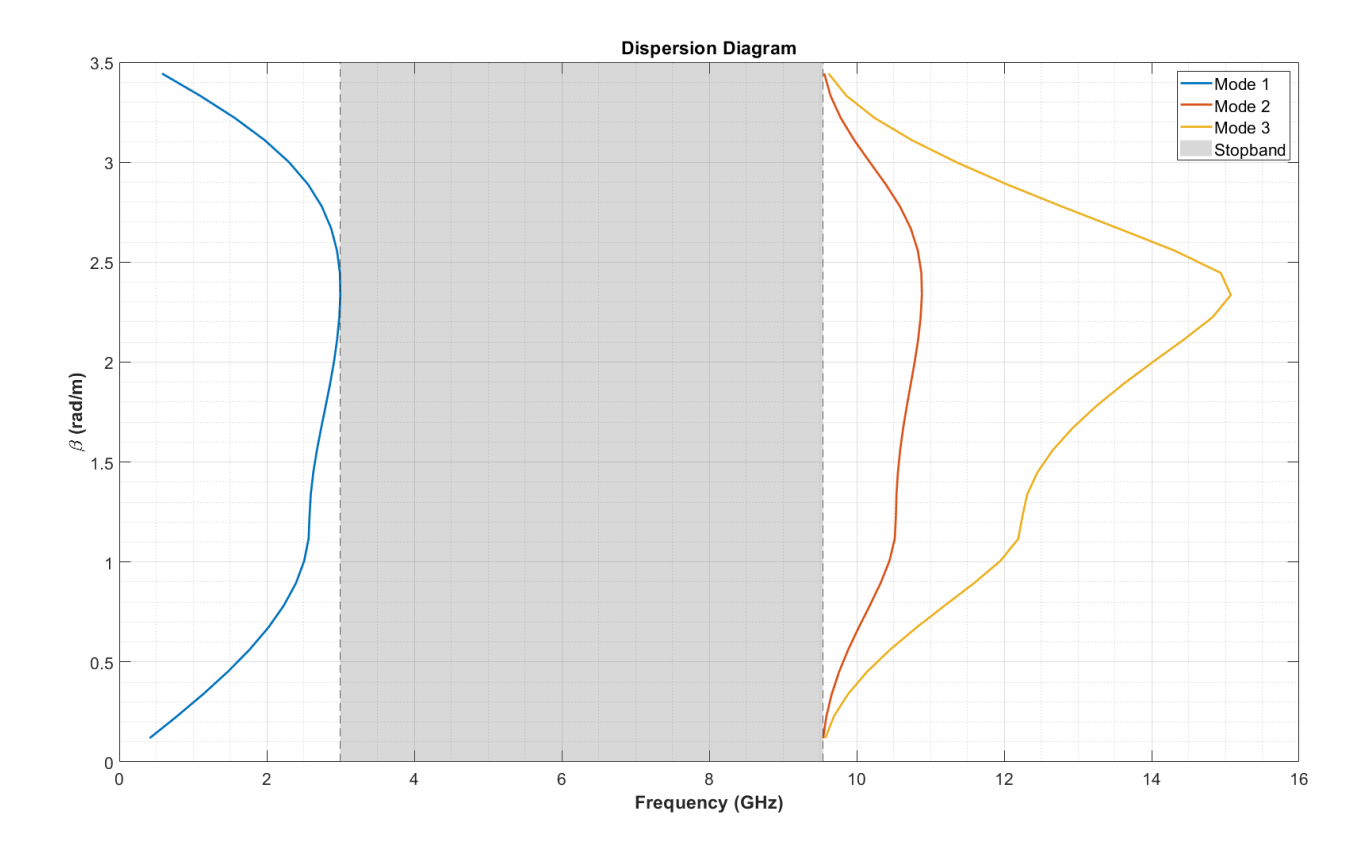


Figure 3.3. EBG Dispersion Diagram

Figure 3.3 depicts the dispersion diagram, illustrating the variation of the propagation constant with frequency. This diagram reveals a bandgap between 2.99 and 9.57 GHz where no modes can propagate.

The air gap in EBG structures, such as those used in GGW designs, plays a critical role in determining the electromagnetic behaviour, particularly the stopband characteristics, wave confinement, and overall performance of the structure.

Figure 3.4 presents the dispersion diagrams for the first three modes of the EBG structure. The effect of varying the air gap size (ag) on the bandgap characteristics and modal behaviour is examined. Each subplot represents the dispersion curves for different values of "ag", where the stopband (bandgap region) is highlighted in gray. The normalized phase constant (β/m) is plotted against frequency.

The investigation into the air gap "ag" reveals significant effects on the EBG structure's performance. As "ag" increases, the stopband widens, which proves beneficial for GGW

applications by enhancing mode suppression—a critical requirement for effective wave confinement. While the lower cut-off frequency of the bandgap remains relatively stable, the upper limit extends with larger "ag" values, broadening the operational range. Regarding mode evolution, the fundamental mode remains largely unchanged across all cases, ensuring consistent performance. However, higher-order modes become more pronounced as "ag" increases, indicating a shift in the structure's modal behaviour that must be carefully managed to maintain desired antenna characteristics.

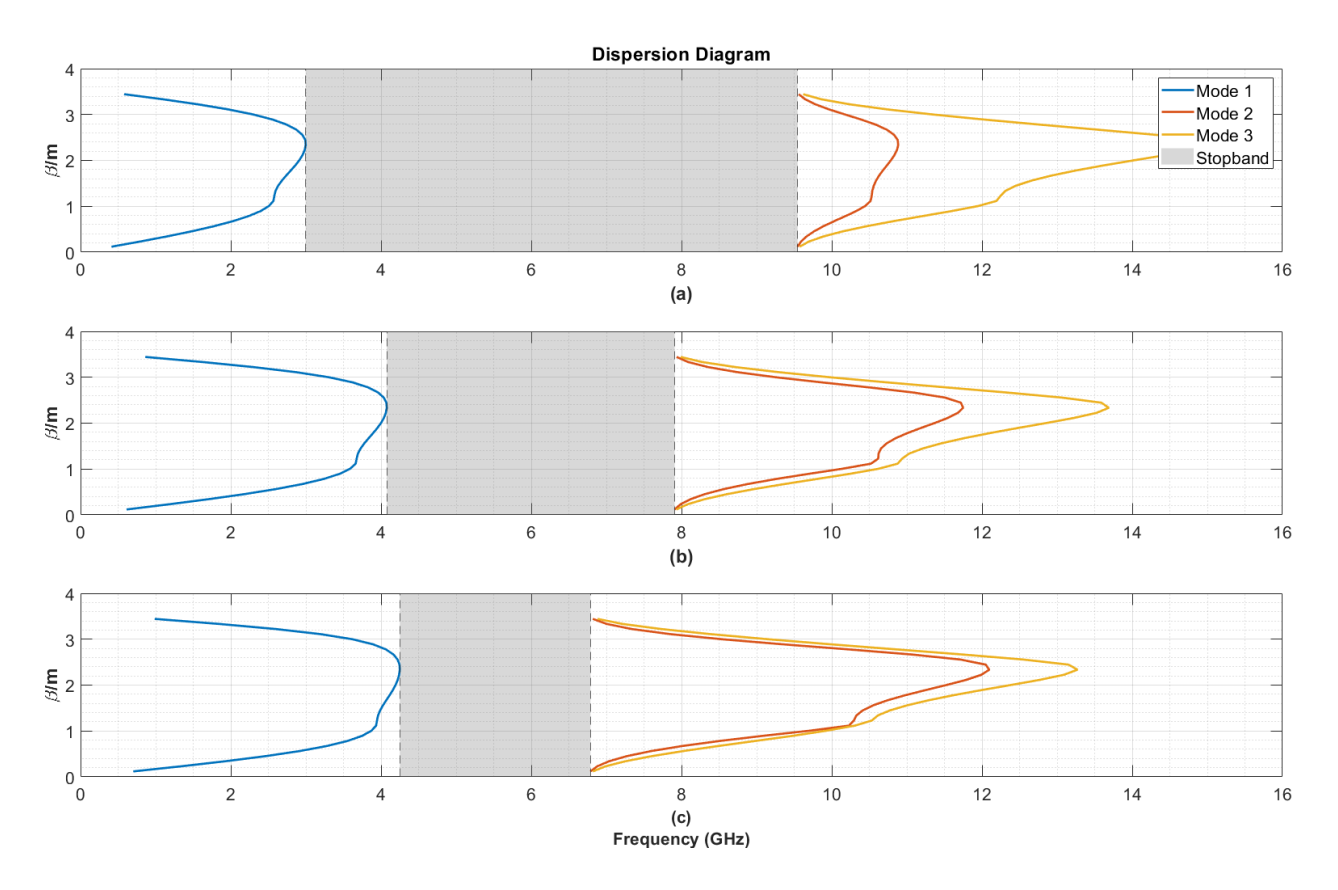


Figure 3.4. Dispersion Diagram, Effect of Air Gap size reduction a) ag=0.588 mm, b) ag=3 mm, and c) ag=5.88 mm

The cell size in an Electromagnetic Bandgap (EBG) structure, typically defined by the periodicity of the unit cell (e.g., the spacing between metallic pins), significantly influences the electromagnetic properties, including the stopband, dispersion characteristics, and wave confinement.

Based on the results presented in Figure 3.4, an air gap size of 0.588 mm was selected for further investigation as it exhibited the highest bandgap among the tested configurations. Subsequently,

Figure 3.5 illustrates the effect of reducing the unit cell size on the band gap. The results demonstrate that a decrease in cell size also leads to a reduction in the bandgap.

The results indicate that optimizing for a higher bandgap requires a combination of design choices. This suggests that carefully balancing these two parameters is crucial for achieving the desired bandgap characteristics.

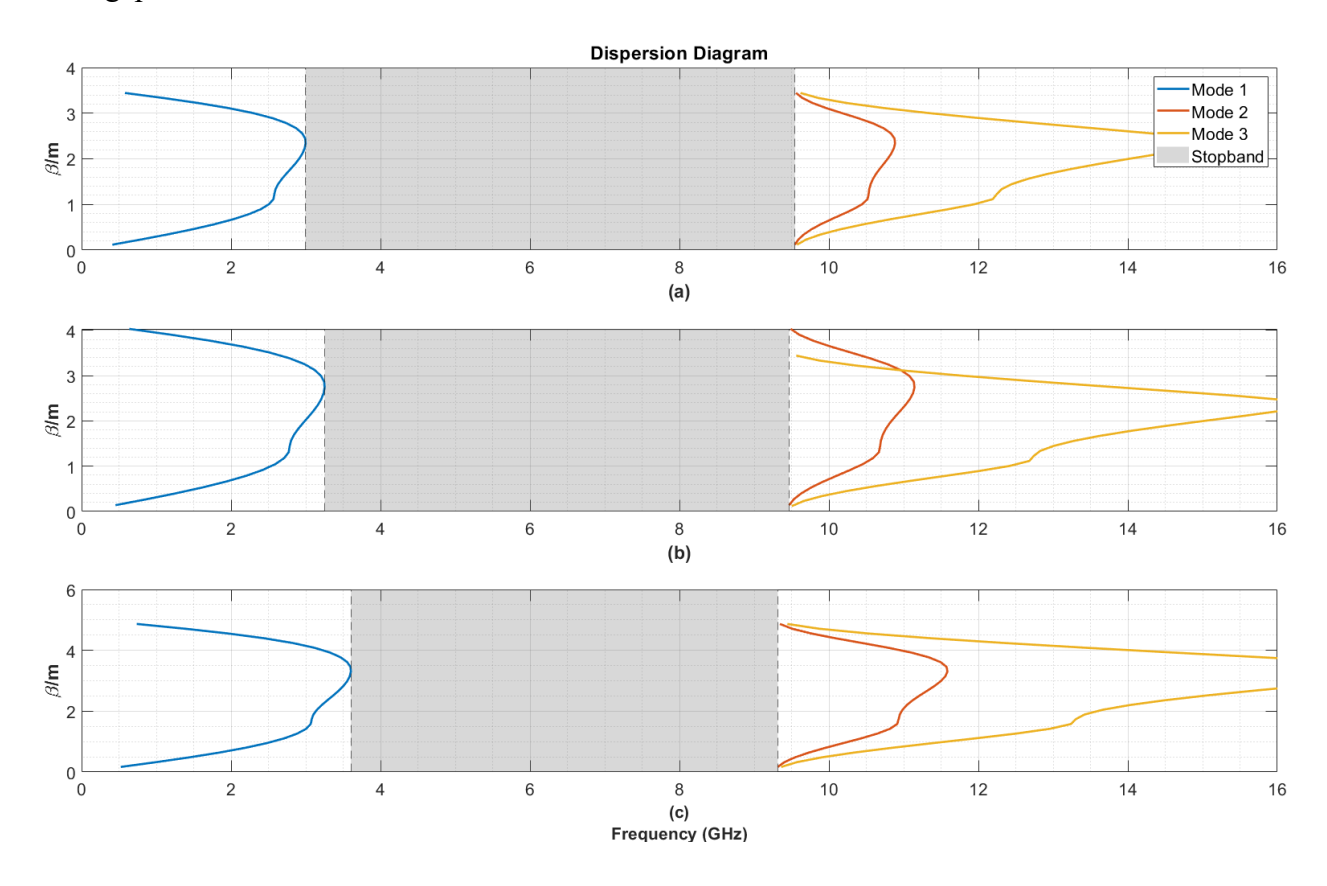


Figure 3.5. Dispersion Diagram, Effect of Cell Size reduction a) p=14.7 mm, b) p=12.25 mm, and c) p=10.4 mm

Figure 3.6 presents the dispersion diagrams for an EBG structure with different pin sizes (a). The first three modes are analyzed.

The analysis of varying pin sizes in the EBG structure reveals that the overall dispersion characteristics remain largely unchanged, indicating a limited impact on the structure's behaviour across different configurations. Specifically, Modes 2 and 3 exhibit minimal variation, suggesting that pin size has a negligible effect on the bandgap frequency and width, thereby maintaining consistency in the stopband region. This stability implies that while adjustments to pin size may offer minor refinements, other parameters—such as the air gap or periodicity—are likely more

critical for tuning the EBG performance to meet the specific requirements of the GGW application in this antenna design.

Since the pin size does not significantly affect the bandgap, alternative design parameters should be explored to further optimize EBG structures.

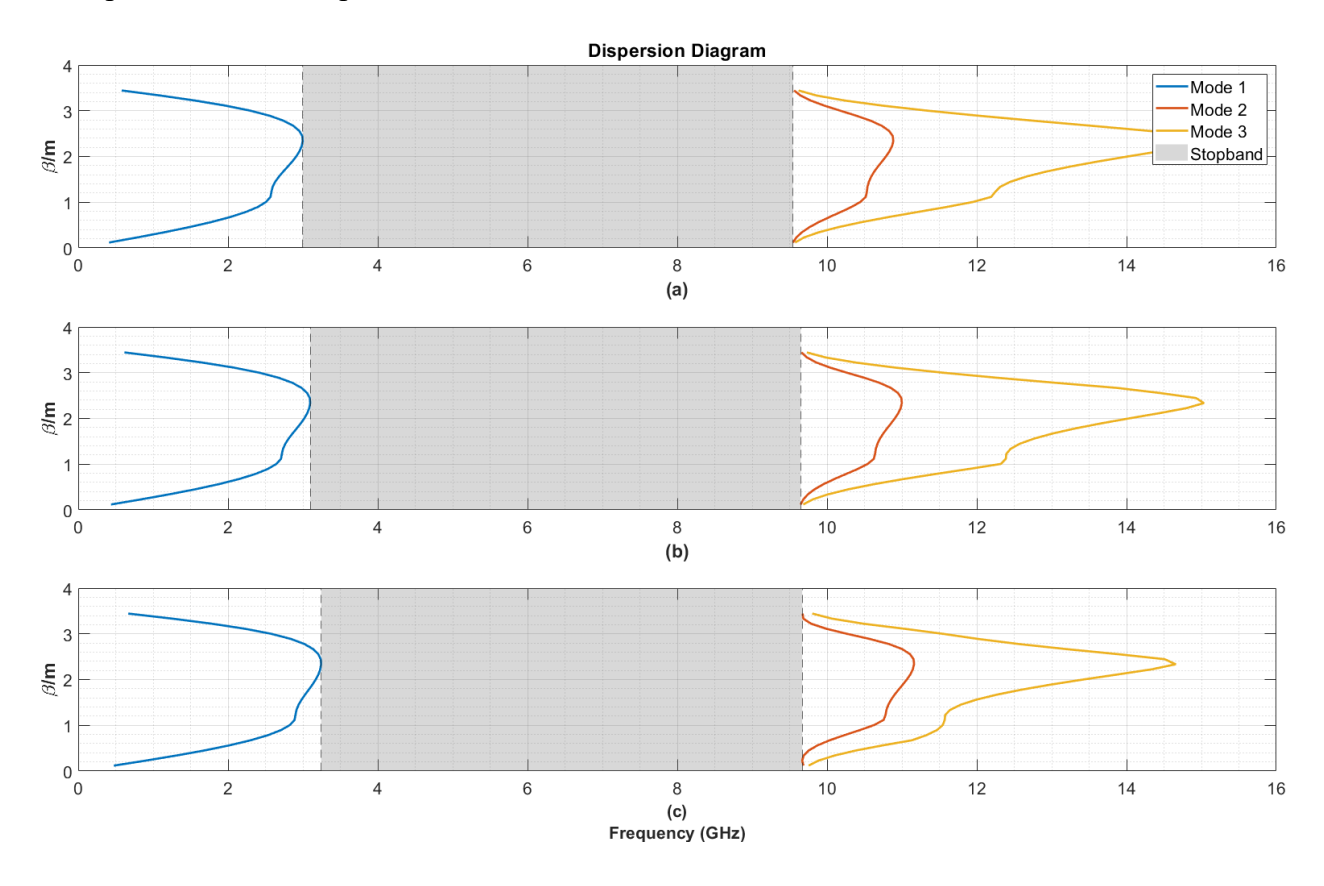


Figure 3.6. Dispersion Diagram, Effect of Pin Size reduction a) a=5.8 mm, b) a=4.8 mm, and c) a=3.8 mm

These dispersion diagrams illustrate the effect of varying the pin height (d) on the EBG structure's first three modes. The three subfigures correspond to:

- (a) d=14.7d=14.7d=14.7 mm
- (b) d=15.8d=15.8d=15.8 mm
- (c) d=16.9d=16.9d=16.9 mm

Analyzing pin height variations in the EBG structure reveals distinct effects on its modal behaviour and stopband characteristics. The fundamental mode (Mode 1, blue line) remains unchanged mainly across different pin heights, exhibiting a low-frequency band that indicates minimal impact from these variations. For the higher-order modes (Modes 2 and 3, red and yellow lines), the

stopband (shaded region) shows stability, with only minor shifts in its upper and lower bounds; increasing the pin height (d) slightly adjusts the cut-off frequency of these modes but does not significantly alter their overall behaviour. The stopband, defined by the gap between the first and second modes, experiences no dramatic shifts with changes in "d", suggesting that other parameters, such as pin width or spacing, may substantially influence the EBG effect in this GGW design.

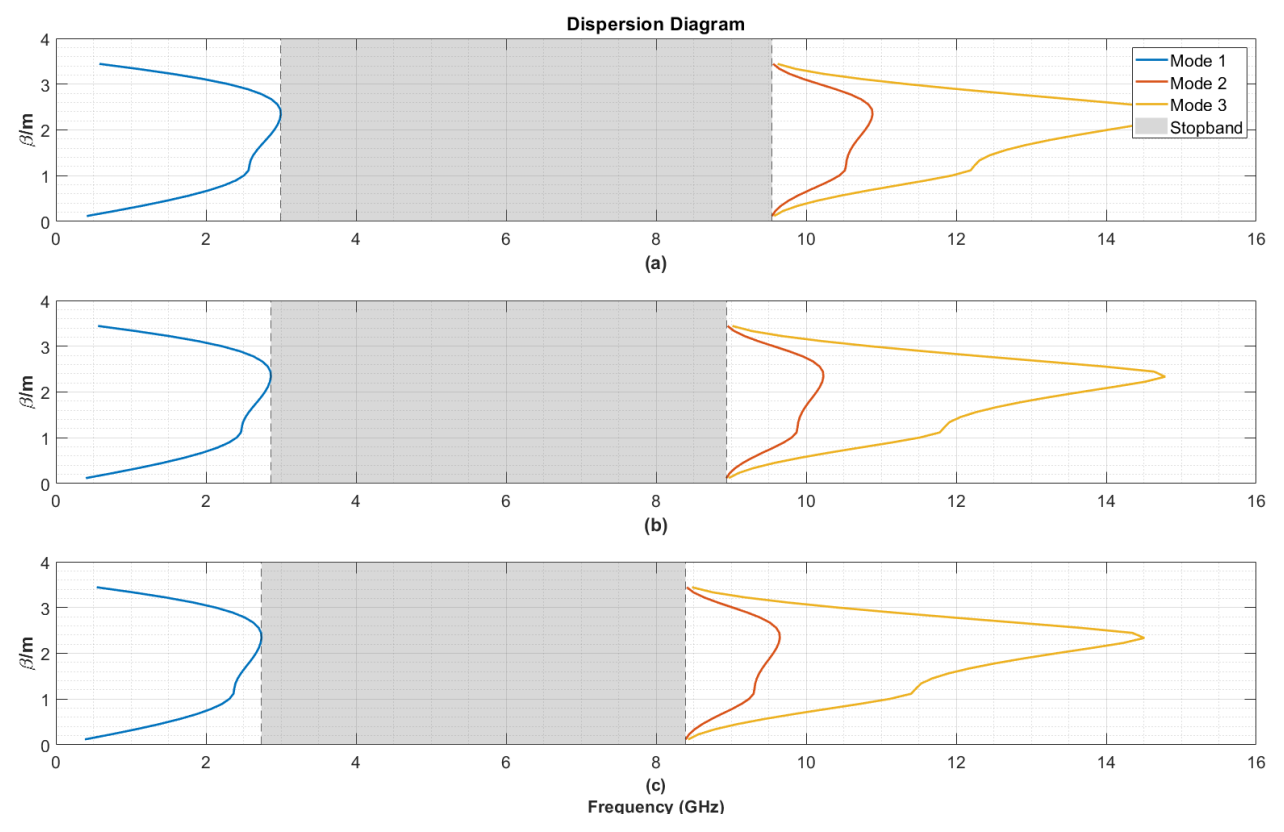


Figure 3.7. Dispersion Diagram, Effect of Pin Height Reduction: a) d=14.7 mm, b) d=15.8 mm, and c) d=16.9 mm

The results indicate that pin height variations have a minor effect on the overall dispersion characteristics, particularly for the fundamental mode. However, adjusting "d" alongside other parameters may be necessary for precise tuning of the stopband.

Figure 3.8 illustrates three pin shapes – square, octagonal, and cylindrical – which will be investigated through simulations to determine their influence on the bandgap.

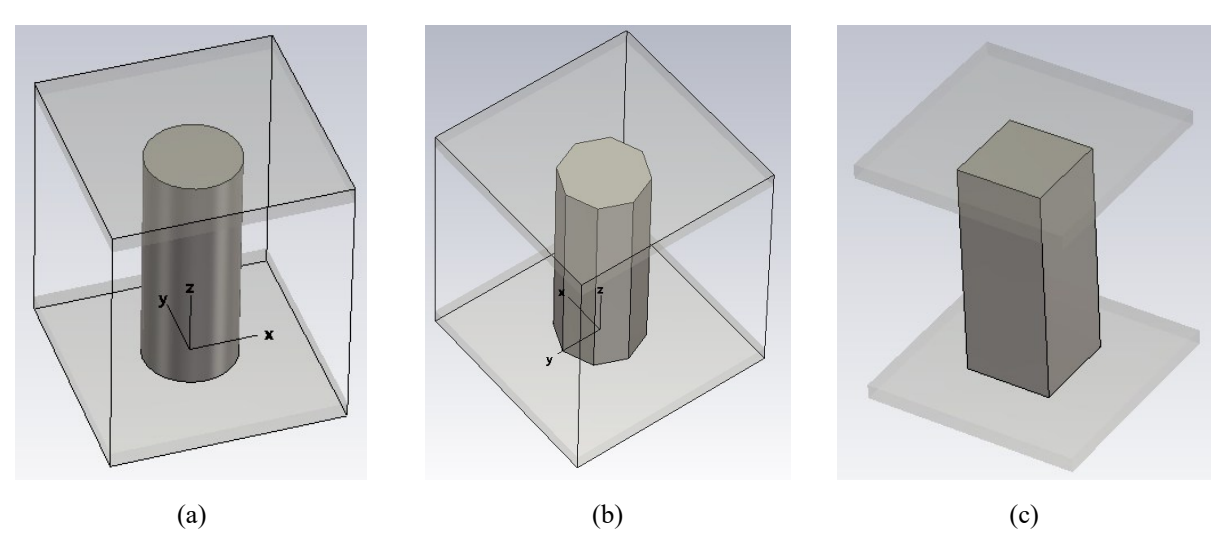


Figure 3.8. Various shapes of Nails: a) Cylindrical, b) Octagonal, and c) Square

CST simulations reveal that the bandgap characteristics exhibit no significant variation across the three pin shapes: square, octagonal, and cylindrical, as depicted in Figure 3.9.

Based on the results, square pins were selected for subsequent simulations to simplify the manufacturing process.

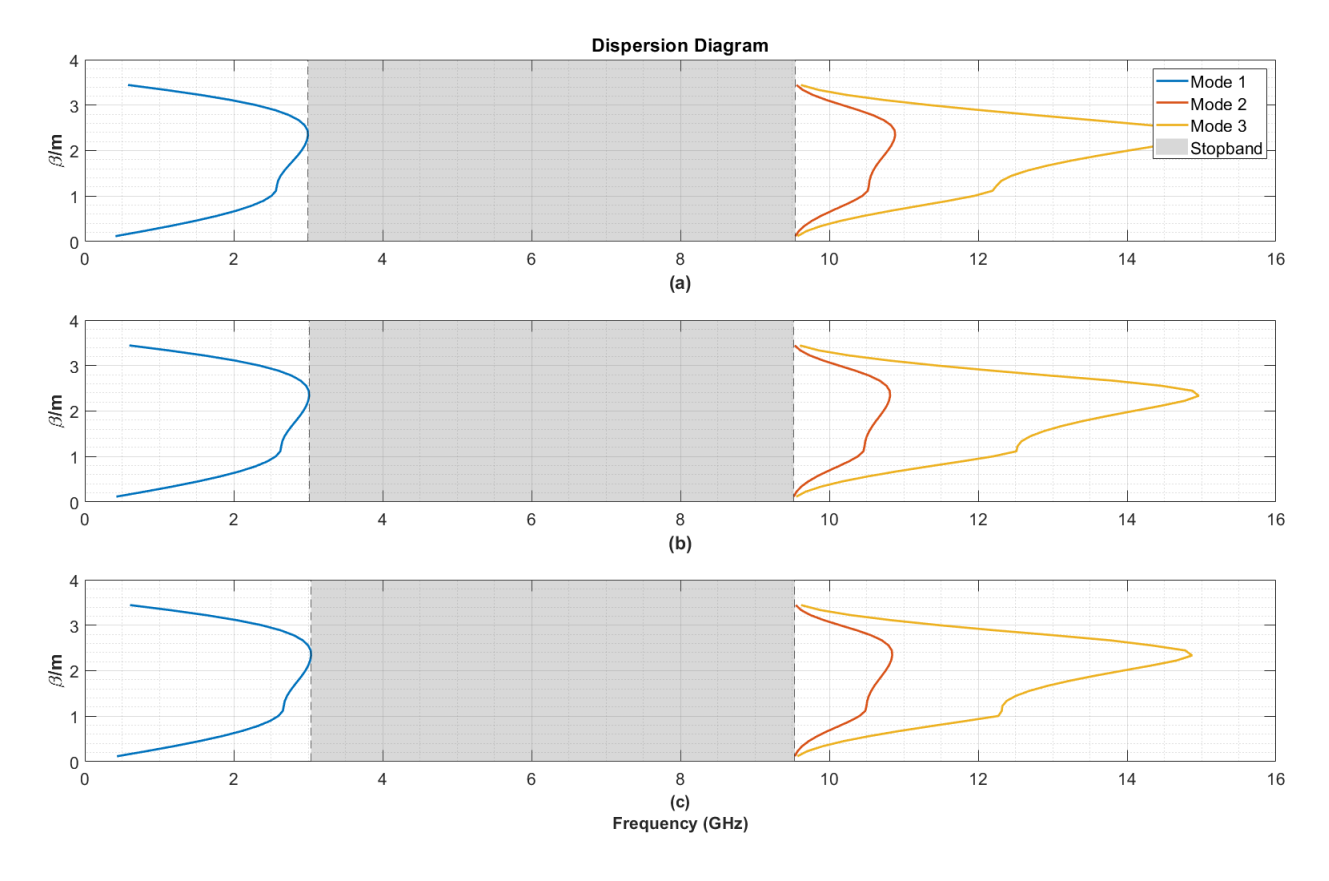


Figure 3.9. Dispersion Diagram, Different Shapes: a) Square, b) Cylindrical, and c) Octagonal

3.3. GGW Design

Figure 3.10 illustrates the geometry of a GGW. A key characteristic of the GGW is the elimination of direct electrical contact between the upper and lower metal plates. Instead, a periodic array of metal pins is introduced on the lower plate, creating a soft surface that effectively functions as an artificial magnetic conductor (AMC). This AMC suppresses wave propagation in lateral directions within a specific frequency range, known as the stopband [67].

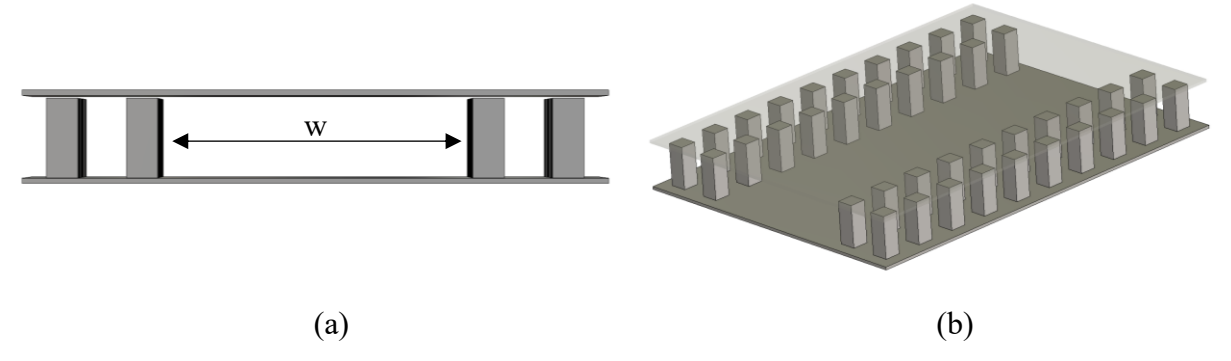


Figure 3.10. Groove Gap Waveguide: a) Front View, b) Perspective View

The GGW, analogous to a rectangular waveguide, facilitates the propagation of TE and TM modes. The waveguide's cross-sectional dimensions determine the specific modes that it supports. However, the TE_{10} mode is generally favoured in most practical applications [72].

The starting point for designing a GGW involves understanding its resemblance to conventional waveguides and defining key parameters such as effective width and propagation constants.

The design process often begins by defining an adequate width for the groove gap waveguide, which can be directly correlated to a rectangular waveguide. This allows conventional equations to be used for designing components, ensuring good impedance matching and desired performance characteristics [73].

The geometry of conventional hollow ridge or rectangular waveguides can serve as a good starting point for designing groove gap waveguide components by comparing the dispersion characteristics and field distributions of groove gap waveguides with traditional waveguides using numerical analysis. This is due to the similarity in dispersion diagrams and characteristic impedances within the stopband of parallel-plate modes [74].

Once the effective width and propagation constants are established, design equations can be applied to optimize the waveguide for specific applications, such as antennas or filters, ensuring efficient performance [73], [75].

The design of a groove gap waveguide starts with defining its effective width and understanding its resemblance to conventional waveguides. This foundational understanding allows for applying traditional design equations and optimization techniques, facilitating the development of efficient and well-matched waveguide components.

For a frequency range starting from 3 GHz, the cut-off frequency should be 25% lower, which means it needs to be set at 2.4 GHz. The TE_{10} mode cut-off frequency of the waveguide can serve as the initial reference. Using this approach, the waveguide width can be determined from:

$$f_c = \frac{c}{2} \sqrt{\left(\frac{m}{a}\right)^2 + \left(\frac{n}{b}\right)^2} \tag{3.1}$$

where a represents the waveguide's width and b its height. For the TE_{10} mode with a cut-off frequency of 2.4 GHz, the calculated waveguide width is 62.5 mm. Therefore, our initial estimate for the GGW width is also 62.5 mm.

To determine the propagating modes, we employ an eigenmode solver to simulate a unit cell of the GGW, guided by Figure 3.11 and the Brillouin Zone geometry.

Figure 3.12 illustrates the propagating modes within the EBG cell's bandgap for three distinct widths: 62 mm, 58 mm, and 52 mm. A notable observation is that as the GGW's width increases, the cut-off frequency experiences a decrease.

The diagrams reveal that the changes between the Γ and X points (x-axis) in the Brillouin Zone do not align with the propagation direction. In contrast, the wave propagation between the X and M points (y-axis) is critical for our analysis. The green line, representing Mode 5, is the first mode to emerge within the gray region, indicating the EBG stopband.

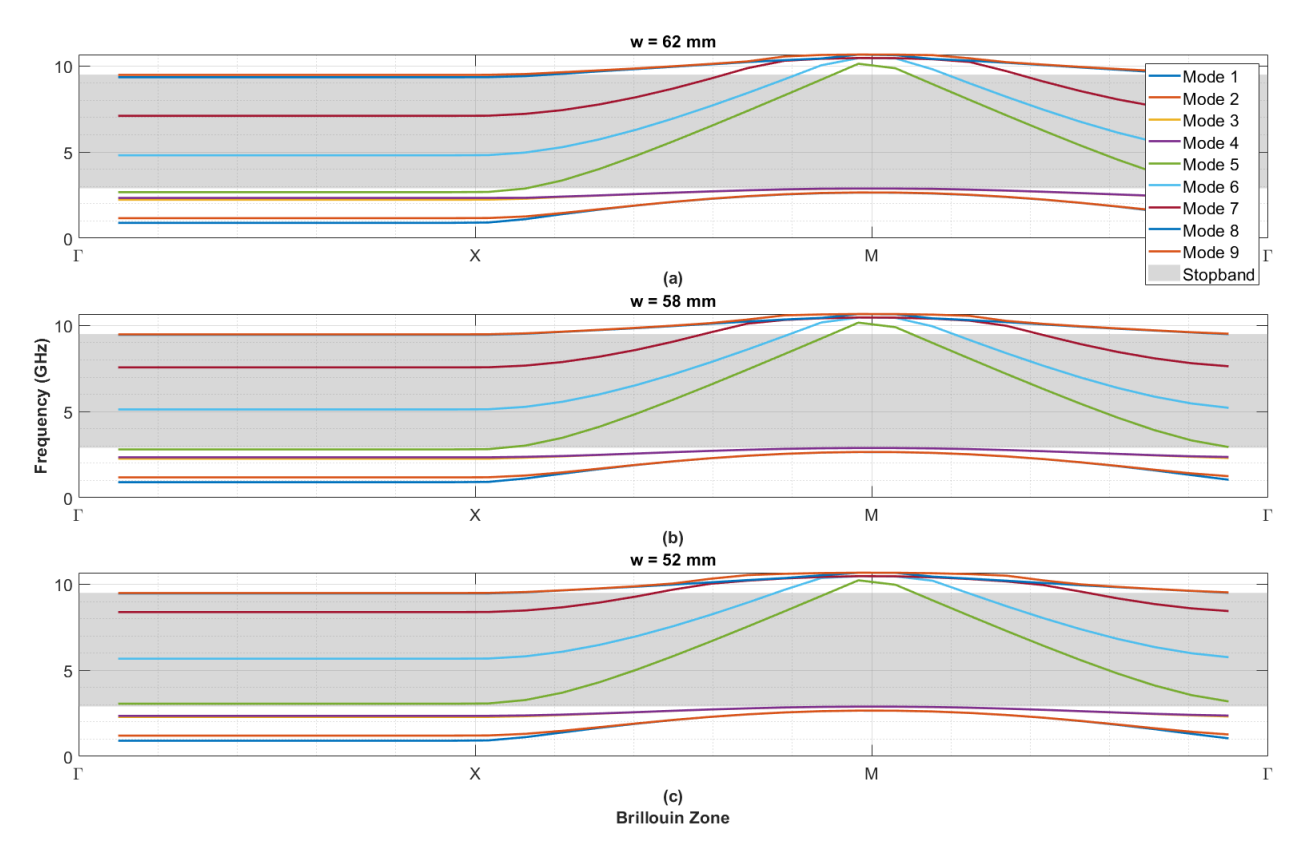


Figure 3.12. Eigenmode Solver Modes and EBG Stopband a) w=62 mm, b) w=58 mm, and c) w=52 mm

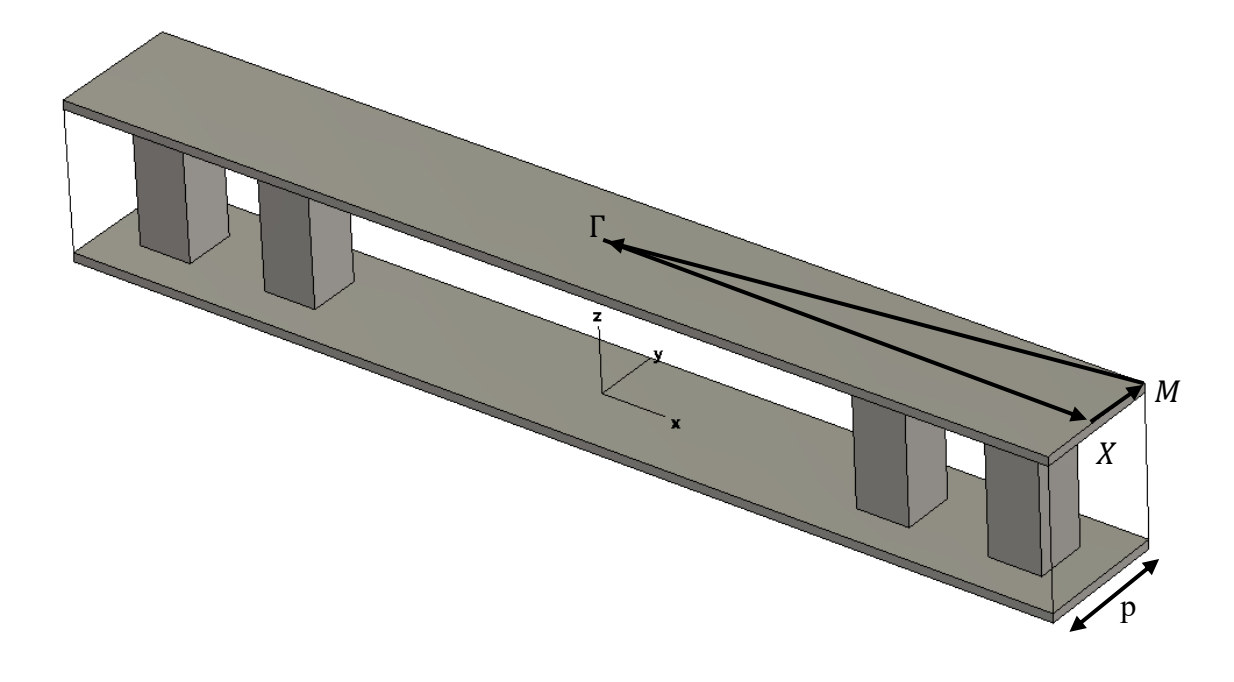


Figure 3.11. GGW Unit Cell

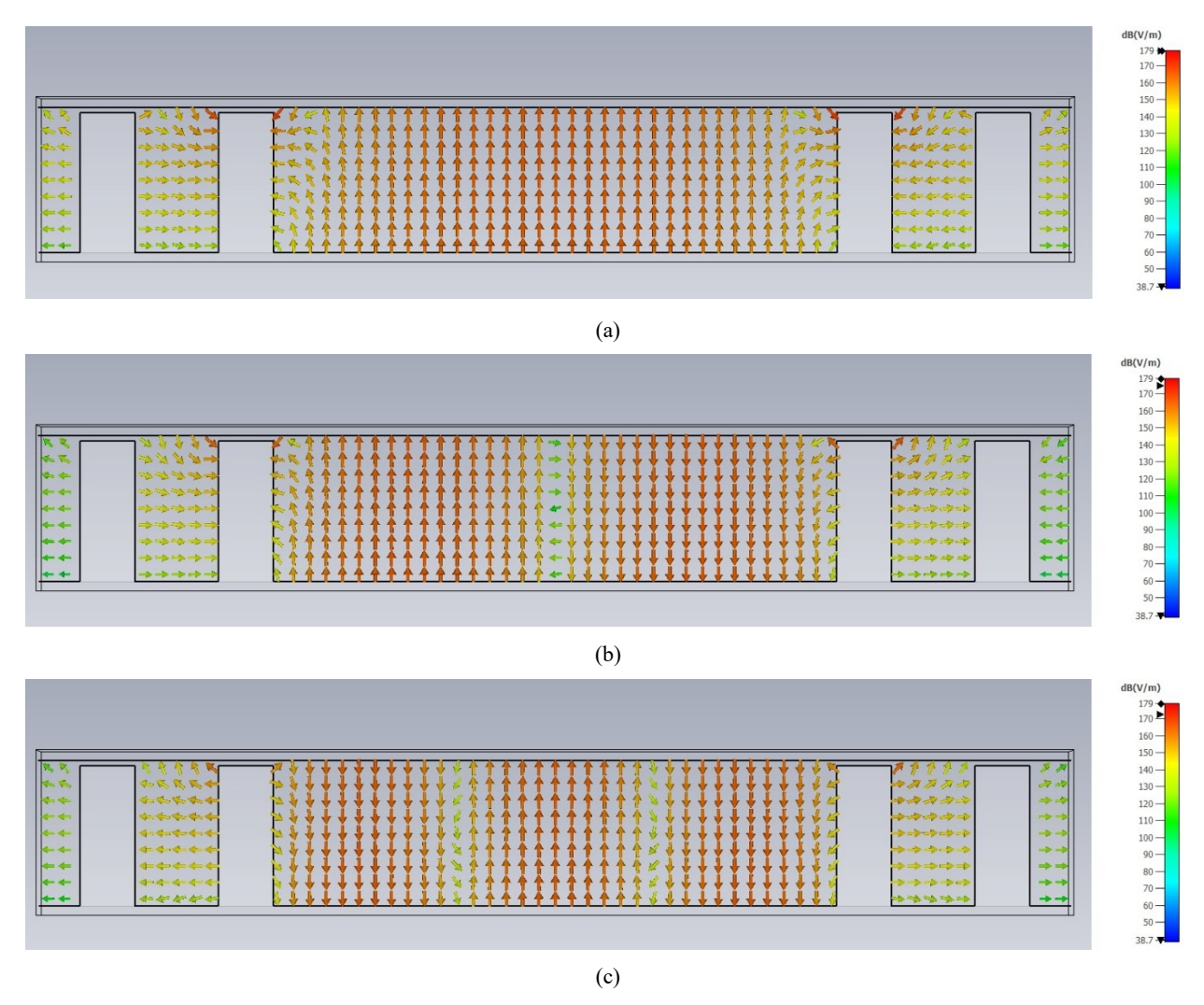


Figure 3.13. Modes of Electric Field Distribution a) Mode 5, b) Mode 6, and c) Mode 7

The GGW exhibits propagation characteristics similar to a conventional rectangular waveguide, supporting similar TE and TM modes. However, the periodic array of pins significantly influences wave propagation. These pins act as an artificial magnetic conductor (AMC), effectively confining the majority of the wave energy within the groove region. This confinement guides the wave along the desired direction.

Figure 3.14 depicts the port mode of the designed GGW. As evident from the figure, the grooves are oriented along the Y-direction, while the top and bottom surfaces of the GGW are perfectly electrically conducting (PEC) planes along the z-axis.

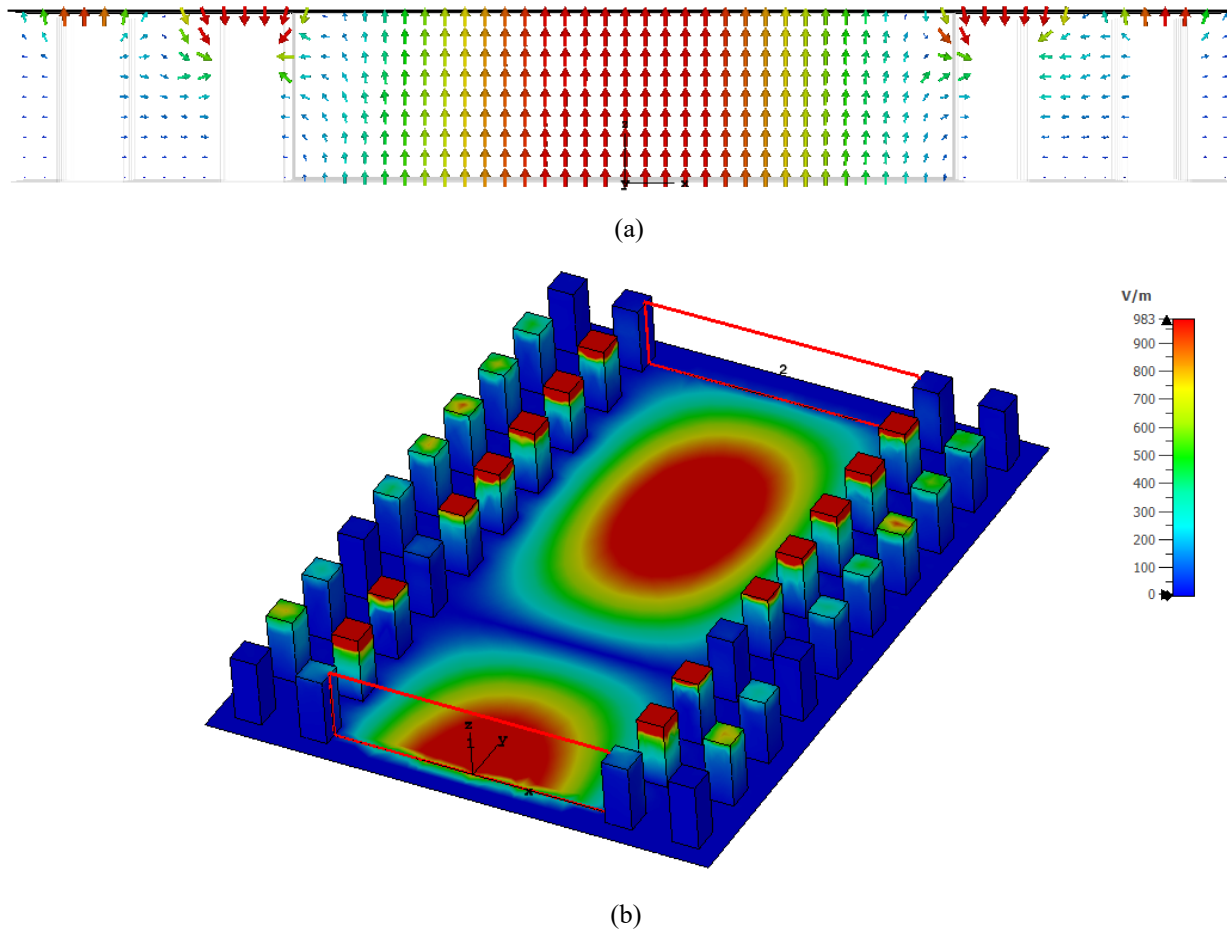
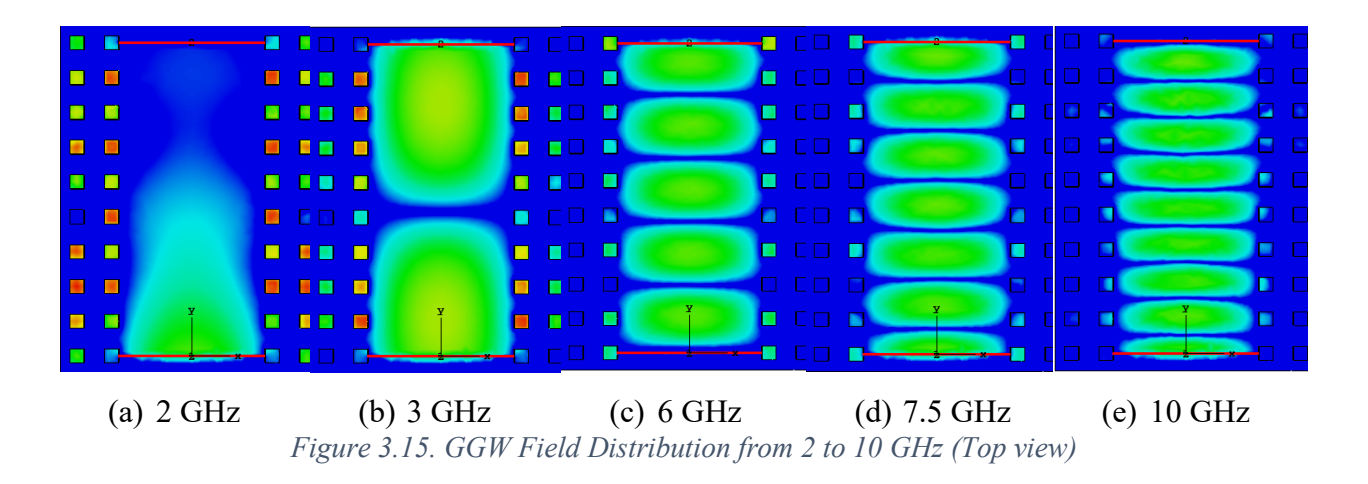


Figure 3.14. Electric Field Distribution a) From the port b) Field Distribution along GGW (Top layer is hidden)

The GGW, with its array of lateral pins, effectively mimics a magnetic conductor, theoretically confining the wave propagation within the groove direction. However, in reality, perfect magnetic surfaces are unattainable. Consequently, some field components will inevitably propagate transversely to the groove direction. Figure 3.15 illustrates the field distribution behavior of the GGW for the first mode across a frequency range of 2 to 10 GHz. The figure clearly demonstrates that the field experiences rapid attenuation beyond the initial row of pins within the EBG stopband, spanning 2.99–9.57 GHz [67].



Several analytical and numerical methods can be employed to obtain the characteristic impedance of a groove gap waveguide. The characteristic impedance is a crucial parameter for understanding waveguide transmission properties.

The characteristic impedance can be derived by solving an eigenvalue problem, which involves analyzing the dispersion characteristics of the waveguide. This approach is used to understand the modes propagating in the waveguide and their associated impedance [76]. The dispersion equation and coupling impedance can also be obtained through approximate field theory, which considers the influence of various circuit dimensions on these parameters [77]. The Characteristic Basis Function Method combined with the parallel-plate dyadic Green's function method can be used to calculate the impedance characteristics of electrically large gap-waveguide structures. This method offers reduced computation times while maintaining accuracy [78]. Numerical solutions to the Wiener–Hopf equation, derived from boundary value problems, can also provide insights into the impedance characteristics. This involves numerically solving an infinite system of linear algebraic equations [79]. Fabrication and measurement of prototypes, such as bandpass filters or other components using groove gap waveguides, can verify the theoretical and numerical predictions of characteristic impedance [80], [81].

The characteristic impedance of a groove gap waveguide can be obtained through a combination of analytical and numerical methods supported by experimental validation. Analytical approaches focus on solving eigenvalue problems and dispersion equations, while numerical methods, such as the Characteristic Basis Function Method, provide efficient computation. These methods

collectively ensure accurate determination of impedance, which is crucial for the design and application of groove gap waveguides in various technologies.

The field distribution similarity between rectangular waveguides (RWG) and GGW is a topic of interest due to the potential advantages of GGW in high-frequency applications. Both waveguide types can support similar modes, but there are distinct differences in their construction and field distribution characteristics. The GGW and RWG can support the TE10 mode, the dominant mode in rectangular waveguides. However, GGW confines the electromagnetic wave within the groove using a stopband created by the bed of nails, which is not present in RWG [16], [82].

The dispersion diagrams of GGW and RWG show similarities within the stopband of the parallel-plate modes, indicating that they can be used interchangeably in specific frequency ranges [74].

GGW offers a unique advantage by not requiring electrical contact between the upper and lower plates, which is beneficial at high frequencies. This design leads to a different field distribution than RWG, which relies on metal contact for field confinement [39], [82].

GGW does not require the precise metal contact needed in RWG, which can lead to differences in field distribution, especially at high frequencies where metal contact is challenging to maintain [37], [39]. The GGW and RWG exhibit different propagation characteristics above the cutoff frequency due to GGW's unique structure, which affects how the fields are distributed and confined [41].

While GGW and RWG can support similar modes and have comparable dispersion characteristics within specific frequency ranges, their field distributions differ due to structural differences and the absence of metal contact in GGW. This makes GGW a suitable alternative for high-frequency applications where maintaining metal contact is challenging.

To compare the wave propagation characteristics of an RWG and a GGW, their propagation constants were simulated using an Eigenmode solver in CST, as illustrated in Figure 3.16. The green and orange walls are clearly marked to indicate the electric ($E_t = 0$) and periodic boundaries, respectively, providing a visual representation of the simulation setup.

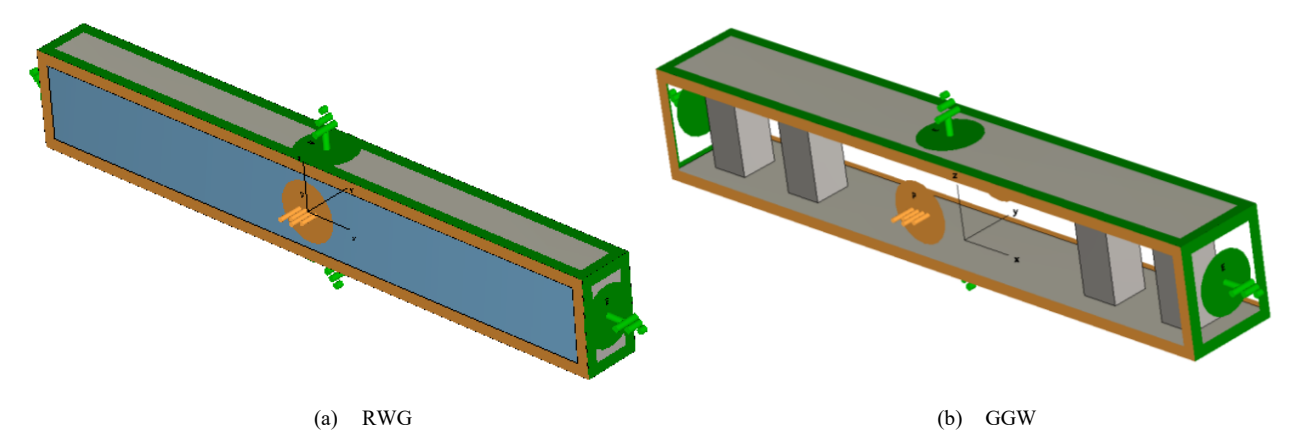


Figure 3.16. Simulated (a) RWG and (b) GGW with the boundary conditions in the Eigenmode Solver

The resulting data is plotted in Figure 3.17 and Figure 3.18, where the graphs are positioned closely to enable a direct visual comparison. This analysis reveals how structural variations influence guided-wave properties. The RWG, which serves as a standard reference, has a well-defined cutoff frequency, and its propagation constant increases monotonically with frequency. The TE_{10} mode, represented by the blue line, is the dominant mode of the RWG. Similarly, the GGW exhibits a comparable propagation trend when analyzed relative to the light line.

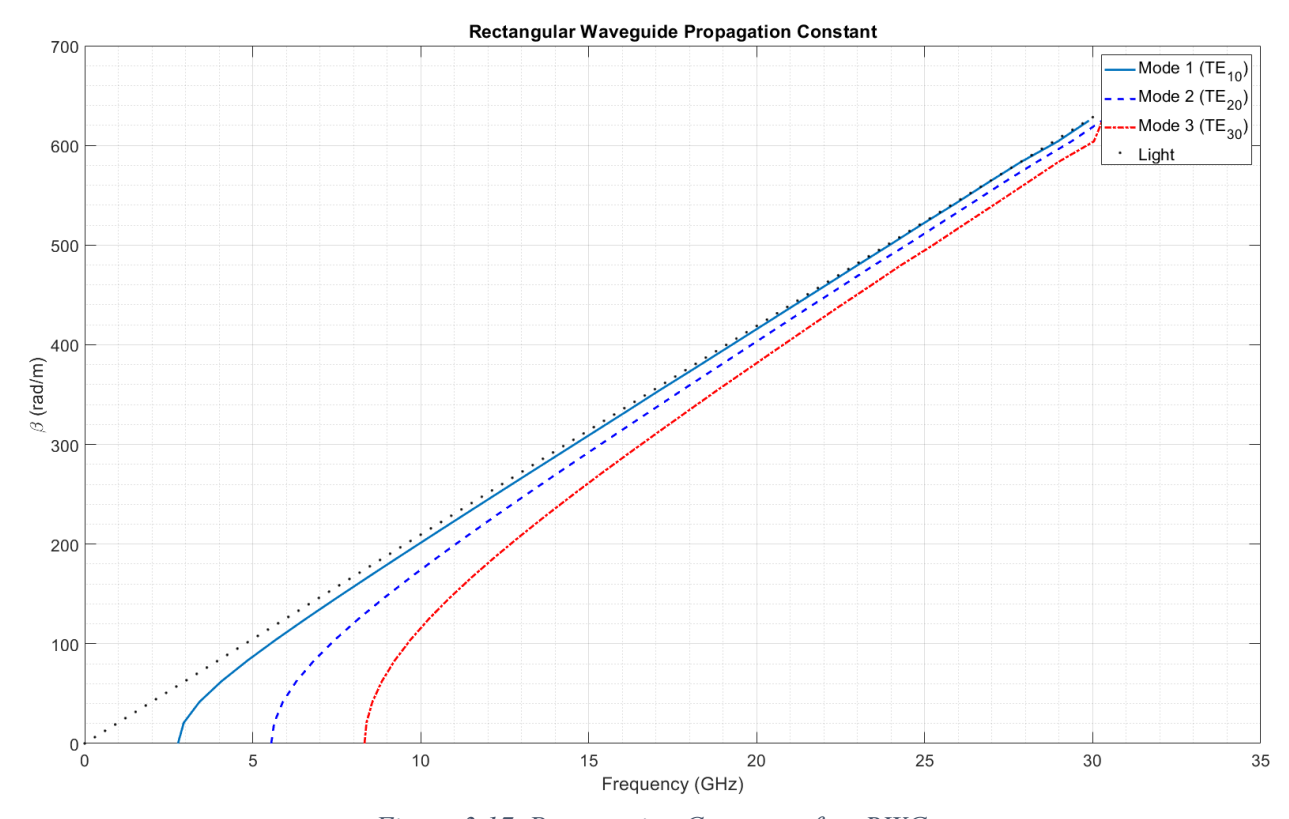


Figure 3.17. Propagation Constant of an RWG

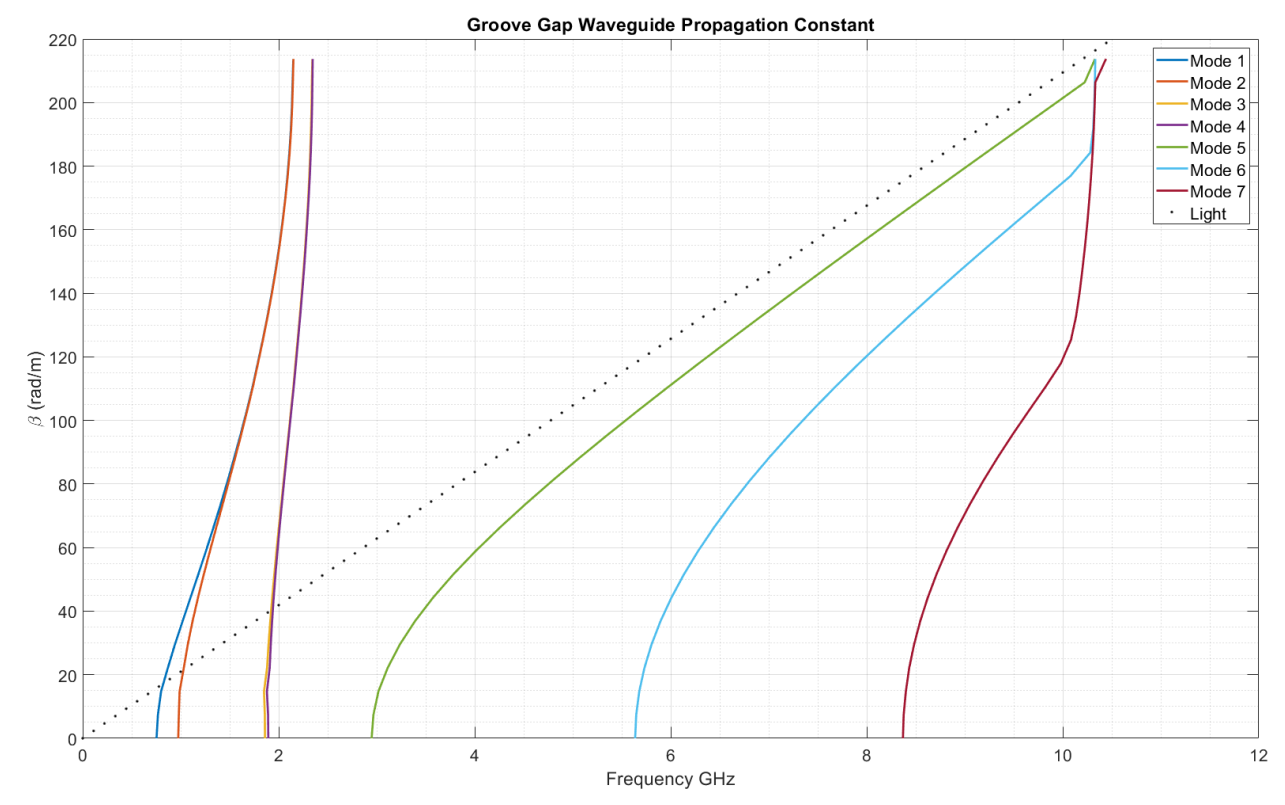


Figure 3.18. Propagation Constant of a GGW

As discussed in previous sections, the primary mode of the GGW is mode 5 (green line), which also corresponds to TE_{10} . Comparing these two structures highlights their respective advantages and constraints in terms of dispersion properties and frequency-dependent wave confinement. Given their similarities, the established relations of the RWG can be used as an initial approximation for further analysis.

The GGW and RWG simulations were conducted using the dimensions specified in Table 3.1.

RWG GGW Description Value (mm) **Description** Value (mm) **Parameter Parameter** 54 5.88 **Broad Wall** Pin Size 14.9 5.8 b Narrow Wall d Pin Height Wall Thickness 1 0.3 t Air Gap Size ag 5 RWG Length Unit Cell Size 14.7 p GGW Width 54 W

Table 3.1. GGW and RGW Dimensions.

3.4. Vertical Transition from Coaxial Cable to GGW:

Efficient transitions between coaxial cables and GGWs are essential for integrating conventional microwave components with modern gap waveguide technology. In this study, a vertical coaxial-to-GGW transition is designed and analyzed, operating within the 3.18–7 GHz frequency range (75 % bandwidth). Unlike conventional horizontal transitions [65], this design leverages a vertical structure to optimize wave coupling while maintaining a compact footprint. The transition aims to minimize reflection losses and ensure impedance matching with a 50-ohm coaxial feed.

Figure 3.19 illustrates the proposed transition, which consists of a coaxial inner pin extending vertically into the GGW, coupled with a metallic plate to enhance impedance matching and wave guidance. The key design parameters include:

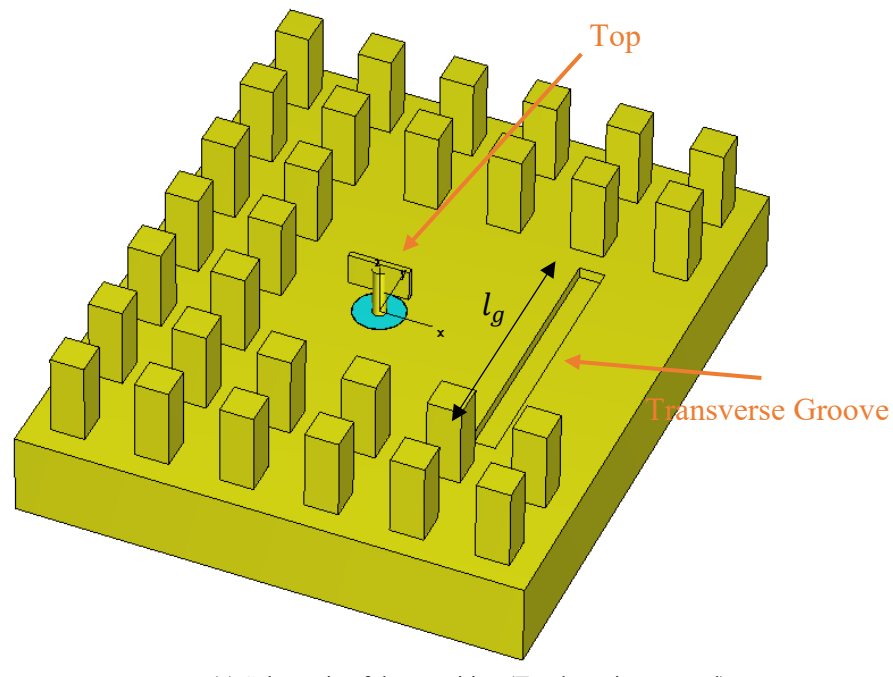
- d_1 : Distance from the coaxial inner pin to the back wall
- l_p : Length of the vertical plate on top of the inner pin
- t_p : Thickness of the metallic plate
- $h_1 \& h_2$: Distances of the lower GGW plate to the bottom and top side of the plate
- d_2 : Distance between the transverse groove and the inner pin conductor
- w_g , l_g , & d_g : Width, length, and Depth of the groove

Most of these dimensions play a crucial role in impedance matching and efficient wave propagation. To optimize performance, a parametric sweep is conducted using CST Studio's Frequency Domain Solver to evaluate their impact.

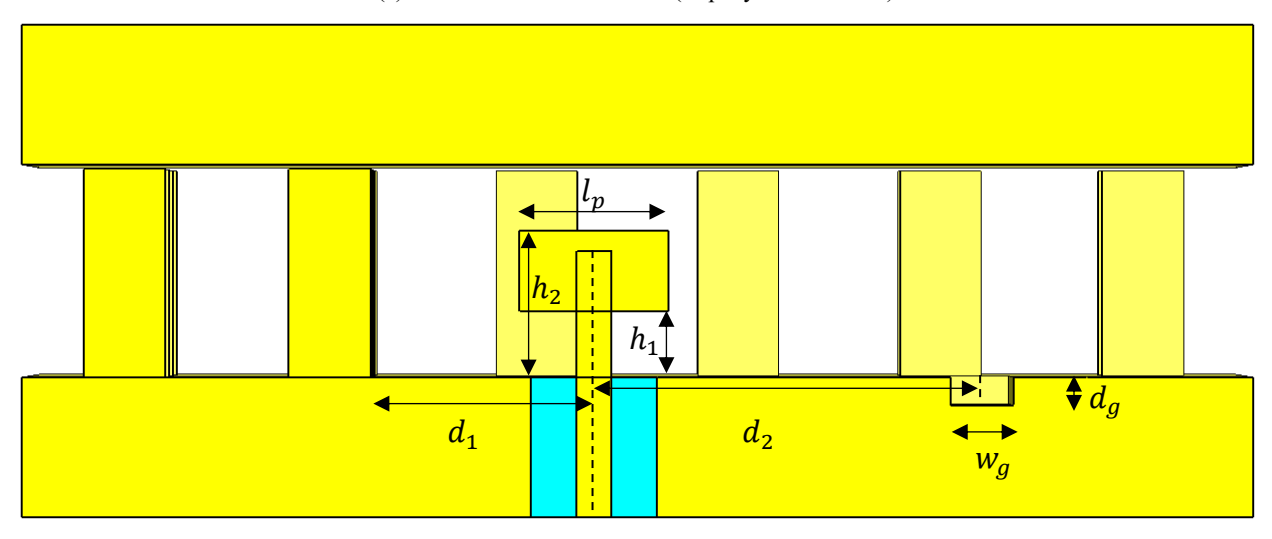
The design incorporates impedance equations to match the 50-ohm system between. The impedance of the coaxial cable is calculated using the equations presented in [83]:

$$Z_{coaxial} = \frac{60}{\sqrt{\varepsilon_r}} \ln \left(\frac{r_{out}}{r_{in}} \right) \tag{3.2}$$

where ε_r represents the relative permittivity of the dielectric filling, r_{out} denotes the inner radius of the outer conductor and r_{in} represents the radius of the inner conductor of the coaxial cable.



(a) Schematic of the transition (Top layer is removed)



(b) Cross-sectional view of the transition.

Figure 3.19. 3D schematic of the transition structure (a) removed-top-layer view and (b) cross-sectional view

The transition is simulated in CST Studio using electric ($E_t = 0$) boundary conditions, ensuring no field exists outside the GGW and coaxial cable, thereby optimizing simulation efficiency. A coaxial wave port is assigned to the input, while a waveguide port is used at the GGW output to monitor transmitted power. The simulation employs a frequency domain solver suitable for broadband analysis and capturing complex field interactions.

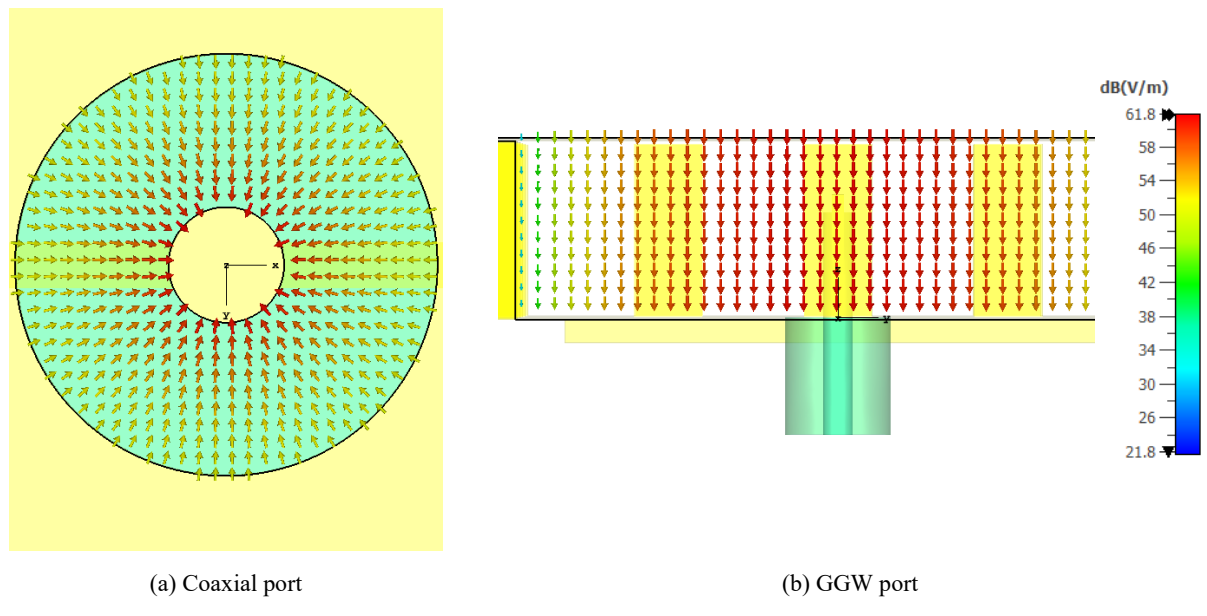


Figure 3.20. Port Electric Field Distribution (a) Coaxial and (b) GGW port

To analyze and compare the port modes excited by this transition, Figure 24(a) and Figure 24(b) depict the port modes of the coaxial cable and GGW, respectively. The structure is designed to naturally excite the TEM mode at the coaxial port and the TE_{10} mode at the GGW port, ensuring efficient mode conversion and minimal reflection.

The TEM mode is the fundamental mode of wave propagation in coaxial cables, where both the electric and magnetic fields are entirely transverse to the direction of propagation. Unlike waveguides, which support higher-order modes with longitudinal field components, the TEM mode ensures uniform energy distribution and non-dispersive propagation across a wide frequency range. This mode is characterized by radial electric field lines extending from the inner conductor to the outer conductor, while the magnetic field forms concentric loops around the inner conductor, governed by Maxwell's equations.

Figure 3.20(a) above illustrates the electric field distribution at the coaxial cable port, clearly depicting the TEM wave characteristics. The radial orientation of the electric field vectors between the inner and outer conductors confirms the expected TEM mode behavior, ensuring efficient power transfer. The symmetry of the field lines minimizes modal distortion, leading to consistent impedance matching. This uniform field distribution is crucial for ensuring a smooth transition from the coaxial port to the GGW while reducing reflection losses. Proper excitation of the TEM

mode at the coaxial port is essential for achieving high-performance coupling into the GGW, as it facilitates seamless mode conversion with minimal energy dissipation.

Given the frequency range of 3 to 7 GHz, the center frequency is determined to be 5 GHz, corresponding to a wavelength (λ_0) of 60 mm. The performance of the transition is simulated based on Table 3.2:

Table 3.2. Coax-to-GGW transition dimensions

Parameter	Description	Value (mm)	Parameter	Description	Value (mm)
a	Pin Size	5.88	d_g	Groove Depth	$0.03\lambda_0$
d	Pin Height	14.9	h_1	Height of the lower side	$0.08\lambda_0$
ag	Air Gap Size	0.3	h ₂	Height of the upper side	$0.175\lambda_0$
p	Unit Cell Size	14.7	l_p	Plate Length	$0.177\lambda_0$
w	GGW Width	54	w_g	Groove Width	$0.075\lambda_0$
d_1	Distance to the Back wall	$0.26\lambda_0$	l_g	Groove Length	$0.76\lambda_0$
d_2	Distance to the transverse groove	$0.463\lambda_0$	t_p	Plate Thickness	$0.16\lambda_0$

The reflection coefficient (S_{11}) and transmission coefficient (S_{21}) are extracted to assess impedance matching and power transfer efficiency. Ideally, S_{11} should be minimized (< -10 dB) over the operating frequency range while S_{21} should remain close to 0 dB. Figure 3.21 illustrates the scattering parameters of the coaxial-to-GGW transition over a frequency range of 3 to 8 GHz. The S_{11} (blue curve) represents the reflection coefficient at the input port (Coaxial Cable Port), indicating how much power is reflected because of impedance mismatch. Ideally, S_{11} should be below -10 dB for good impedance matching, and in this case, it reaches values below -40 dB around 4 GHz and 6 GHz, suggesting highly efficient energy transfer at these frequencies. The operating bandwidth spans from 3.18 GHz to 7 GHz, covering 75% of the center frequency. The S_{21} (red curve) represents the transmission coefficient, showing the power successfully transmitted to the GGW. Since S_{21} remains close to 0 dB across most of the frequency range, demonstrating excellent power transmission with minimal loss. The two deep nulls in S_{11} indicate frequencies where near-perfect impedance matching occurs, making these regions optimal for operation.

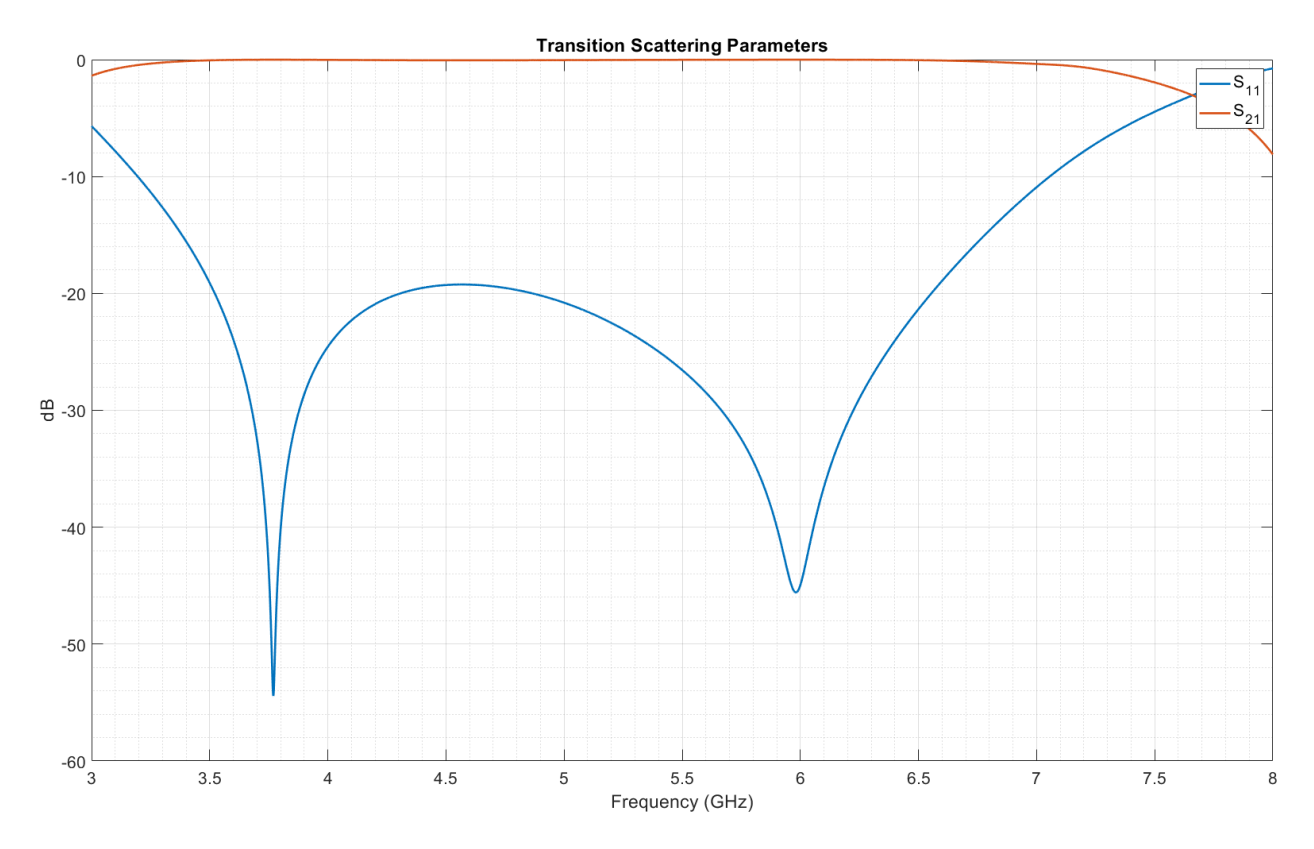


Figure 3.21. S-parameter plot showing S_{11} and S_{21} over frequency.

The transition region's electric and magnetic field distributions are analyzed to visualize wave propagation and identify potential losses or mismatches.

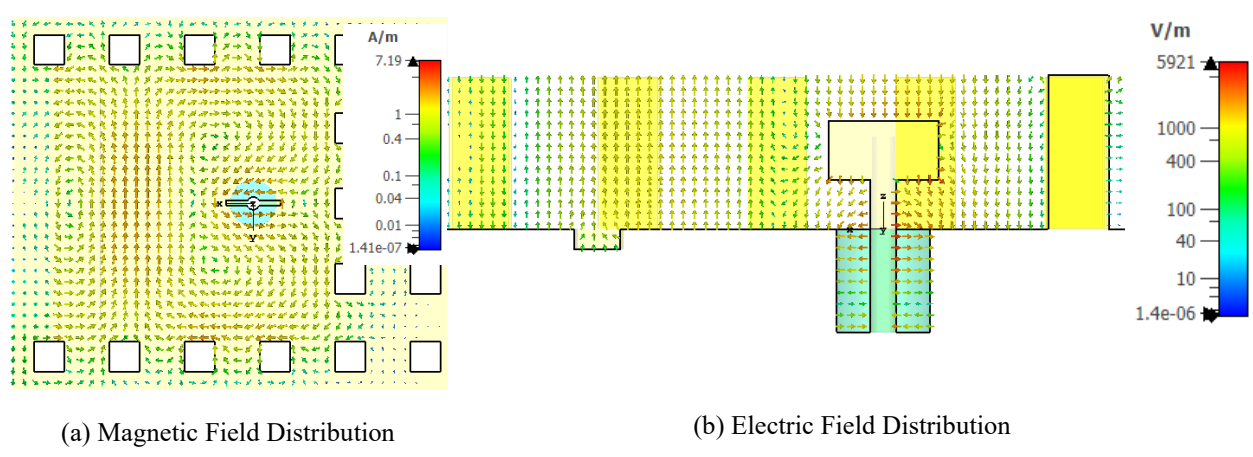


Figure 3.22. Electromagnetic Field Distribution

Figure 3.22 presents the cross-sectional view of the magnetic and electric field distributions in the coaxial-to-GGW transition. The field vectors illustrate the magnetic and electric field intensities

and directions, revealing the interaction between the coaxial feed and the GGW structure. The arrangement of the periodic pins (EBG structure) suggests the presence of artificial magnetic conductors (AMCs), which help confine and guide the electromagnetic waves within the GGW. The circular magnetic field patterns around the central region indicate strong coupling between the coaxial pin and the GGW, ensuring efficient mode conversion. The gradient in the field intensity, transitioning from stronger near the coaxial port to weaker toward the outer regions, highlights the gradual energy transfer into the GGW mode. This visualization confirms the proper excitation of the desired mode and provides insight into possible field leakage or confinement issues in the design.

Parametric Analysis

A parametric sweep is conducted to study the effect of each dimension (d_1, l_p, h_1, h_2) on the transition performance. This analysis helps fine-tune the design for optimal broadband response.

Figure 3.23 represents the S_{11} for different values of d_1 , which is the distance from the inner pin to the back wall within the 3 to 8 GHz frequency range. As indicated in the legend, each curve corresponds to a different value of d_1 , ranging from 6 mm to 20 mm.

The distance d_1 significantly influences impedance matching in the coax-to-GGW transition. The plot reveals that certain d_1 values achieve improved matching with reduced reflections, while others result in increased reflections, signalling suboptimal matching. Specifically, a shorter d_1 range of 6–10 mm leads to a considerable mismatch, as indicated by elevated reflection levels across the frequency band. However, as d_1 extends to 12–18 mm, the matching enhances noticeably, with marked reductions in reflection at specific frequencies, demonstrating better performance.

Optimal impedance matching is achieved when $d_1 \approx 15$ mm, corresponding to roughly $\lambda_0/4$ at the center frequency of 5 GHz. At this $\lambda_0/4$ distance, the reflected wave at the inner pin aligns inphase, resulting in constructive interference that maximizes power transfer and significantly reduces return loss.

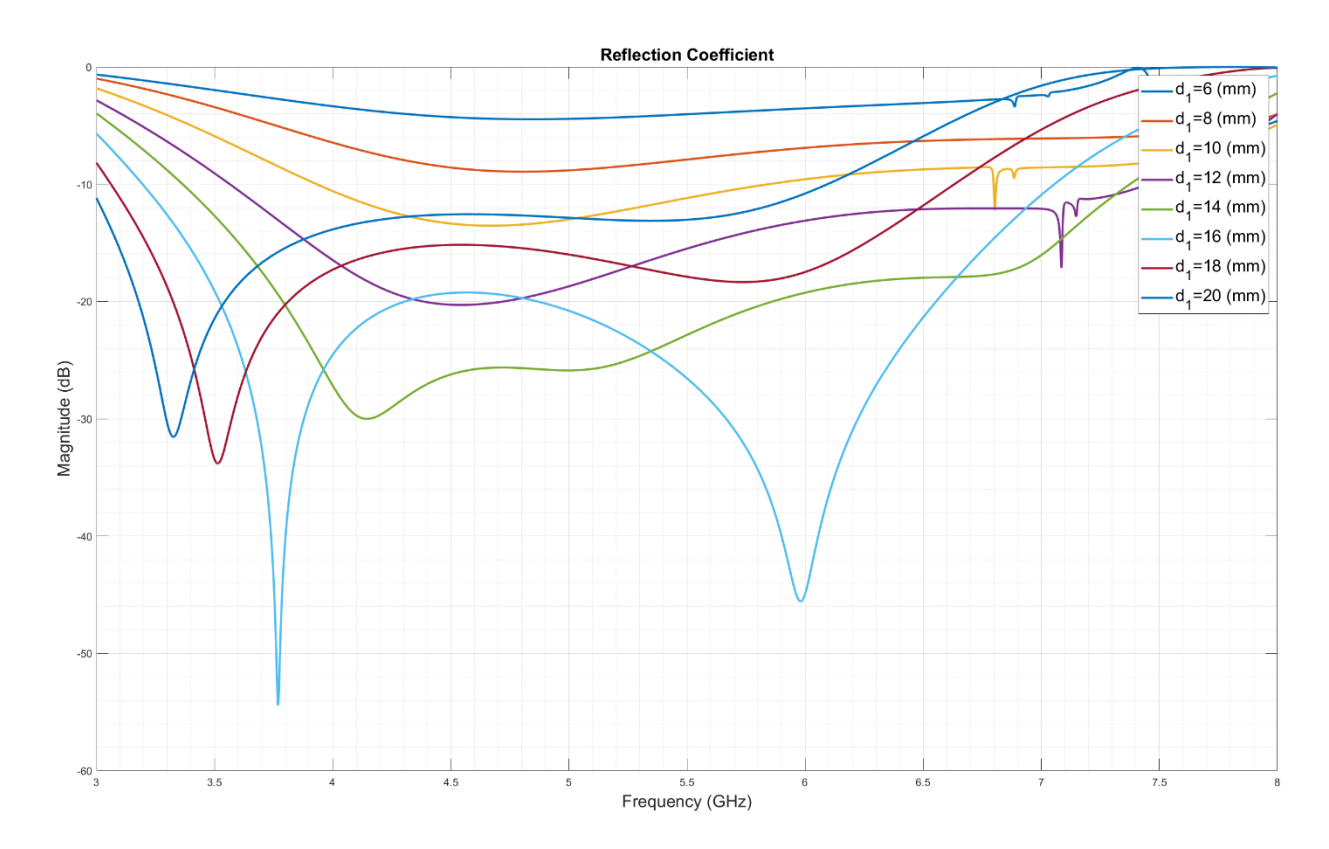


Figure 3.23. S_{11} of Sweep Parameter d_1

When d_1 exceeds 15 mm, reflections rise as the transition deviates from the optimal impedance transformation point. This indicates that surpassing $\lambda_0/4$ alters the phase relationship between the incident and reflected waves, resulting in increased reflections.

Although optimal matching at approximately 15 mm minimizes reflection at specific frequencies, practical applications often demand a broadband response with consistently low reflection across the entire frequency range. The findings suggest that a moderate range of $d_1(14 - 16 \text{ mm})$ may be more suitable for achieving effective broadband performance.

This sweeping analysis highlights that the distance from the inner pin to the back wall (d_1) has a significant impact on impedance matching in the coaxial-to-GGW transition. The best matching occurs at approximately $\lambda_0/4$ (~15 mm), where the reflected wave at the pin is in phase, minimizing return loss. Adjusting d_1 properly is crucial to optimizing the transition for both narrowband and broadband applications.

Figure 3.24 presents the S_{11} for various values of the plate length (L_p) at the tip of the inner conductor, covering a frequency range of 3 to 8 GHz. Each curve represents a different L_p value, ranging from 3 mm to 15 mm, as indicated in the legend.

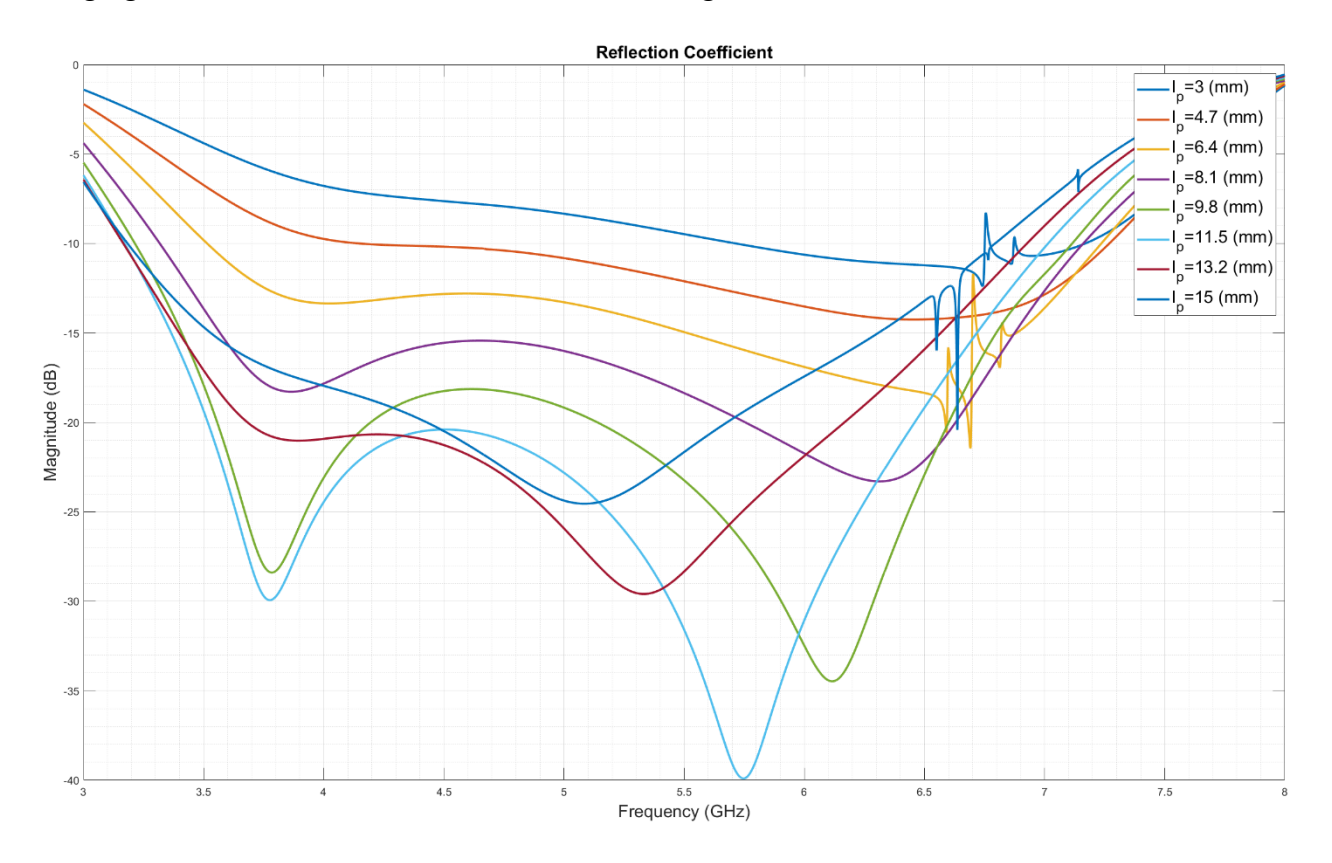


Figure 3.24. S_{11} of Sweep Parameter l_p

The plate length (L_p) is crucial in impedance matching, as evidenced by the varying reflection levels across frequencies. Certain L_p values substantially lower reflection, signifying enhanced impedance matching and more efficient energy transfer. Conversely, other L_p values result in increased reflections, indicating mismatched conditions that hinder performance.

Optimal impedance matching is achieved with L_p values ranging from approximately 9.8 mm to 13.2 mm, where the S_{11} exhibits deep nulls, indicating low reflection. Notably, the light blue curve $(L_p = 9.8 \text{ mm})$ and the red curve $(L_p = 13.2 \text{ mm})$ demonstrate the lowest reflections, signifying that the structure is effectively matched at these lengths. These pronounced dips reflect minimal energy reflection, ensuring efficient energy transfer to the GGW.

For shorter plate lengths ($L_p = 3 - 6.4 \ mm$), such as $L_p = 3 \ mm$ and 4.7 mm, the corresponding curves exhibit elevated reflection levels across the frequency range. This indicates that shorter L_p values fail to achieve sufficient impedance transformation, resulting in a significant portion of the energy being reflected back into the coaxial port. For longer plate lengths, such as $L_p = 15 \ mm$, the corresponding curve indicates a rise in reflection at higher frequencies. This implies that overly extended plate lengths may cause unwanted resonances or phase mismatches, thereby decreasing the efficiency of the transition.

The reflection minima exhibit a slight shift across frequencies, indicating that the impact of L_p on impedance matching is frequency-dependent. Optimal broadband performance is achieved with L_p values ranging from 9.8 mm to 13.2 mm, where the return loss remains consistently low across a broader frequency range.

The sweep results highlight the significant impact of the plate length (L_p) at the inner conductor's tip on impedance matching. Optimal matching is achieved with L_p values between 9.8 mm and 13.2 mm, where reflection is minimized, thereby enhancing power transfer efficiency. Conversely, very short $(L_p = 3 - 6.4 \text{ mm})$ or very long $(L_p = 15 \text{ mm})$ plate lengths result in higher reflections and diminishing performance. Selecting an appropriate L_p is essential for ensuring a well-matched broadband transition to the Groove Gap Waveguide (GGW). This analysis informs the transition design by guiding the optimization of L_p to minimize return loss and maximize energy transfer efficiency. The figure consists of two subplots showing the S_{11} for different values of h_1 (lower side height of the plate) and h_2 (upper side height of the plate), with frequency varying from 3 GHz to 8 GHz.

Figure 3.25(a) illustrates the S_{11} for h_1 values ranging from 0.1 mm to 10 mm. As h_1 increases, the impedance-matching behavior shifts, altering the frequency at which the minimum reflection occurs. Optimal impedance matching is achieved at $h_1 \approx 8.5mm$ (red curve), exhibiting a deep null around 3.5 GHz with a reflection level below -40 dB. Conversely, when h_1 is either too small (0.1 mm, blue curve) or too large (10 mm, dark blue curve), the reflection levels rise significantly, indicating poor impedance matching.

The sweep of h_1 reveals distinct impedance-matching trends across its range. For very small h_1 values (0.1–2.9 mm), the matching is poor, resulting in high reflection across the frequency band.

In contrast, moderate h_1 values (4.3–8.5 mm) exhibit good matching with significantly reduced reflections, with the best performance observed at $h_1 \approx 8.5$ mm. However, when h_1 becomes too large (e.g., 10 mm), the matching degrades, leading to increased reflection levels.

Figure 3.25(b) displays the S_{11} for h_2 values ranging from 7 mm to 15 mm. As h_2 increases, the dips in the S_{11} shift across frequencies. Optimal matching is achieved at $h_2 \approx 10.4$ mm (purple curve), where deep nulls are observed around 6 GHz, with a reflection level below -40 dB. However, larger h_2 values, such as 15 mm (blue curve), result in elevated reflections at lower frequencies.

The sweep of h_2 reveals varying impedance-matching performance across its range. For smaller h_2 values (7–9.2 mm), the reflection reduction is moderate but falls short of optimal performance. At h2 = 10.4 mm, the structure exhibits strong impedance matching, characterized by a deep null in reflection. However, larger h_2 values (13.8–15 mm) lead to increased reflection, which diminishes the overall performance of the transition.

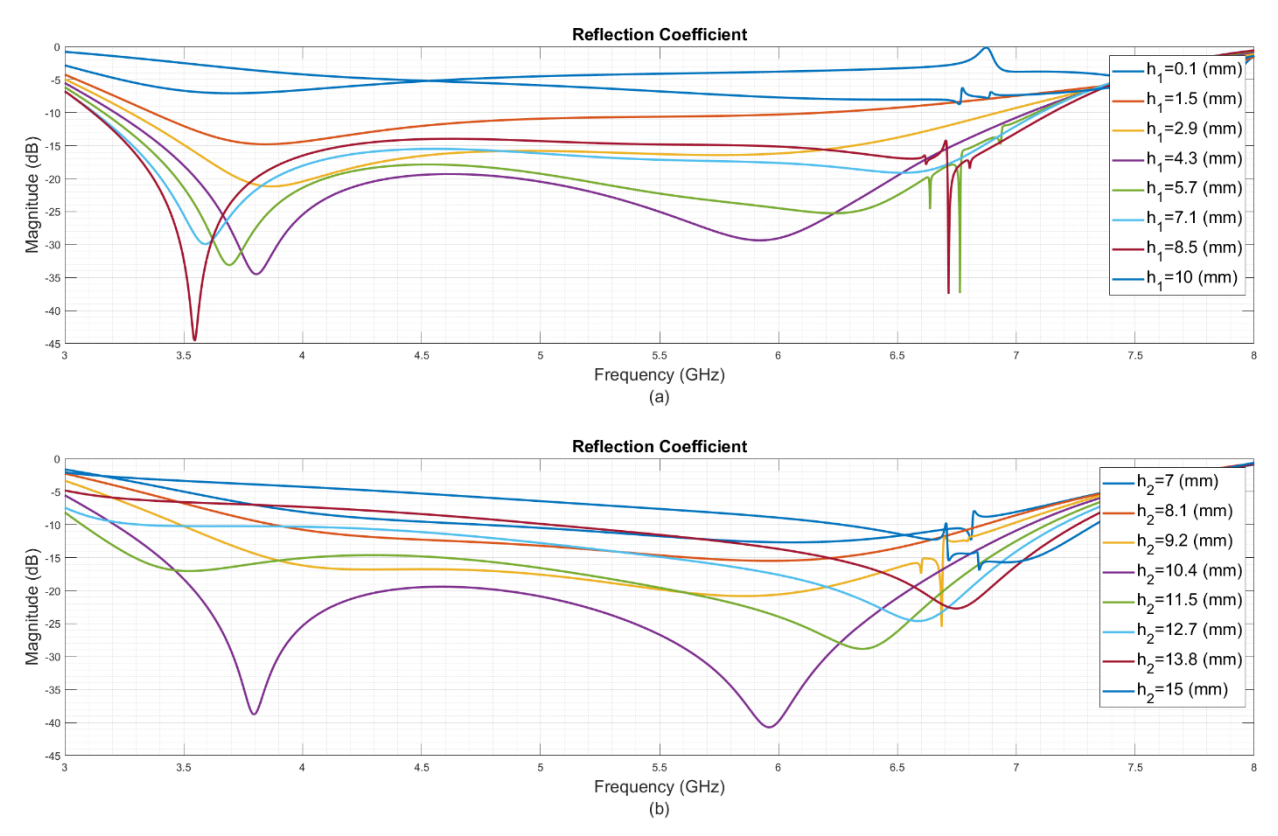


Figure 3.25. S_{11} of Sweep Parameters $h_1 \& h_2$

The heights h_1 and h_2 play a critical role in impedance matching by shaping the electromagnetic field distribution within the transition. Optimal values of $h_1 \approx 8.5 \ mm$ and $h_2 \approx 10.4 \ mm$ yield the best impedance matching, effectively minimizing reflections and enhancing power transfer. Deviations to either excessively small or large values lead to suboptimal impedance matching, resulting in increased signal reflection.

This study underscores the importance of precisely tuning h_1 and h_2 to ensure efficient energy transfer in the coaxial-to-GGW transition. Optimal impedance matching is achieved at $h_1 = 8.5 \, mm$ and $h_2 = 10.4 \, mm$, resulting in a substantial decrease in the S_{11} . Deviations from these values lead to diminished performance, highlighting the critical role of proper height selection in the design process. Figure 3.26 presents three subplots showing the S_{11} as a function of frequency. The impact of different geometric parameters on the impedance matching and bandwidth of the coaxial-to-GGW transition is studied: As d_2 (Distance of the transverse groove to the inner pin of the coaxial cable) increases, the resonance exhibits a slight shift, influencing the S_{11} . While the depth of the notch varies with this change, there is no notable improvement in bandwidth observed.

Variations in l_g exhibit a slight impact on the S_{11} , with the lowest reflection levels observed at intermediate values. However, these changes do not significantly affect the bandwidth.

Changes in d_g have a noticeable effect on impedance matching, with variations impacting the reflection characteristics. Nevertheless, the bandwidth remains relatively consistent across different d_g values.

None of these parameters significantly enhances bandwidth individually. However, they can improve impedance matching and bandwidth performance when optimized together. The interaction between these parameters must be considered carefully to achieve a better trade-off between matching quality and bandwidth expansion.

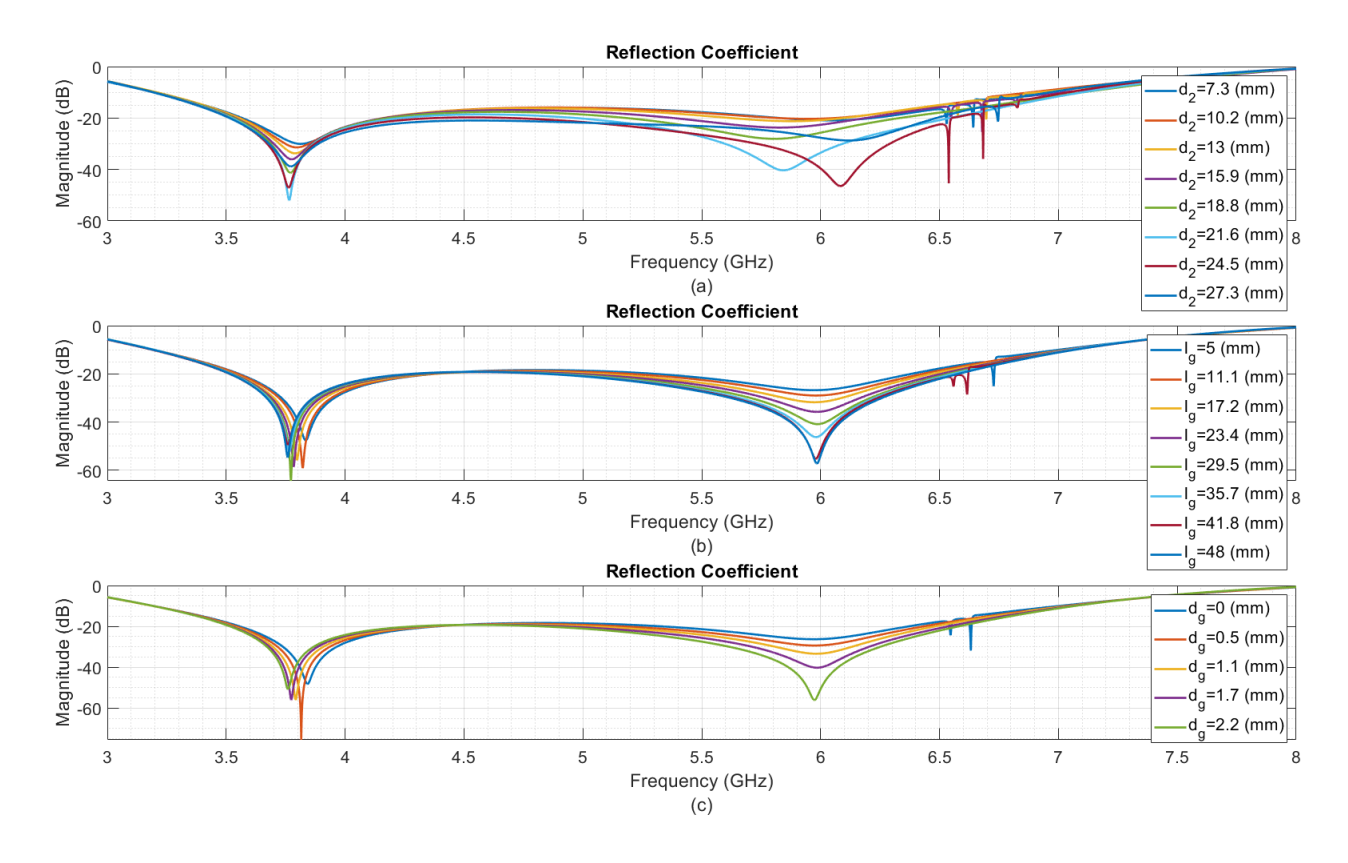


Figure 3.26. S_{11} of Sweep Parameters d_2 , $l_g \& d_g$

Discussion and Comparison

While horizontal coaxial-to-GGW transitions have been explored in previous studies, vertical transitions remain under investigation [65]. The proposed design offers advantages such as compact size and enhanced mode coupling, making it a promising candidate for practical implementations. Future work could compare it with existing horizontal designs to highlight the trade-offs.

Conclusion

This section presents a vertical coaxial-to-GGW transition that has been optimized using CST simulations. The parametric analysis provides insights into the influence of key design parameters, ensuring efficient impedance matching and minimal reflection losses. Future work can focus on experimental validation and further miniaturization.

Chapter IV:

Transverse Slot Antenna Based on GGW

4.1. Introduction

Slot antennas based on GGW technology have emerged as a promising solution for high-frequency applications, particularly in MMW communications. GGW technology offers several advantages, including reduced manufacturing complexity, high radiation efficiency, and maintaining performance despite fabrication tolerances. These features make GGW-based slot antennas highly suitable for 5G and other advanced communication systems.

GGW technology facilitates low insertion losses and high radiation efficiency, which are critical for achieving optimal signal transmission and reception [84], [85]. Using metal pin arrays in GGW slot antennas further enhances gain, improving symmetry in radiation patterns [85].

Moreover, GGW technology simplifies the fabrication process by eliminating the need for electrical contact between metal layers, thus reducing costs and mechanical complexity [67]. This contactless feature is particularly advantageous in the design of complex antenna structures, such as multi-layered arrays and power dividers, which are essential for high-gain applications [67], [86]. The ability to achieve wide operational bandwidths and maintain high radiation efficiency across a broad frequency range further underscores the versatility of GGW-based slot antennas [67], [87].

In summary, GGW-based slot antennas offer a robust and efficient solution for modern communication systems, providing high gain, wide bandwidth, and ease of fabrication. These attributes make them attractive for applications ranging from 5G networks to satellite communications and radar systems. This chapter comprehensively analyzes the GGW slot antenna with the coax-to-GGW transition, including its structure, operation, and performance characteristics.

4.2. Design and Analysis of a Simple Single-Groove Gap Waveguide Slotted Antenna

The implemented coax-to-GGW transition functions as the feeding mechanism for the slot antenna, as depicted in Figure 4.1(a) and (b), which present the 3D model and cross-sectional view, respectively. The S_{11} , gain, and the front-to-back ratio of the proposed antenna are illustrated in Figure 4.1(c).

The top panel shows a 3D rendering of the GGW antenna, depicted in yellow to represent a metallic structure (Copper). The design includes an upper flat plate with a single transverse slot, labelled " L_r " (slot length), positioned centrally over the groove and the plate, W_t (Upper plate width), and l_t (Upper Plate Length).

Figure 4.1 (b) presents a cross-sectional view, illustrating key components: the transverse slot width w_r , the distance from the coax inner pin to the front wall (d_3) , and the distance from the slot center to the front wall (d_4) . The EBG structures, consisting of pins on both sides of the groove (at the back and front walls), effectively maintain the stopband to suppress unwanted modes.

The transverse slot, centrally aligned over the groove, disrupts the quasi-TE mode currents to facilitate radiation. This view also underscores the contactless design of the GGW, with the upper and lower plates separated by an air gap, simplifying fabrication. A coaxial feed is also inferred, likely transitioning into the GGW via a probe or aperture at the groove's input.

Figure 4.1 (c) presents simulated results for the antenna's performance, plotted versus frequency 3–8 GHz. The black curve depicts the S_{11} in decibels (dB), reflecting the antenna's impedance matching with the feed. It reveals a minimum S_{11} of approximately -23 dB at around 3.3 GHz and 4 GHz, signifying effective matching at these frequencies. The bandwidth where $S_{11} < -10 \, dB$ extends from approximately 3.1 GHz to 4.6 GHz, yielding a 39% bandwidth, which indicates a narrowband design well-suited for targeted applications in the microwave or low-MMW frequency range.

The red curve represents the antenna gain in decibels (dBi), rising from approximately 4.6 dBi at 3 GHz to about 7 dBi at 4.6 GHz. This consistent gain increase with frequency indicates enhanced radiation efficiency at higher frequencies within this range, likely attributed to improved aperture efficiency.

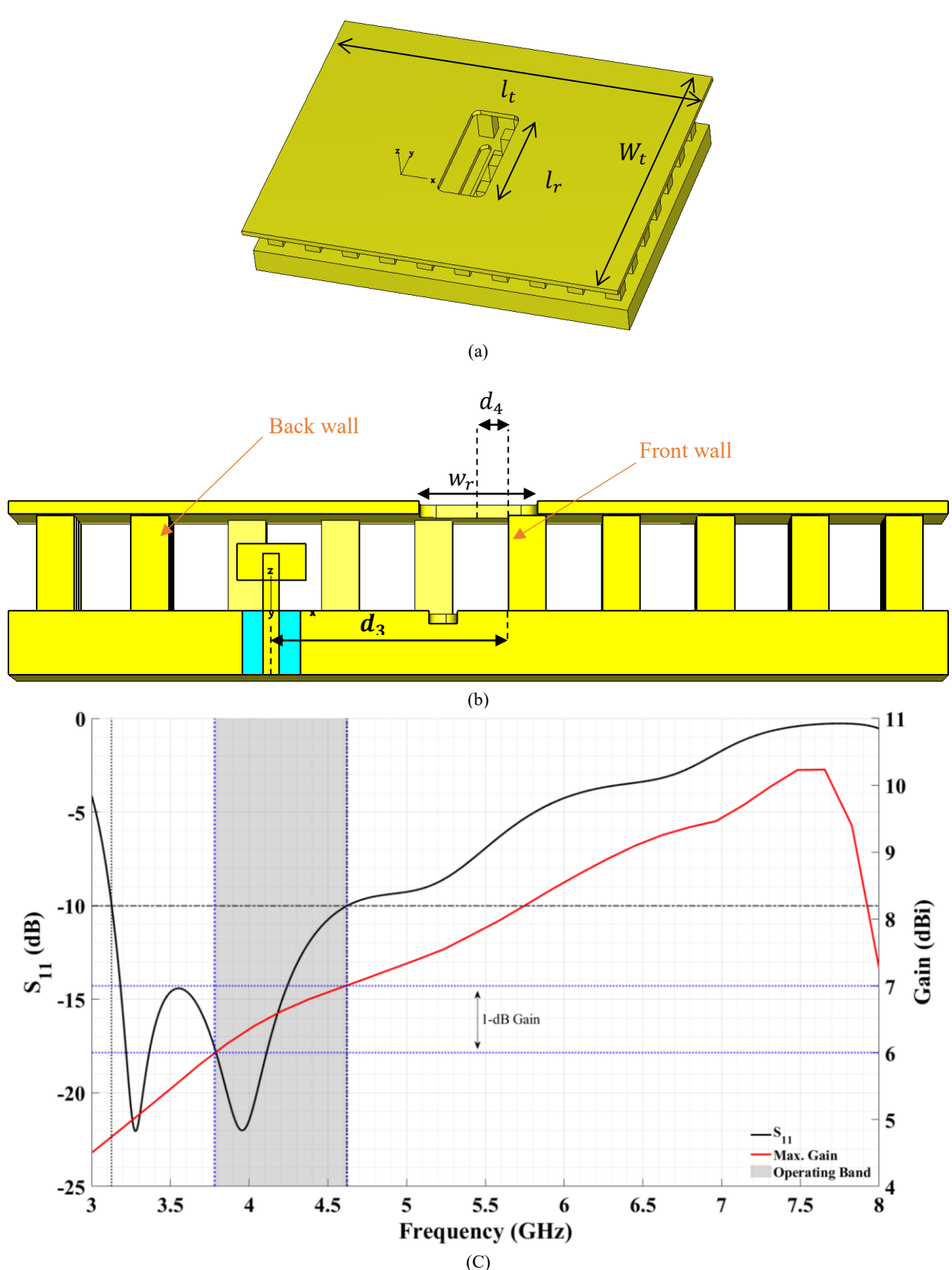
The 1-dB gain bandwidth and the impedance matching bandwidth effectively overlap, indicating a cohesive operating frequency band of 21.6%. This operating frequency range is clearly delineated by the gray shaded area in the provided plot from 3.7 GHz to 4.6 GHz, where the antenna achieves a maximum gain of 7 dB at the end of the matching impedance bandwidth.

The 3–8 GHz range suggests this design targets low-MMW or high-microwave applications, possibly for 5G sub-6 GHz bands or extended C-band systems. The resonance at 3.2 GHz aligns with the slot length ($L_r \approx \lambda_0/2$ at 3.2 GHz, where $\lambda_0 = \frac{c}{f_0} = 93.75 \, mm$, so $L_r \approx 46.875 \, mm$). The dimensions of the simulated model are listed in Table 4.1.

Table 4.1. Transverse slotted GGW antenna dimensions (Figure 4.1)

Parameter	Description	Value (mm)	Parameter	Description	Value (mm)
d_3	Inner Pin's Center to the front wall	36.92	l_t	Upper layer Length	146.52
d_4	Slot's center to the front wall	4.65	t_t	Upper layer Thickness	2
w_r	Slot Width	18.5	w_t	Upper layer Width	60
l_r	Slot Length	46			

The coaxial probe or aperture at the groove's input transitions the coax's TEM mode to the GGW's quasi-TE mode. Using the dimensions from the previous chapter, this transition must be optimized to minimize reflections. The EBG structures (pins) ensure mode confinement, reducing leakage and enabling the high front-to-back ratio observed.



(C)
Figure 4.1. (a) Simulated 3D of the GGW slotted antenna, (b) Cross-sectional view, and (c) S11, Gain, and the front-to-back ratio of the antenna

4.3. Design and Analysis of a Groove Gap Waveguide Slotted Antenna with Rectangular Corrugations

Building on the simple GGW slotted antenna, this section explores a modified design incorporating rectangular corrugations on the top layer to enhance performance, targeting the frequency range of 3.2–7.2 GHz. The GGW structure retains the same groove dimensions and EBG parameters as those in Section 4.2, which are optimized for the target frequency band. The single transverse slot remains unchanged, with dimensions $L_r = 46 \ mm$ and $W_r = 18.5 \ mm$, ensuring continuity with the baseline design.

Rectangular corrugations are introduced on the upper plate, parallel to the transverse slot, to increase the impedance bandwidth and antenna gain. Figure 4.2 provides a cross-sectional view of the corrugated GGW slotted antenna, showing the groove, EBG pins, transverse slot, and the rectangular corrugations on the top layer.

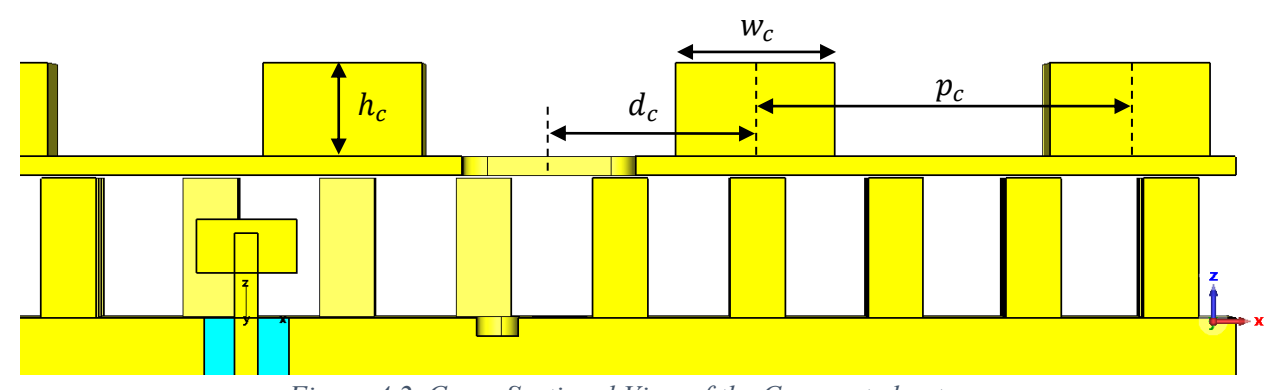


Figure 4.2. Cross-Sectional View of the Corrugated antenna

The corrugation design is specified in Table 4.2:

Table 4.2. Corrugation Dimensions

Parameter	Description	Value (mm)	Parameter	Description	Value (mm)
d_c	Slot center to Corrugation Center	22	h_c	Corrugation height	10
p_c	Corrugation periodicity	40	w_c	Corrugation Width	17

These corrugations modify the surface current distribution and electromagnetic field patterns, aiming to broaden the operational bandwidth and enhance radiation efficiency [75]. The design is

simulated using CST Studio, following the same methodology as in Section 4.2, to evaluate the antenna's S_{11} , gain, and radiation pattern over the 3.2–7.2 GHz range.

The simulated performance metrics, based on the provided radiation pattern, gain, and S_{11} plots are analyzed as follows: The S_{11} , represented by a red curve in Figure 4.3, indicates that $S_{11} < -10 \, dB$ over the expanded bandwidth of 3.2–5.6 GHz, a significant improvement over the simple slot's 3.1–4.6 GHz range. This 54% impedance bandwidth demonstrates the effectiveness of the corrugations in mitigating impedance mismatches and broadening the operational frequency range.

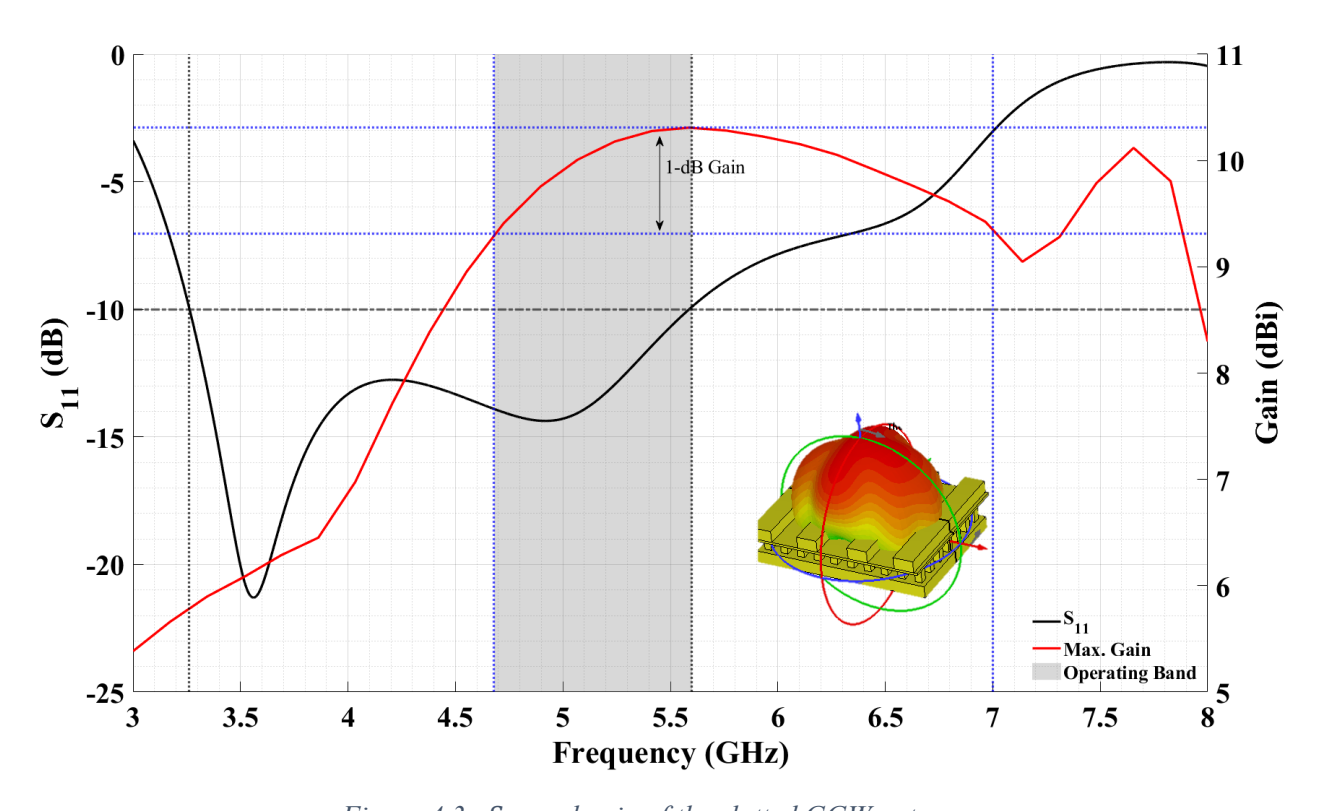


Figure 4.3. S_{11} and gain of the slotted GGW antenna.

The gain, depicted by a dashed blue curve in Figure 4.3, increases to 10.5 dBi at approximately 5.5 GHz (the midpoint of 3.2–7.2 GHz), surpassing the 7 dBi of the simple slot at 5.5 GHz.

The antenna's operational frequency range, depicted by the gray shaded area, spans from 4.7 GHz to 5.6 GHz. This bandwidth is constrained at its lower and upper ends by the 1-dB gain bandwidth, resulting in an overall operating bandwidth of 17.5%.

The radiation pattern of the GGW slotted antenna with rectangular corrugations, illustrated in Figure 4.4(a) and (b), exhibits a broadside pattern with horizontal polarization, consistent with the

transverse slot orientation. The corrugations contribute to a more directive pattern, reducing sidelobes, which reach approximately 33 dB at 5.5 GHz, as shown by the solid blue curve in Figure 4.3.

Figure 4.4(a) shows the radiation pattern at $\phi = 0^{\circ}$, revealing a similar broadside characteristic but with slight variations in beam shape due to the polarization orientation. The pattern maintains high directivity with minimal back radiation at 5.5 GHz.

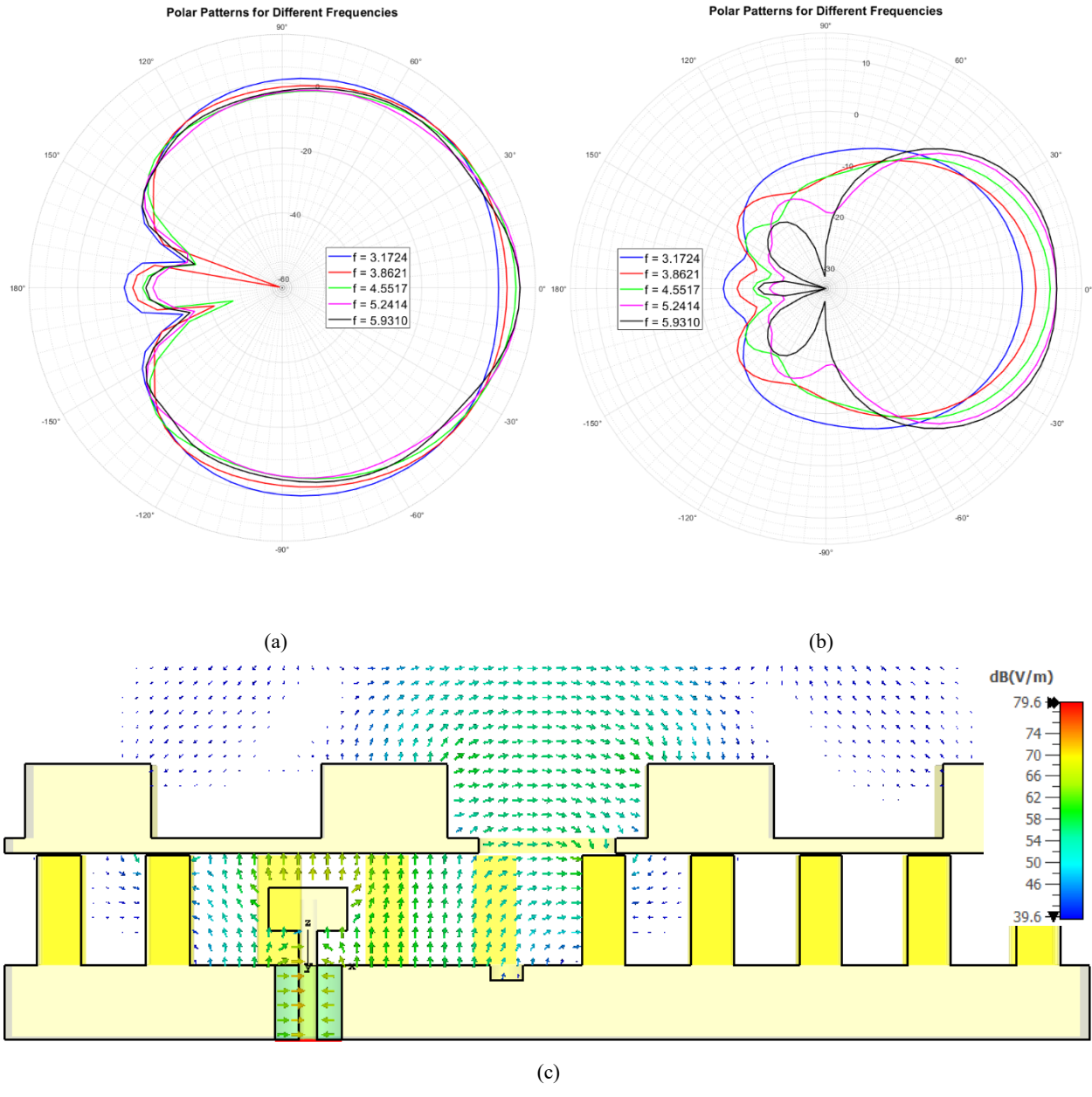


Figure 4.4. Simulated Results of Corrugated Antenna: polar radiation pattern at (a) $\phi = 0^{\circ}$ and (b) $\phi = 90^{\circ}$ at different frequencies. (c) E-Field distribution at 3.9 GHz

Figure 4.4(b) presents polar radiation patterns at $\phi = 90^{\circ}$ for different frequencies within the 3.2–7.2 GHz range, including 3.1724 GHz (blue), 3.8621 GHz (red), 4.5517 GHz (green), 5.2414 GHz (purple), and 5.9310 GHz (black). These patterns demonstrate consistent broadside radiation with maximum gain directed at $\theta = 0^{\circ}$, and a gradual narrowing of the beamwidth as the frequency increases, indicating improved directivity at higher frequencies. The maximum gain ranges from approximately 5.6 dBi at 3.1724 GHz to 10.2 dBi at 5.9310 GHz, aligning with the gain curve in Figure 4.3.

Figure 4.4(c) presents the E-field distribution at 3.9 GHz, illustrating the electromagnetic field concentration within the GGW structure. The E-field is strongest around the slot and corrugations.

This distribution confirms the effective radiation from the slot and the role of corrugations in shaping the field pattern, enhancing directivity and bandwidth.

Comparison of Simple and Corrugated GGW Slotted Antennas

This subsection compares the performance of the simple single GGW slotted antenna with the corrugated version to assess the impact of the rectangular corrugations. The simple slot achieves $S_{11} < -10 \ dB$ from 3.1–4.6 GHz, yielding a 38% bandwidth. In contrast, the corrugated design extends this to 3.2–7.2 GHz, offering a 54% bandwidth—a substantial improvement due to the corrugations' effect on surface currents and field distribution, as evidenced by the S_{11} in Figure 4.3. The simple slot exhibits a gain of 7 dBi at 5.5 GHz, while the corrugated version achieves 10.3 dBi at 5.5 GHz, reflecting increased radiation efficiency from the corrugations' focusing effect, as shown in Figure 4.3. Both designs produce broadside radiation patterns, but the corrugated version offers improved directivity and a higher gain, reducing back radiation and enhancing performance for directional applications, as illustrated by the polar patterns in Figure 4.4(a) and (b).

This comparison highlights the effectiveness of rectangular corrugations in broadening the operational bandwidth and increasing gain, making the corrugated GGW slotted antenna more versatile for wideband, high-gain applications in the 3.2–5.6 GHz range.

4.4. Design and Analysis of a Groove Gap Waveguide Slotted Antenna with a Step Under the Slot

This section presents an advanced modification to the GGW slotted antenna with rectangular corrugations. A step is introduced under the slot at the transition point from the GGW to the slot to further improve the antenna's bandwidth. Building on the design described in Section 4.2, a step is added to the lower plate beneath the transverse slot, as illustrated in Figure 4.6. This step modifies the electromagnetic field distribution and impedance matching to enhance the operational bandwidth.

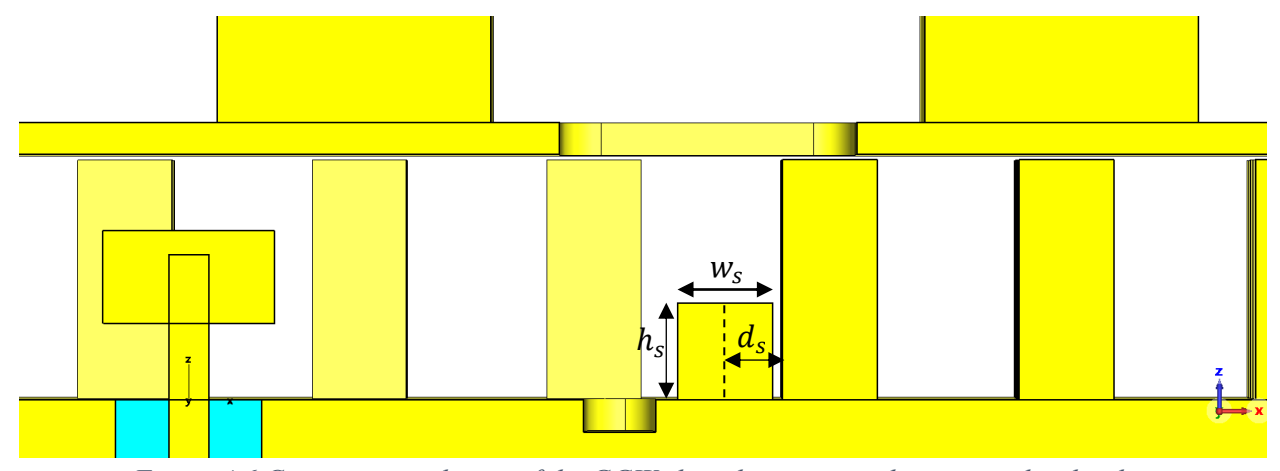


Figure 4.6. Cross-sectional view of the GGW slotted antenna with a step under the slot.

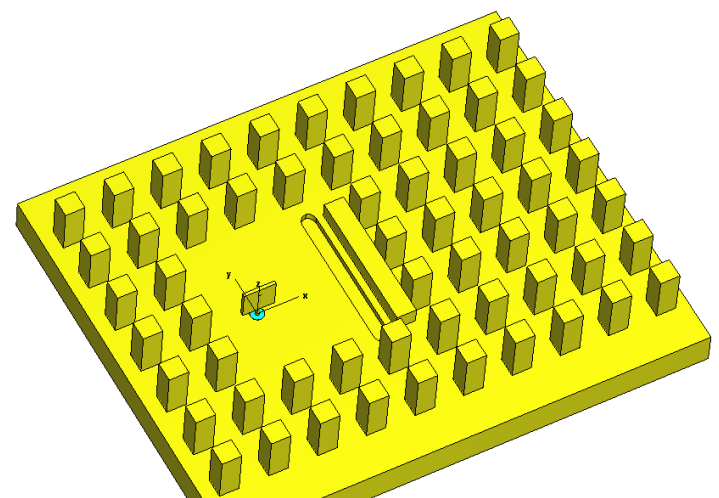


Figure 4.5. Top view of the stepped GGW slotted antenna (Top layer is hidden)

The step is integrated into the groove structure at the slot location, altering the groove height locally to create a discontinuity that broadens the impedance bandwidth. Based on the cross-sectional view in Figure 4.6, the step appears to reduce the groove height under the slot, potentially

by $0.1\lambda_0$, depending on the specific design parameters. The GGW structure, slot dimensions ($L_r=46~mm$ and $W_r=18.5~mm$), and corrugations (height 10 mm, width 17 mm, periodicity 40 mm) remain unchanged from Section 4.3, maintaining continuity with the previous design. The step dimensions are $l_s=41.16~mm$, $w_s=5.88~mm$, $h_s=6~mm$, and $d_s=3.59~mm$.

Simulations using CST Studio demonstrate that adding the step significantly enhances the impedance bandwidth. The S_{11} , represented by a black curve in Figure 4.7, achieves $S_{11} < -10$ over an impressive 77% impedance bandwidth, corresponding to approximately 3.2–7.2 GHz within the 3–8 GHz range shown in the plot. This improvement is attributed to the step's effect on the field distribution, which reduces reflections and broadens the frequency response.

The gain, depicted by a red dashed curve in Figure 4.7, ranges from 5.5 to 10.3 dBi across the bandwidth, maintaining performance comparable to the corrugated design, with a peak of about 10.3 dBi at 5.5 GHz.

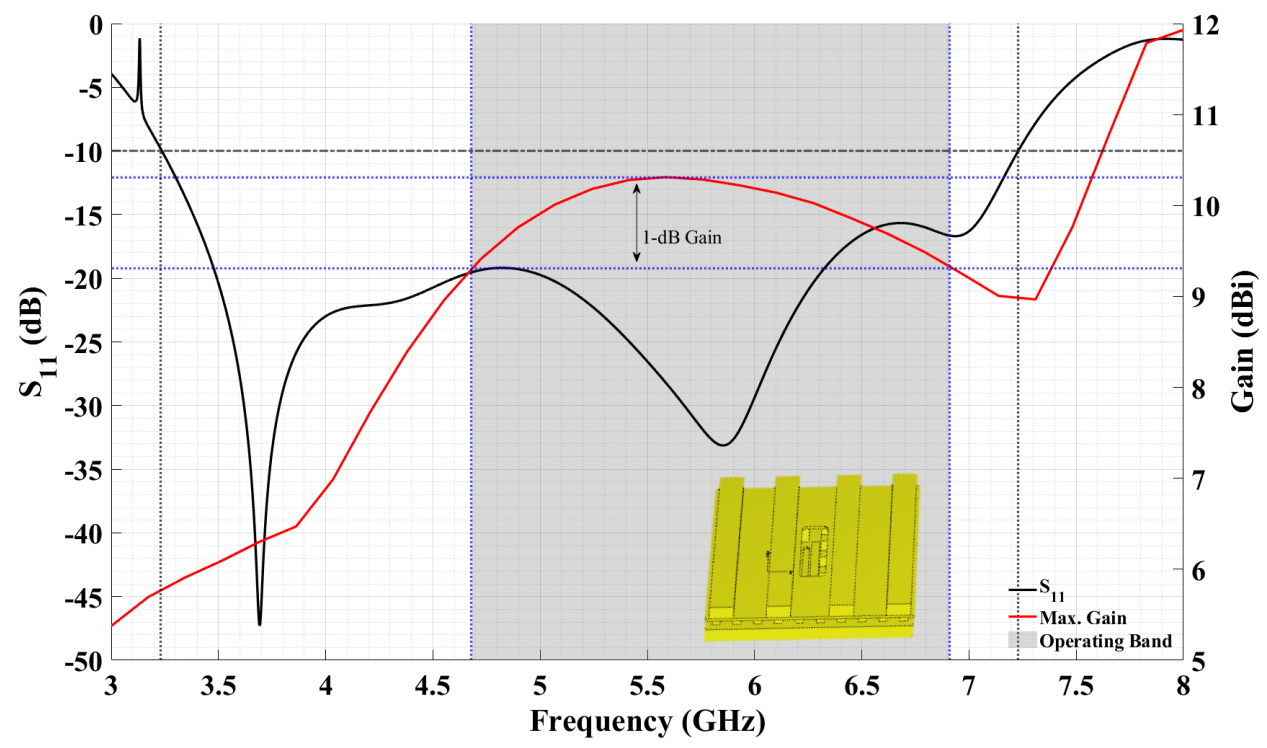


Figure 4.7. Simulated performance of the GGW slotted antenna with a step under the slot: S_{11} (black), and gain (red) over the 3–8 GHz range

The antenna's operating frequency bandwidth, visualized by the grey shaded area, spans from 4.7 GHz, where it is limited by the 1-dB gain bandwidth, up to 6.9 GHz. This results in an overall operating bandwidth of 38%.

Figure 4.8 presents the E-field distribution at 3.9 GHz, illustrating the electromagnetic field concentration within the stepped GGW structure. The E-field is strongest around the slot, step, and corrugations. This distribution confirms the effective radiation from the slot and the role of the step and corrugations in shaping the field pattern, further enhancing directivity and bandwidth.

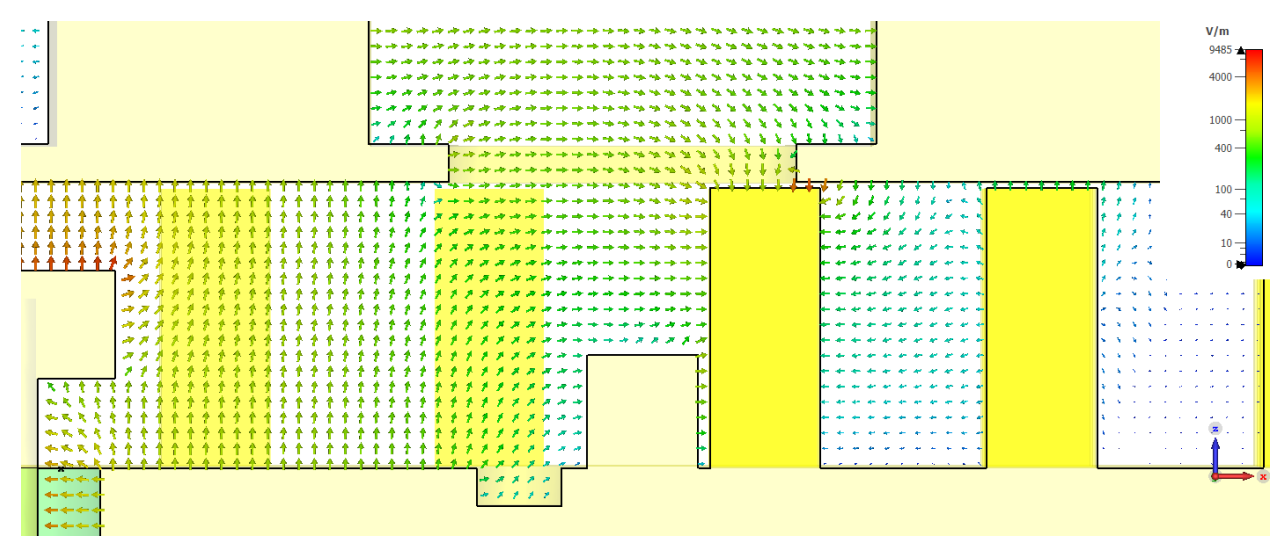


Figure 4.8. E-field distribution at 3.28 GHz for the stepped GGW slotted antenna with a step under the slot.

4.5. Comparison of Simple, Corrugated, and Stepped GGW Slotted Antennas

This section compares the performance of the simple single GGW slotted antenna (Section 04.2), the GGW slotted antenna with rectangular corrugations (Section 4.3), and the GGW slotted antenna with a step under the slot (Section 4.4) to assess the incremental improvements as shown in Figure 4.9.

The simple slot design achieves an $S_{11} < -10 \, dB$ bandwidth from 3.1 GHz to 4.6 GHz, resulting in a bandwidth of approximately 1.5 GHz, equivalent to a 38% impedance matching bandwidth. The corrugated design expands this range to 3.2–5.6 GHz, providing a 2.4 GHz bandwidth or a 54% impedance matching bandwidth. The stepped design further enhances this to a 77% impedance matching bandwidth, spanning 3.2–7.2 GHz, while maintaining the gain with no reduction and potentially improving matching across the range due to the step's influence on impedance, as demonstrated by the S_{11} results in Figure 4.7.

All designs exhibit gains of 5-10 dBi for the simple slot, 5.5–10.3 dBi for the corrugated design, and 5.5–10.3 dBi for the stepped design at their respective optimal frequencies, indicating that the step primarily enhances bandwidth without significantly altering gain.

All designs produce broadside radiation patterns with horizontal polarization. Still, the corrugated and stepped versions offer improved directivity, as shown in Figure 4.3 and Figure 4.7. The step does not substantially alter the radiation pattern but supports the broadband performance, as confirmed by the E-field distribution in Figure 4.8.

This comparison underscores the progressive enhancements: corrugations broaden the bandwidth and increase gain. At the same time, the step sustains this bandwidth at 77%, making the stepped GGW slotted antenna ideal for ultra-wideband applications in the 3.2–7.2 GHz range.

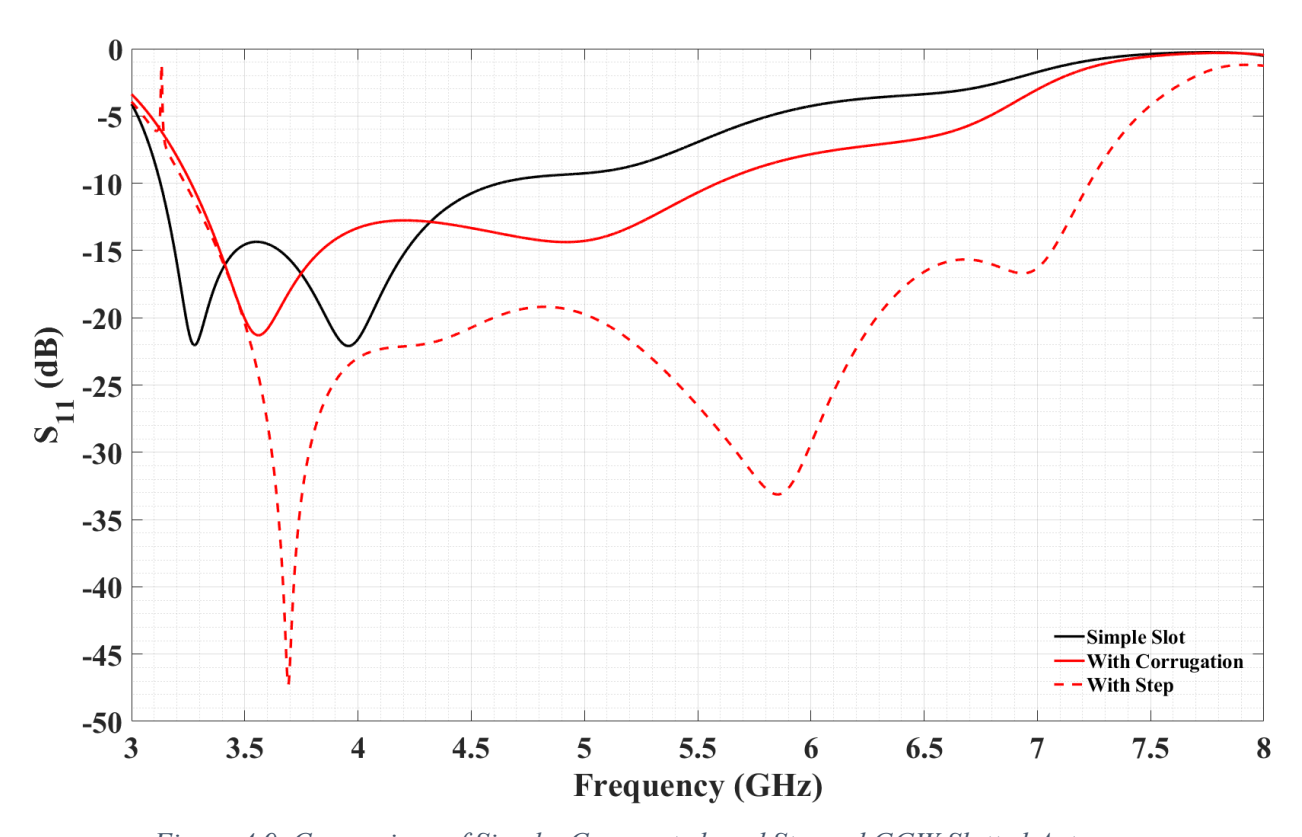


Figure 4.9. Comparison of Simple, Corrugated, and Stepped GGW Slotted Antennas

4.6. Prototyping and Measurement Results

During the prototyping of the stepped GGW slotted antenna, the specific size of the female SMA port used for the feeding mechanism necessitated adjustments to the antenna's dimensions to ensure proper integration and performance. These modifications, driven by the physical constraints of the SMA connector, resulted in revised dimensions for key components of the antenna, including the slot and step. The updated dimensions are detailed in Table 4.3:

Table 4.3. The dimensions of the Prototyped Antenna

Parameter	Description	Value (mm)	Parameter	Description	Value (mm)
a	Pin Size	5.88	d_g	Groove Depth	2
d	Pin Height	14.9	h_1	Height of the lower side	2.75
ag	Air Gap Size	0.3	h_2	Height of the upper side	11.5
p	Unit Cell Size	14.7	l_p	Plate Length	9.67
w	GGW Width	54	w_g	Groove Width	4.5
d_1	Distance to the Back wall	16	l_g	Groove Length	46
d_2	Distance to the transverse groove	27.05	t_p	Plate Thickness	10
d_3	Inner Pin's Center to the front wall	36.92	l_t	Upper layer Length	146.52
d_4	Slot's center to the front wall	4.65	t_t	Upper layer Thickness	2
w_r	Slot Width	18.5	w_t	Upper layer Width	120
l_r	Slot Length	46	h_c	Corrugation height	10
d_c	Slot center to Corrugation Center	22	w_c	Corrugation Width	17
p_c	Corrugation periodicity	40	d_s	Step's center to the front wall	2.94
h_s	Step Height	5	w_s	Step Width	5.88
l_s	Step Length	41.16	r_1	SMA Inner Conductor Radius	0.635
r_2	SMA Outer Conductor Radius	2.05			

Manufacturing Process

The proposed simple, corrugated, and stepped GGW slotted antennas were fabricated to validate the simulated performance in Section 4.4. The manufacturing process utilized high-precision CNC milling to ensure the accurate replication of design dimensions, particularly for the EBG pins, grooves, slot, corrugations, and step structures. Aluminum was selected as the primary material due to its high conductivity, lightweight properties, and suitability for high-frequency applications. The fabrication process involved the following steps.

Aluminum blocks were prepared with dimensions exceeding the final antenna size to accommodate machining tolerances. The blocks were polished to ensure a smooth surface finish, minimizing surface roughness that could affect electromagnetic performance. A 5-axis CNC machine was used to mill the lower plate, which includes the groove, EBG pins, and the step. The upper plate was milled to incorporate the transverse slot and rectangular corrugations. The slot dimensions and corrugation parameters were precisely machined according to Table 4.3.

A coaxial connector (SMA type) with an extended inner pin was integrated into the lower plate to facilitate the transition from the coaxial TEM mode to the GGW quasi-TE mode. The transition design followed the dimensions, with a probe inserted into the GGW to excite the quasi-TE mode. The probe and surrounding geometry were machined with sub-millimeter precision to minimize reflections.

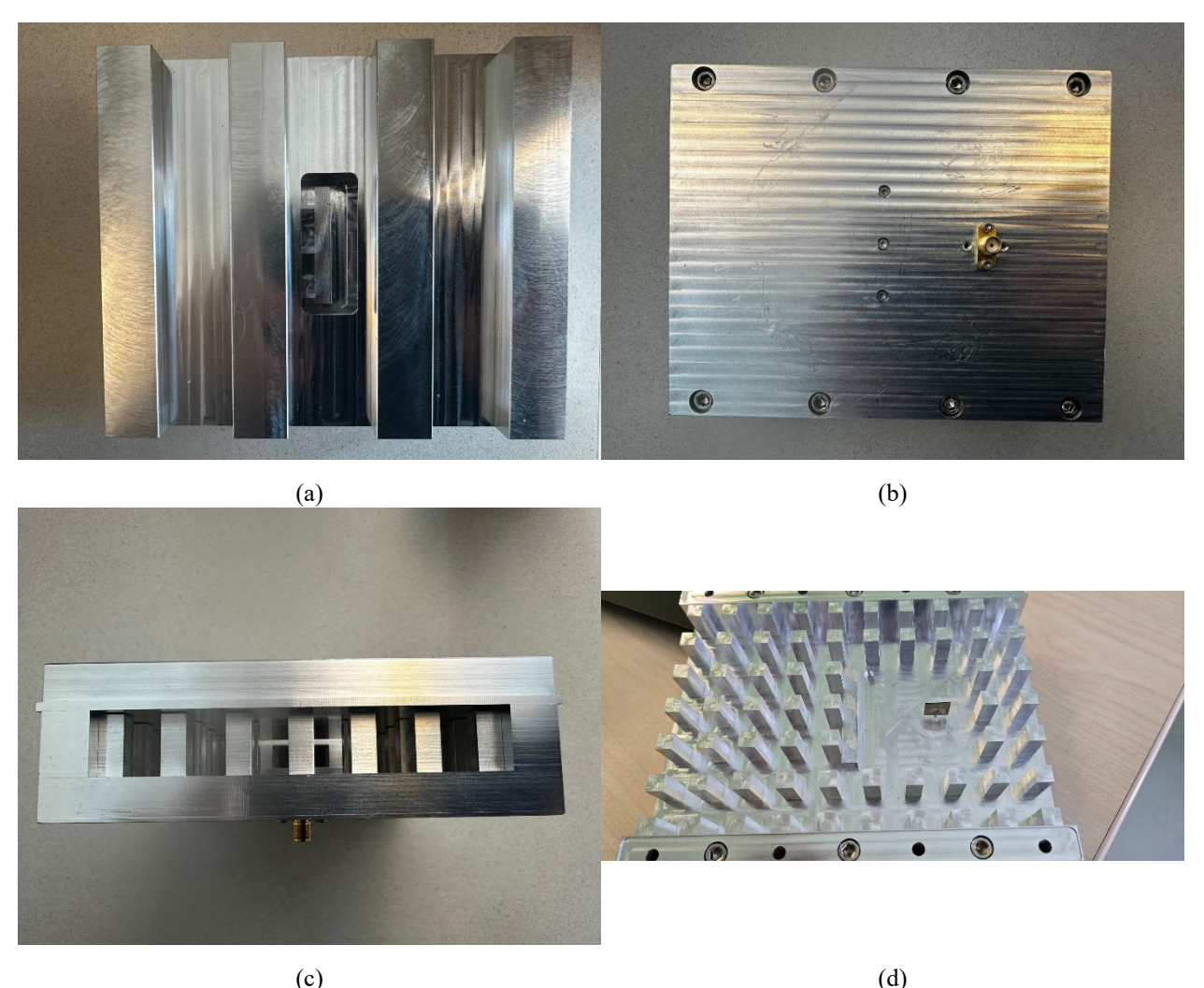


Figure 4.10. The Prototyped Antenna: (a) Top View (b) Bottom View (c) Side View (d) Disassembled Antenna

The assembly was secured with screws at the edges, ensuring structural stability without compromising electromagnetic performance. The fabricated components were inspected using a coordinate measuring machine (CMM) to verify dimensional accuracy. The fabrication process was optimized to strike a balance between precision and cost, making the design feasible for small-scale production while ensuring repeatability. Challenges included maintaining tight tolerances for the EBG pins and ensuring uniform air gap spacing, which were addressed through iterative machining adjustments and rigorous quality checks.

Measurement Setup

The fabricated antennas were tested in an anechoic chamber at Concordia University to measure their S_{11} and radiation patterns in the E-plane ($\phi = 90^{\circ}$) and H-plane ($\phi = 0^{\circ}$). The measurement setup included a Keysight N5227A PNA Microwave Network Analyzer, which was used to measure the S_{11} over the 3–8 GHz range. To ensure accuracy, the PNA was calibrated using an ECAL SOLT (Short-Open-Load-Thru) procedure. A shielded anechoic chamber was used to minimize reflections and external interference. The chamber was equipped with pyramidal absorbers rated for frequencies up to 40 GHz. A double-ridge horn antenna (ETS-3115) was used as the receiver antenna for radiation pattern measurements. The horn antenna was positioned 2.5 meters from the antenna under test (AUT) to ensure the far-field conditions were satisfied. A motorized turntable with 0.1° angular resolution was used to rotate the AUT for E-plane and H-plane pattern measurements. The turntable was controlled via software synchronized with the E8364B VNA for automated data collection. Measurements were conducted at three frequencies: 3.25 GHz, 5 GHz, and 7.25 GHz, selected to cover the operational bandwidth of the antennas, particularly the stepped design (3.2–7.2 GHz).

The AUT was connected to the VNA via a low-loss coaxial cable, and the setup was verified to ensure no cable-induced artifacts affected the measurements. Temperature and humidity were maintained at 23°C and 50%, respectively, to ensure consistent material properties.

Measurement Results

The measurement results for the stepped GGW slotted antennas are presented below, focusing on the S_{11} and the E-plane and H-plane radiation patterns at the specified frequencies.

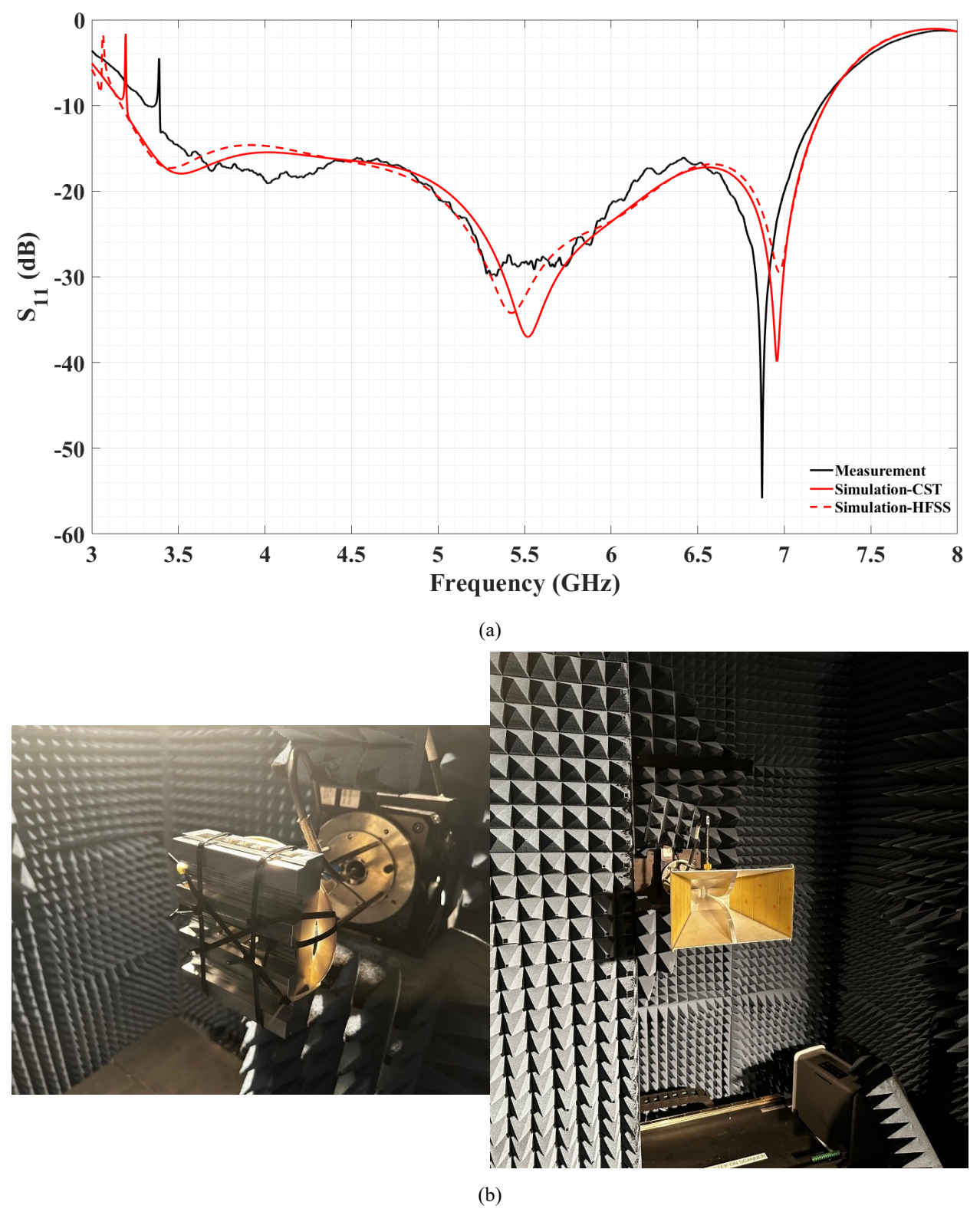


Figure 4.11. (a) Comparison of measured (blue line) and simulated (red line) S_{11} (b) The far-field setup of the radiation pattern measurement.

The results are compared with simulations to assess fabrication accuracy and real-world performance. Based on the provided plots in Figure 4.11 (a), the measured and simulated S_{11} for the stepped GGW slotted antenna are compared across the 3-8 GHz range. The measured \mathcal{S}_{11} (black line) and simulated S_{11} (red and dashed lines) exhibit a broad bandwidth, where for less than -10 dB, covering approximately 3.4-7.2 GHz for the measurement and 3.2-7.23 GHz for the CST simulation, aligning closely with the expected 72% impedance matching bandwidth. At lower frequencies (3–4 GHz), both plots show a dip below -20 dB, with the measured curve reaching a minimum around 4 GHz and the simulated curve slightly offset, indicating good agreement despite minor fabrication variations. Around 5.5 GHz, both curves show a noticeable dip, with the measured S_{11} dipping below -30 dB and the simulated plot following a similar trend, though the measured curve exhibits more fluctuation, possibly due to the cable or connector losses. At higher frequencies (6–8 GHz), the measured and simulated curves diverge slightly, with the measured S_{11} showing a sharper drop below -40 dB around 6.9 GHz, while the simulated curve remains above -30 dB, suggesting potential differences in high-frequency response due to machining tolerances or measurement setup. To validate the stepped GGW slotted antenna's performance, the E-plane ($\phi = 90^{\circ}$) and H-plane ($\phi = 0^{\circ}$) radiation patterns were measured and compared with simulations at 3.25, 5, and 7.25 GHz, spanning the 3.2–7.2 GHz bandwidth.

Figure 4.12 and Figure 4.13 present the normalized measured (red), simulated (black), and cross-polarization (red dashed) patterns. In Figure 4.12, the E-plane radiation pattern at 3.25 GHz displays a broadside configuration with dual lobes at $\pm 25^{\circ}$, a null at $\theta = 0^{\circ}$, a -2 dB gain level, and cross-polarization below -20 dB. At 5 GHz, the main beam shifts to $\theta = 0^{\circ}$, with cross-polarization reduced to below -30 dB. At the higher end of the frequency band, the main lobe tilts by 17°, likely due to the asymmetrical structure beneath the E-plane slot and its sensitivity to higher frequencies. In Figure 4.13, the H-plane pattern exhibits a wider beamwidth compared to the E-plane and maintains consistent alignment across the frequency band, attributed to the symmetrical structure in this plane. Discrepancies between simulated and measured patterns at angles beyond $\pm 70^{\circ}$ may result from antenna mounting conditions and the influence of absorbers. The close agreement between measured and simulated normalized patterns validates the stepped design's consistent broadside radiation across the bandwidth. Minor discrepancies are attributed to fabrication imperfections or measurement setup limitations.

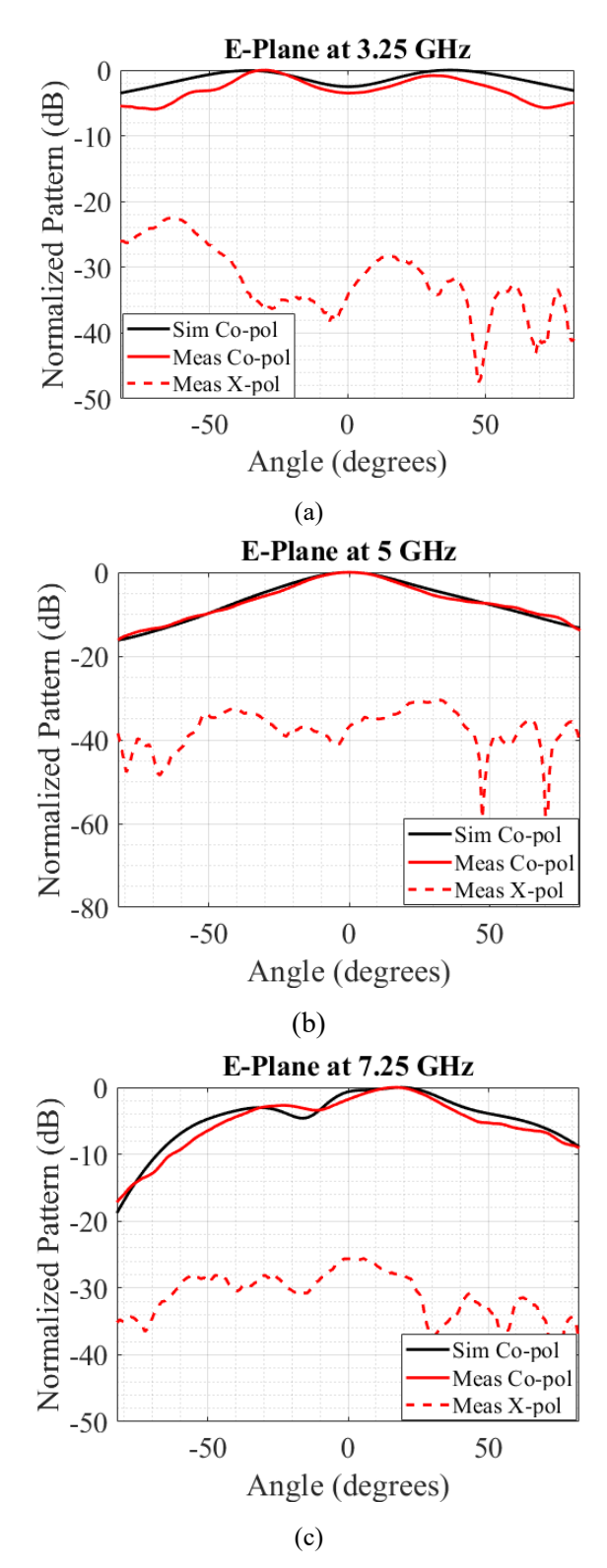


Figure 4.12. Comparison of Measurement and Simulation of E-Plane pattern at (a) 3.25 GHz, (b) 5 GHz, and (c) 7.25 GHz.

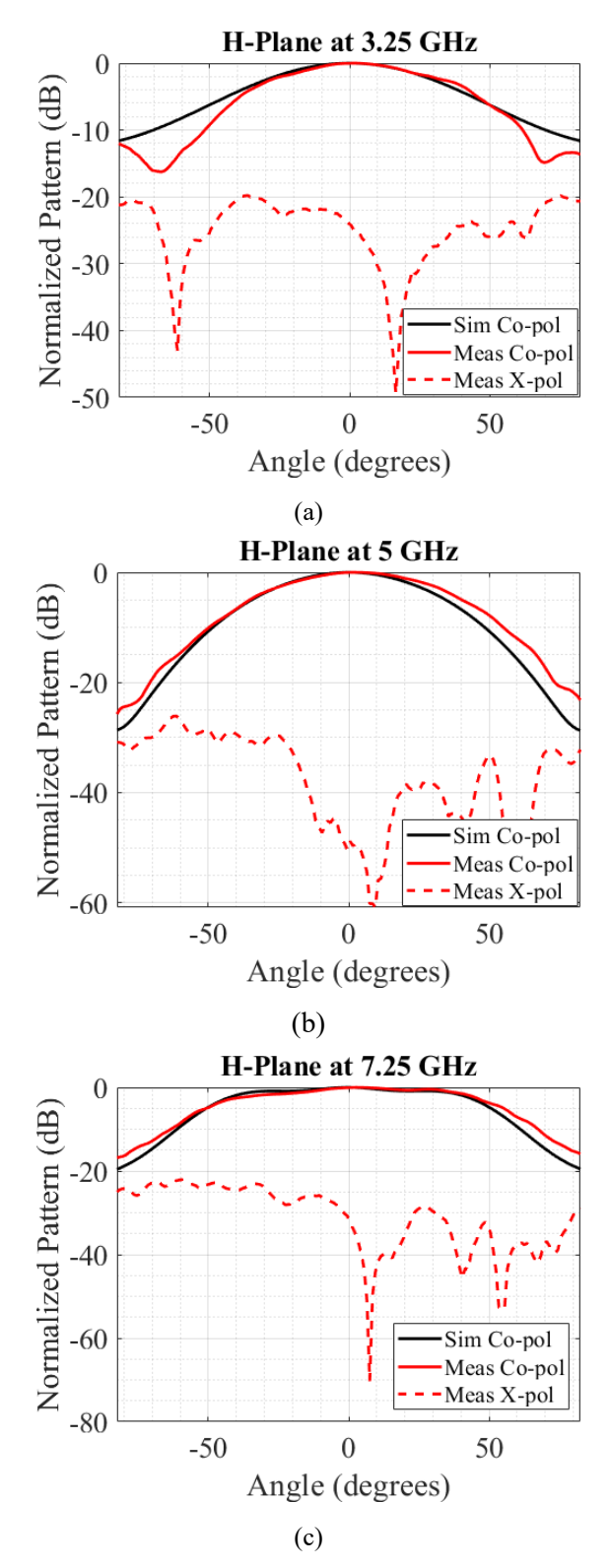


Figure 4.13. Comparison of Measurement and Simulation of H-Plane pattern at (a) 3.25 GHz, (b) 5 GHz, and (c) 7.25 GHz.

The investigation of GGW slotted antennas in this chapter demonstrates the potential of simple, corrugated, and stepped designs. The simple single GGW slotted antenna offers a narrowband, moderate-gain solution for the 3.1–4.6 GHz frequency range, while the addition of rectangular corrugations on the top layer significantly enhances the impedance bandwidth (3.2–5.6 GHz) and gain (10.3 dBi).

CST Studio simulations validate that introducing a step under the slot further improves the bandwidth to a 77% impedance matching bandwidth (3.2–7.2 GHz). The E-field distributions at 3.9 GHz (Figure 4.4 and Figure 4.8), cross-sectional views (Figure 4.1(b) Figure 4.2, and Figure 4.6), and radiation patterns in Figures Figure 4.4(a) and (b) provide visual and quantitative confirmation of the designs' effectiveness.

4.7. Design and Analysis of a 1x4 GGW Slotted Antenna Array with Stepped Design

This section extends the stepped GGW slotted antenna design presented in Section 4.4 to a 1x4 array configuration, enhancing the antenna's gain while preserving its wideband characteristics for sub-6 GHz applications. The array design utilizes the stepped GGW slotted antenna as the fundamental element, incorporating a standard one-to-four power divider feeding network with coaxial cables to ensure uniform power distribution and phase alignment, thereby improving radiation performance.

The 1x4 array comprises four identical stepped GGW slotted antennas, each with the dimensions and parameters specified in section 4.4. The elements are arranged linearly along the y-axis, with a uniform inter-element spacing of 59.88 mm, as shown in Figure 4.14. This spacing corresponds to slightly less than λ_0 at the center frequency of 5 GHz (within the 3.2-7.2 GHz bandwidth). While this spacing is less than the typical λ_0 range for minimizing grating lobes, it aligns with the design constraints. It ensures constructive interference in the broadside direction, with potential sidelobe considerations addressed in the performance analysis. Each antenna element retains the GGW structure with EBG pins, rectangular corrugations, and the step under the slot, preserving the 77% impedance matching bandwidth (3.2-7.2 GHz) observed in the single-element design to simulate the array antenna without the feeding network, all elements are simultaneously excited in CST Studio with an amplitude of 1 and a 0-degree phase, allowing the assessment of their mutual interactions and impact on the radiation pattern and gain.

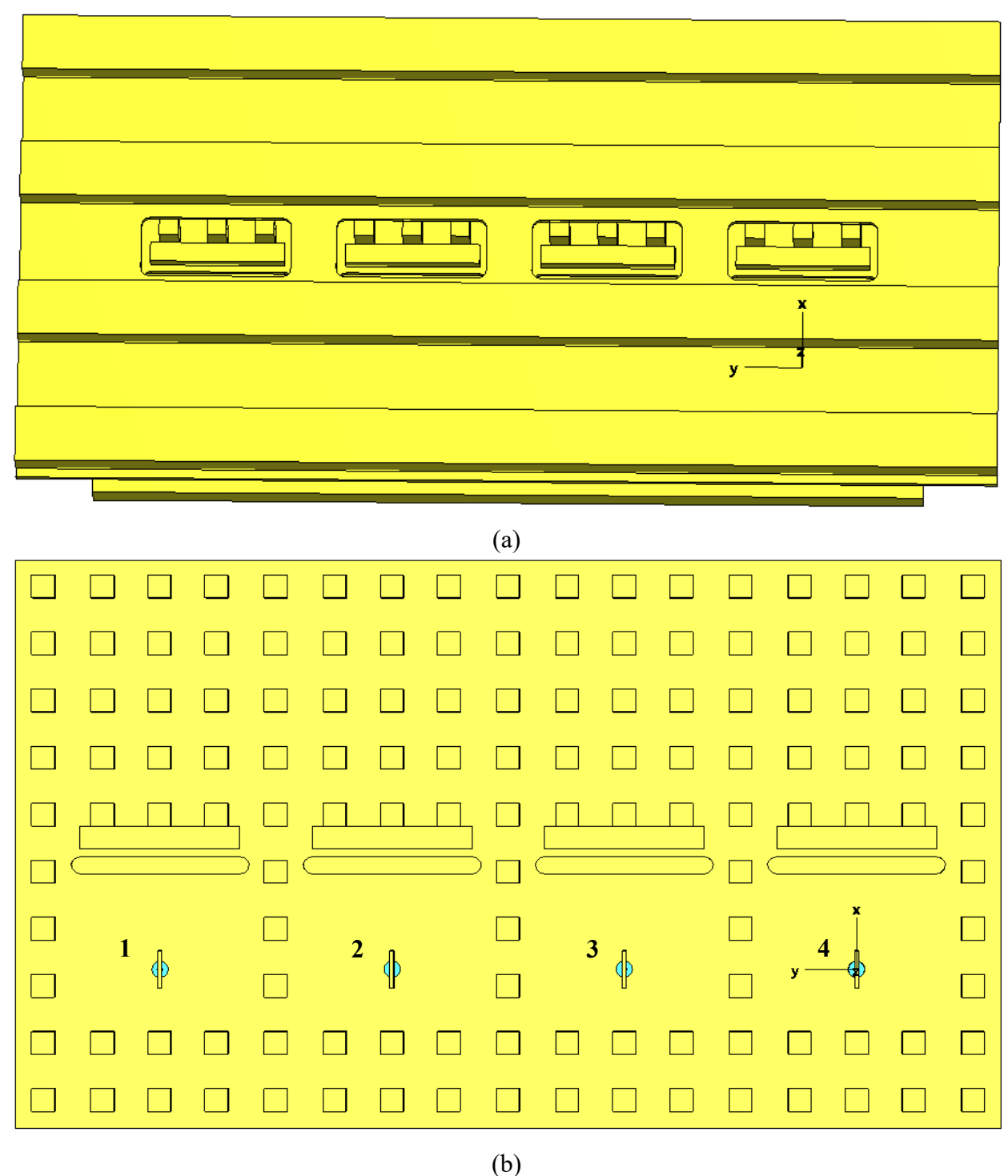


Figure 4.14.Simulated 1x4 array antenna a) Perspective view b) top view (hidden top layer)

In Figure 4.15, the plot illustrates the performance of the 1x4 array antenna, highlighting key characteristics across the frequency range of 3 to 8 GHz. As anticipated, the gain plot, depicted by

the black line, exhibits an increase of approximately 6 dB, reflecting the contribution of each pair of elements, which adds about 3 dB to the gain when optimally designed. The red line represents the active S_{11} for outer ports 1 and 4, maintaining values below -10 dB from 3.3 to 7.2 GHz, corresponding to a 74% impedance matching bandwidth, indicating excellent impedance matching across this range. In contrast, the red dashed line represents the active S_{11} for the inner ports 2 and 3, showing a slightly reduced impedance bandwidth of 3.3 to 7.1 GHz with values below -10 dB, covering 72% of the impedance bandwidth, suggesting a minor bandwidth reduction likely due to mutual coupling effects between the closely spaced elements. The antenna's operating frequency bandwidth, visualized by the gray shaded area in the plot, spans 30%. This range is constrained at its lower end by the 1-dB gain bandwidth, which is found at 4.77 GHz. Also, at the higher end, the limitation is set by the 1-dB gain bandwidth, occurring at 6.45 GHz.

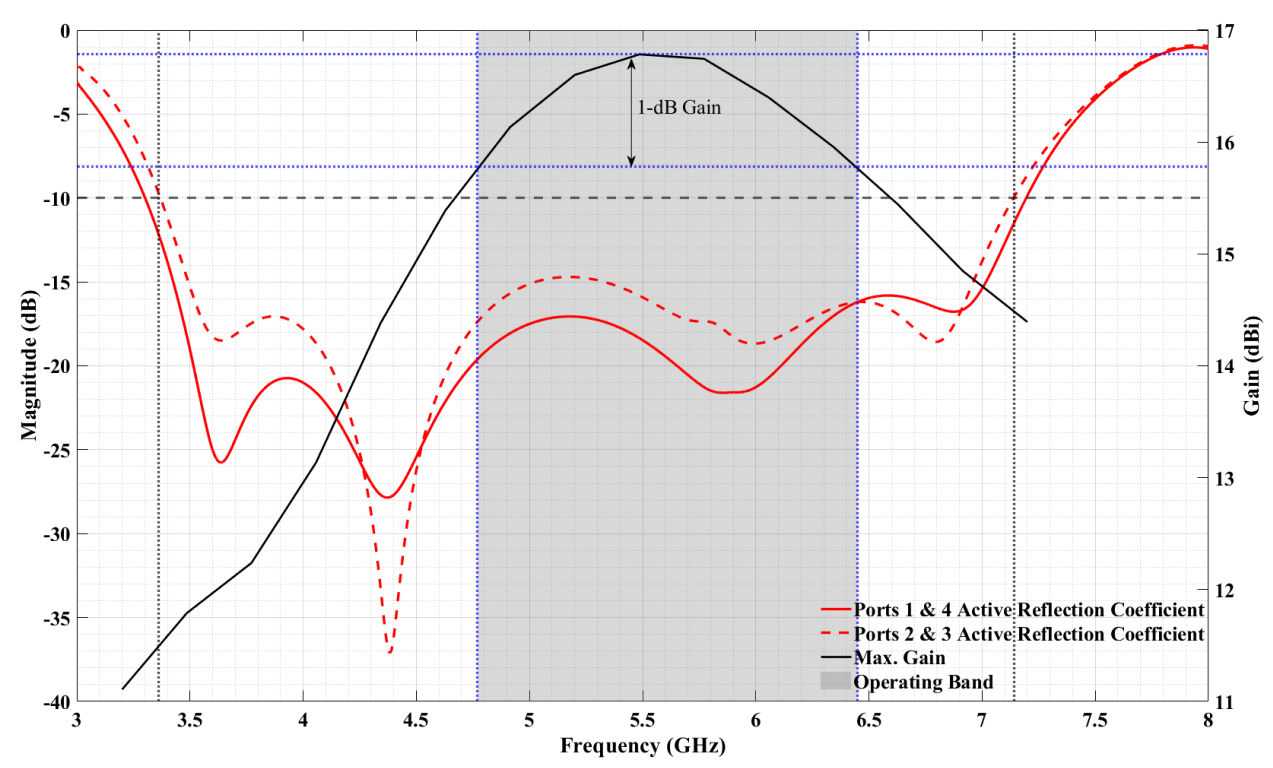


Figure 4.15. Active Reflection Coefficient and Gain versus frequency for the 1x4 Stepped GGW slot antenna simulated in CST

Table 4.4 presents a detailed comparison of the measured and simulated (CST) performance metrics for a single slot antenna and a 1x4 array configuration, both utilizing a stepped GGW feeding network. This table is pivotal in showcasing the effectiveness of the proposed antenna designs for sub-6 GHz applications, such as 5G communications and radar systems. For the single slot antenna, it lists parameters like impedance matching bandwidth, frequency range, 3dB

beamwidth, maximum gain, and the location of maximum radiation in E and H planes. The close agreement between simulated and measured results validates the accuracy of the simulation models and the precision of the fabrication process. The reason there is no maximum radiation location and a 3-dB beamwidth for the E-plane pattern at 3.25 GHz is that a null occurs at $\theta=0^{\circ}$ with a level of -3 dB, related to two lobes at $\pm 39^{\circ}$. This table underscores the array's ability to achieve higher directivity while retaining a broad operational bandwidth, highlighting its potential for high-gain, wideband applications and reinforcing the thesis's contribution to advancing antenna technology.

Table 4.4. Comparative results of Measured, Simulated (CST) Single Slot and 1x4 Array Antenna

	Impedance Matching Bandwidth	Frequency (GHz)	3dB-Beamwidth (H-Plane)	3dB-Beamwidth (E-Plane)	Max. Radiation Location (H- Plane/E-Plane)
Single Slot (Simulated)	77% (3.2-7.23 GHz)	3.25	66°	_	0°/-
		5	52°	45°	0°/0°
		7.25	90°	50°	0°/18.5°
Single Slot (Measured)	72% (3.4-7.2 GHz)	3.25	68°	_	0°/-
		5	59°	38°	0°/0°
		7.25	91°	42°	0°/17.5°
1x4 Slot Array (Simulated)	72% (3.4-7.1 GHz)	3.25	19°	22°	$0^{\circ}/0^{\circ}$
		5	12°	12.5°	0°/0°
		7.25	8°	8.7°	$0^{\circ}/0^{\circ}$

4.8. Scaling Analysis for Higher Frequencies

To explore the scalability of the stepped GGW slotted antenna, the design is scaled down to operate at higher center frequencies of 30 GHz and 60 GHz, maintaining the same impedance bandwidth. Figure 4.16 presents the S_{11} performance for two scaling factors: 0.17 (30 GHz) and 0.085 (60 GHz). The S_{11} curves, represented by red and black lines respectively, demonstrate that $S_{11} < -10 \, dB$ over bandwidths of approximately 18.9–42.5 GHz for the 30 GHz design and 37.8–85.1 GHz for the 60 GHz design, both maintaining the 77% impedance bandwidth observed in the original 3.2–7.2 GHz design.

This invariance in the bandwidth is attributed to the proportional scaling of all dimensions (slot, groove, corrugations, and step), preserving the electromagnetic behaviour across frequency bands. The consistency in bandwidth suggests that the stepped GGW design is highly scalable for

millimetre-wave applications, such as 5G or radar systems, without requiring a redesign of the bandwidth characteristics.

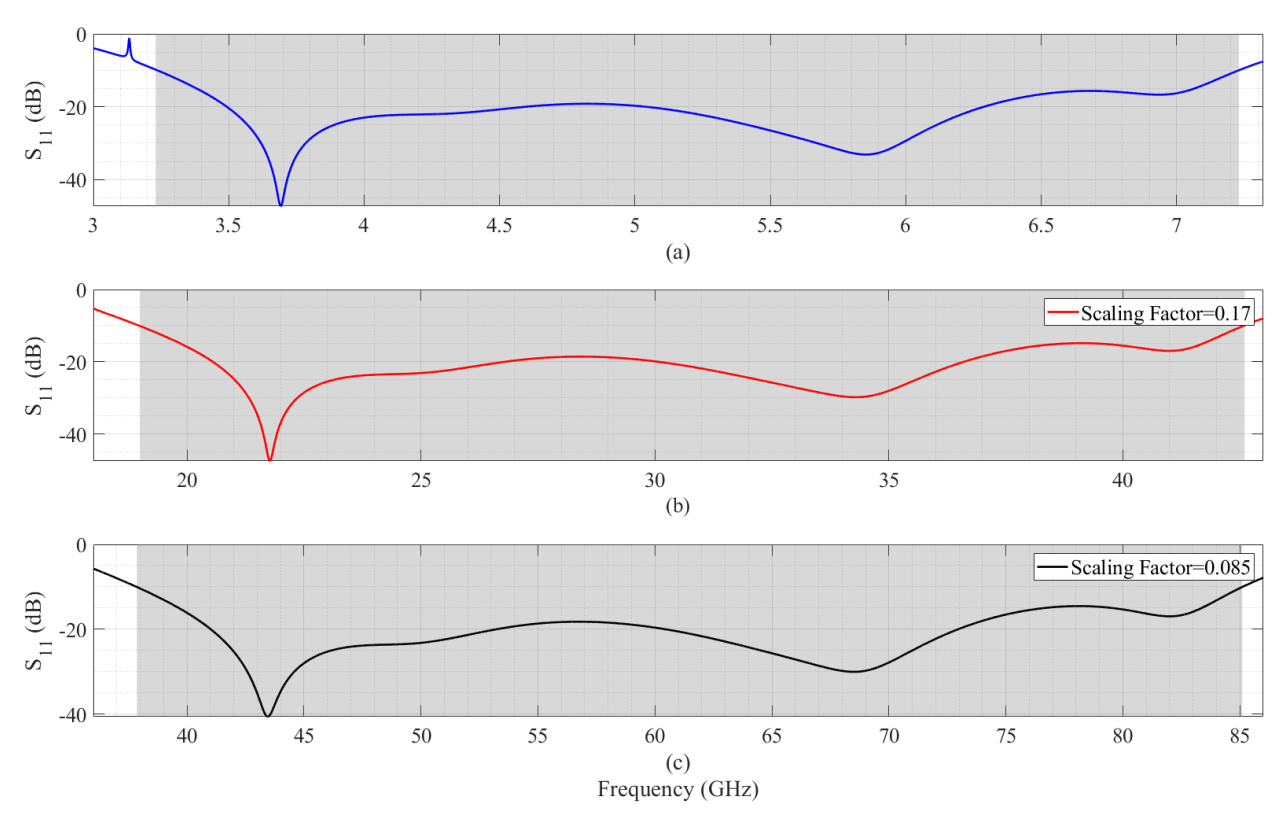


Figure 4.16. S₁₁ of the scaled GGW slotted antenna with a step under the slot, comparing b) scaling factors of 0.17 (red, 30 GHz center frequency) and c) 0.085 (black, 60 GHz center frequency), demonstrating invariant 77% impedance matching bandwidth

In Figure 4.17, the plot illustrates the performance of the 1x4 array antenna, scaled by a factor of 0.17 to operate at 30 GHz as expected. The red line represents the active S₁₁ for outer ports 1 and 4, maintaining values below -10 dB from 19.4 to 42.3 GHz, corresponding to a 74% bandwidth, which demonstrates effective impedance matching across this range. Conversely, the red dashed line represents the active S₁₁ for inner ports 2 and 3, a slightly reduced bandwidth of 19.8 to 42 GHz, with values below -10 dB, covering 71.8% of the bandwidth. This suggests a minor matching impedance bandwidth reduction, likely due to mutual coupling between the closely spaced elements. The antenna's operating frequency bandwidth, visualized by the gray shaded area in the plot, spans from 28 GHz, where it is constrained by the 1-dB gain bandwidth, up to 38.57 GHz, showing an overall operating bandwidth of 32.3%.

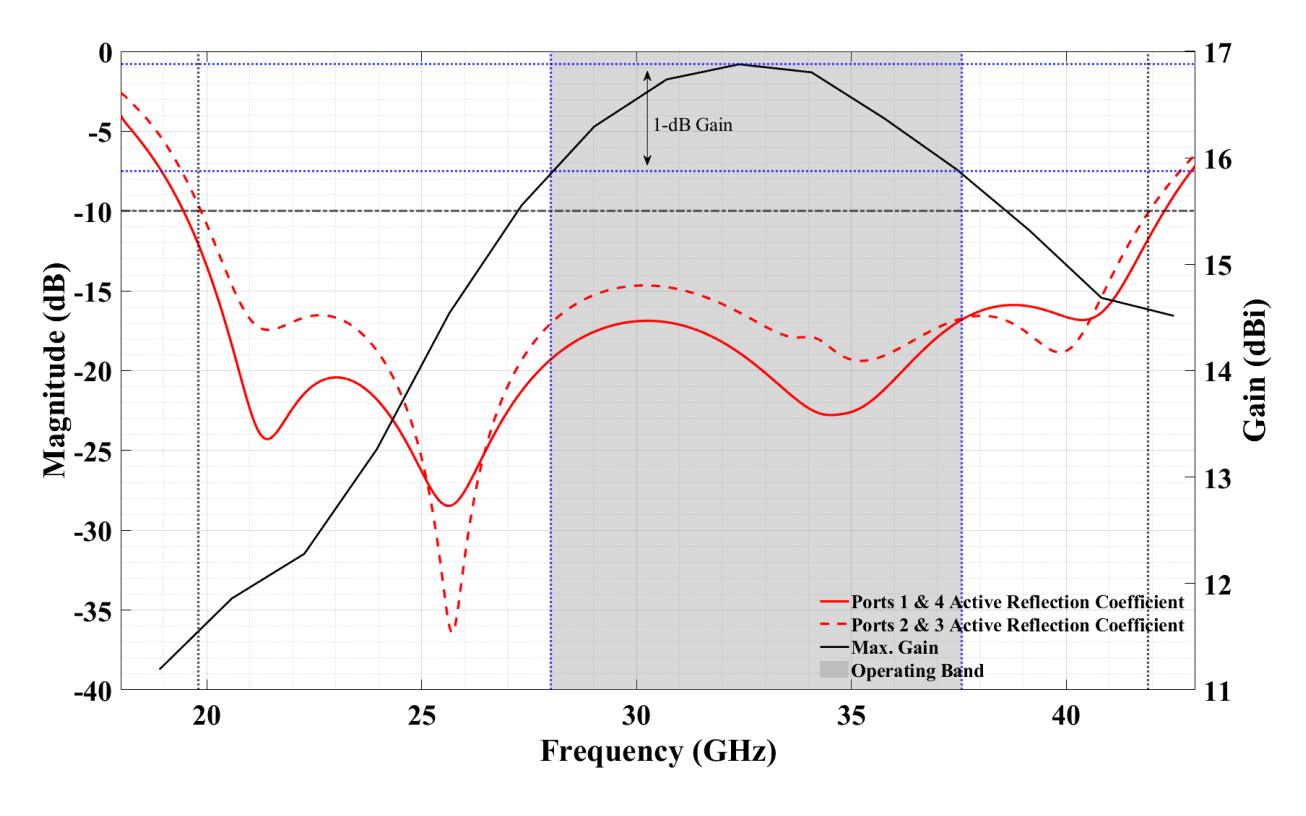
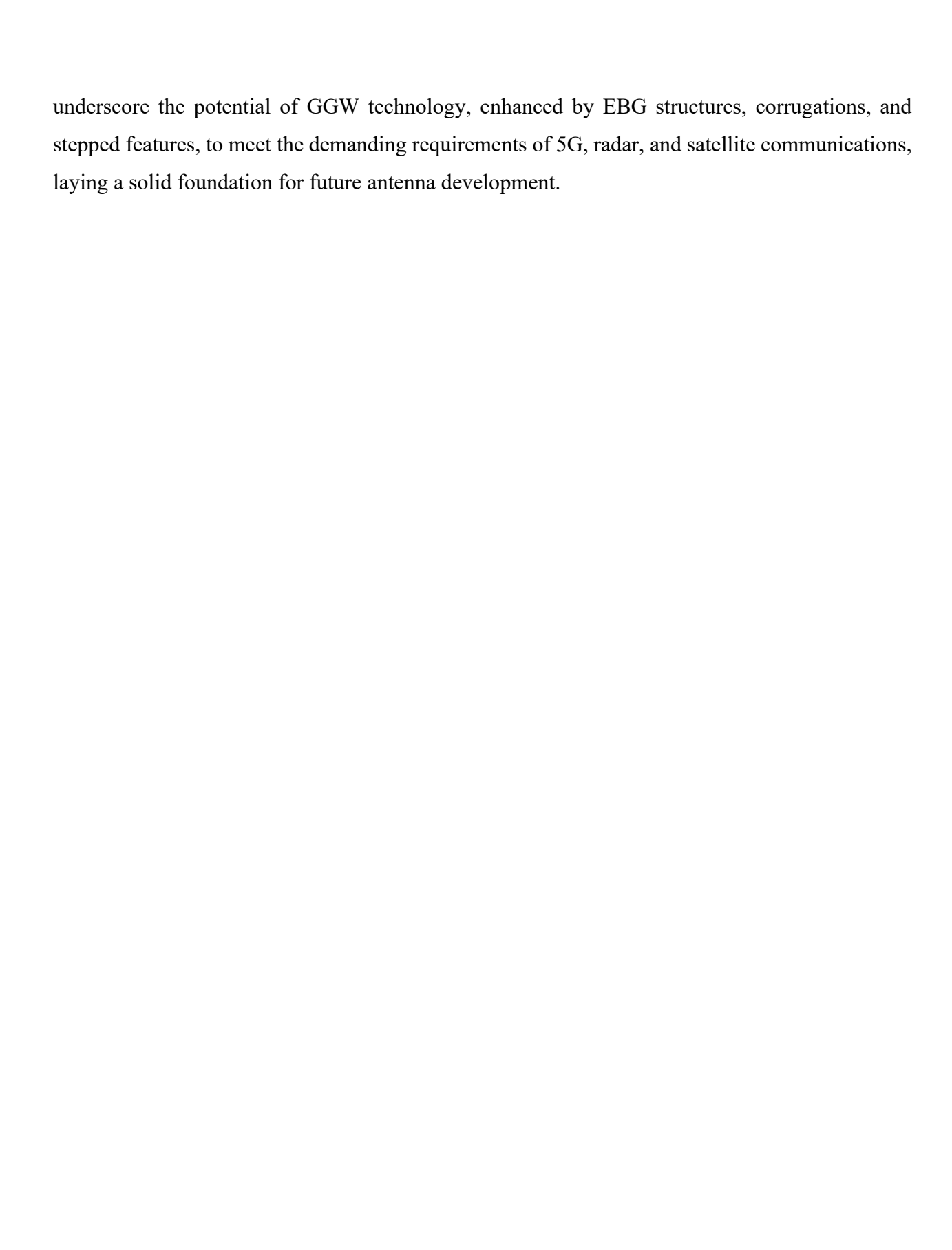


Figure 4.17. Active Reflection Coefficient and Gain versus frequency for the scaled 1x4 Stepped GGW slot antenna simulated in CST.

4.9. Conclusion

The investigations conducted in Chapter 4 have demonstrated the significant advancements achieved in the design and performance of transverse slot antennas using GGW technology. The progression from a simple single GGW slotted antenna, with a 38% bandwidth (3.1-4.6 GHz) and a gain of 7.5 dBi, to a corrugated design, expanding the bandwidth to 54% (3.2-5.6 GHz) with a gain of 10.3 dBi, highlights the effectiveness of rectangular corrugations in enhancing bandwidth and radiation efficiency. The introduction of a step under the slot further revolutionized the design, achieving a remarkable 77% impedance matching bandwidth (3.2-7.2 GHz) while maintaining a gain of 10.3 dBi, thereby addressing the critical needs of wideband applications. The stepped design was successfully prototyped and measured, with results closely aligning with CST Studio and HFSS simulations, confirming its robustness. Despite minor deviations due to fabrication tolerances, the matching impedance bandwidth remained strong at 73%. The extension to a 1x4 array configuration demonstrated a 6 dB gain increase and preserved the wideband characteristics, while scaling to 30 GHz and 60 GHz center frequencies retained the 77% impedance matching bandwidth, affirming the design's scalability for sub-6 GHz and MMW applications. These results



Chapter V:

Conclusion and Future Works

5.1. Conclusion

This thesis has demonstrated the potential of GGW technology in enhancing the performance of transverse slotted antennas for sub-6 GHz and MMW applications, particularly for 5G and beyond. The initial design of a simple single GGW slotted antenna, operating in the 3.1–4.6 GHz range, achieved a modest impedance matching bandwidth of 38%, with the highest gain of 10 dBi, establishing a baseline for further improvements. By incorporating rectangular corrugations on the top layer, the antenna's bandwidth was expanded to 54% (3.2–5.6 GHz), with a highest gain of 10.3 dBi, demonstrating enhanced directivity and radiation efficiency.

The introduction of a step under the slot at the GGW-to-slot transition marked a breakthrough, achieving a 77% impedance bandwidth (3.2–7.2 GHz) while maintaining the gain, thus addressing the critical need for wideband performance in modern communication systems. After successful fabrication and precise measurement, the antenna's matching impedance bandwidth was determined to be 73%, closely aligning with the initial simulation results. The scalability analysis further confirmed that this 77% impedance bandwidth is preserved when scaling the design to center frequencies of 30 GHz and 60 GHz, highlighting the versatility of the stepped GGW design for mm-wave applications such as 5G, radar, and satellite communications.

Simulations conducted using CST Studio and HFSS provided detailed insights into the antenna's S_{11} , gain, radiation patterns, and E-field distributions, validating the effectiveness of GGW technology, EBG structures, corrugations, and steps in mitigating challenges like narrow bandwidth, high path loss, and limited directivity. The contactless nature of GGW, combined with the suppression of surface waves through EBG structures, simplifies fabrication, reduces losses,

and enhances performance, making this approach a promising solution for next-generation wireless networks.

Overall, this research demonstrates that integrating GGW technology with advanced design modifications—such as corrugations and steps—offers a robust, scalable, and efficient platform for high-performance slotted antennas, significantly advancing the state-of-the-art antenna design for future communication systems.

5.2. Future Works

Building on the findings of this thesis, future research can enhance the performance and applicability of Groove Gap Waveguide (GGW) slotted antennas by exploring several key directions. Expanding the single-slot design into multi-element slotted arrays using GGW technology could focus on beamforming, mutual coupling reduction, and array factor optimization to achieve higher gains and steerable radiation patterns, which are suitable for massive MIMO systems and 5G/6G networks. Additionally, investigating hybrid beamforming techniques that combine sub-6 GHz and mm-wave bands could leverage the scalability of GGW slotted antennas to develop dual-band, dual-polarized designs, improving coverage, capacity, and spectral efficiency for next-generation networks. Furthermore, integrating advanced EBG structures, such as glide-symmetric holey designs or meta surfaces, and artificially soft or hard surfaces could further suppress surface waves, reduce mutual coupling, and enhance bandwidth and efficiency, particularly for compact, high-frequency antenna systems. These research avenues will address practical implementation challenges and broaden the applicability of GGW-based slotted antennas to meet the evolving demands of advanced wireless communication technologies.

References

- [1] R. Hussain *et al.*, "A Multiband Shared Aperture MIMO Antenna for Millimeter-Wave and Sub-6GHz 5G Applications," *Sensors*, vol. 22, no. 5, p. 1808, Feb. 2022, doi: 10.3390/s22051808.
- [2] Z. Huang, Z. Wang, and S. Chen, "Sub-6GHz Assisted mmWave Hybrid Beamforming With Heterogeneous Graph Neural Network," *IEEE Trans. Commun.*, vol. 72, no. 11, pp. 6917–6928, Nov. 2024, doi: 10.1109/TCOMM.2024.3405372.
- [3] M. Zada, I. A. Shah, and H. Yoo, "Integration of Sub-6-GHz and mm-Wave Bands With a Large Frequency Ratio for Future 5G MIMO Applications," *IEEE Access*, vol. 9, pp. 11241–11251, 2021, doi: 10.1109/ACCESS.2021.3051066.
- [4] K. Humadi, I. Trigui, W.-P. Zhu, and W. Ajib, "User-Centric Cluster Design and Analysis for Hybrid Sub-6GHz-mmWave-THz Dense Networks," *IEEE Trans. Veh. Technol.*, vol. 71, no. 7, pp. 7585–7598, Jul. 2022, doi: 10.1109/TVT.2022.3170518.
- [5] M. Shi, K. Yang, Z. Han, and D. Niyato, "Coverage Analysis of Integrated Sub-6GHz-mmWave Cellular Networks With Hotspots," *IEEE Trans. Commun.*, vol. 67, no. 11, pp. 8151–8164, Nov. 2019, doi: 10.1109/TCOMM.2019.2939802.
- [6] J. Kurvinen *et al.*, "Capacitively-Loaded Feed Line to Improve mm-Wave and Sub-6 GHz Antenna Co-Existence," *IEEE Access*, vol. 8, pp. 139680–139690, 2020, doi: 10.1109/ACCESS.2020.3012773.
- [7] B. Coll-Perales, J. Gozálvez, and M. Gruteser, "Sub-6GHz Assisted MAC for Millimeter Wave Vehicular Communications," *IEEE Communications Magazine*, vol. 57, pp. 125–131, Sep. 2018, doi: 10.1109/MCOM.2019.1800509.
- [8] M. Ostovarzadeh and S. Parizi, "Development of a compact transverse slot array antenna using corrugation in groove gap waveguide technology," *International Journal of Communication Systems*, vol. 36, Nov. 2022, doi: 10.1002/dac.5374.
- [9] Y. Quan, H. Wang, S. Tao, and J. Yang, "A Double-Layer Multibeam Antenna With 45° Linear Polarization Based on Gap Waveguide Technology," *IEEE Transactions on Antennas and Propagation*, vol. 70, pp. 56–66, Jun. 2021, doi: 10.1109/TAP.2021.3090507.
- [10] A. Farahbakhsh, D. Zarifi, and A. Zaman, "A mmWave Wideband Slot Array Antenna Based on Ridge Gap Waveguide With 30% Bandwidth," *IEEE Transactions on Antennas and Propagation*, vol. 66, pp. 1008–1013, Feb. 2018, doi: 10.1109/TAP.2017.2782263.
- [11] Z. Zang, A. Zaman, and J. Yang, "Single-Layer Dual-Circularly Polarized Series-Fed Gap Waveguide-Based Slot Array for a 77 GHz Automotive Radar," *IEEE Transactions on Antennas and Propagation*, vol. 71, pp. 3775–3784, May 2023, doi: 10.1109/TAP.2023.3243996.
- [12] M. Ebrahimpouri, E. Rajo-Iglesias, Z. Sipus, and O. Quevedo-Teruel, "Cost-Effective Gap Waveguide Technology Based on Glide-Symmetric Holey EBG Structures," *IEEE Trans. Microwave Theory Techn.*, vol. 66, no. 2, pp. 927–934, Feb. 2018, doi: 10.1109/TMTT.2017.2764091.
- [13] M. Ebrahimpouri, O. Quevedo-Teruel, and E. Rajo-Iglesias, "Design Guidelines for Gap Waveguide Technology Based on Glide-Symmetric Holey Structures," *IEEE Microwave and*

- Wireless Components Letters, vol. 27, pp. 542–544, May 2017, doi: 10.1109/LMWC.2017.2701308.
- [14] Z. Šipuš, M. Bosiljevac, and E. Rajo-Iglesias, "Higher symmetries in holey structures applied to gap waveguide technology: fundamentals and considerations," *2020 International Symposium on Antennas and Propagation (ISAP)*, pp. 585–586, Jan. 2021, doi: 10.23919/ISAP47053.2021.9391106.
- [15] Z. Liao, J. Zhang, X. J. Wang, F. Y. Yu, G. Luo, and L. Liu, "Topological State in Heterostructured Gap Waveguides and Their Transitions to Classical Transmission Line," *Laser & Photonics Reviews*, Oct. 2024, doi: 10.1002/lpor.202401284.
- [16] X.-H. Cheng, Z. Liu, Y. Yao, T. Yu, J. Yu, and X.-D. Chen, "Novel Band Gap Waveguide for Low-Loss and Dual Band Applications," *IEEE Transactions on Microwave Theory and Techniques*, vol. 70, pp. 2610–2621, May 2022, doi: 10.1109/tmtt.2022.3154747.
- [17] D. Sun, X. Chen, L.-X. Guo, W. Cui, and J. Deng, "Hard–Soft Groove Gap Waveguide Based on Perpendicularly Stacked Corrugated Metal Plates," *IEEE Transactions on Microwave Theory and Techniques*, vol. 69, pp. 3684–3692, Aug. 2021, doi: 10.1109/TMTT.2021.3086497.
- [18] Z. Šipuš, K. Ćavar, M. Bosiljevac, and E. Rajo-Iglesias, "Glide-Symmetric Holey Structures Applied to Waveguide Technology: Design Considerations †," *Sensors (Basel, Switzerland)*, vol. 20, Dec. 2020, doi: 10.3390/s20236871.
- [19] L. Liao, Y. Xiang, W. Wang, and W. Du, "Band Gap and Waveguide Characteristics of Petal-Shaped Scatterer Phononic Crystals," *The International Journal of Acoustics and Vibration*, Mar. 2023, doi: 10.20855/ijav.2023.28.11881.
- [20] P. Kildal and A. Kishk, "EM Modeling of surfaces with STOP or GO characteristics-artificial magnetic conductors and soft and," 2003, [Online]. Available: https://consensus.app/papers/em-modeling-of-surfaces-with-stop-or-go-kildal-kishk/ada7a52c4ef95eefad96c36c5ff72590/
- [21] R. Li, G. DeJean, M. Tentzeris, J. Papapolymerou, and J. Laskar, "Radiation-pattern improvement of patch antennas on a large-size substrate using a compact soft-surface structure and its realization on LTCC multilayer technology," *IEEE Transactions on Antennas and Propagation*, vol. 53, pp. 200–208, Jan. 2005, doi: 10.1109/TAP.2004.840754.
- [22] P. Kildal, "Artificially soft and hard surfaces in electromagnetics," *IEEE Transactions on Antennas and Propagation*, vol. 38, pp. 1537–1544, Oct. 1990, doi: 10.1109/8.59765.
- [23] E. Rajo-Iglesias, Ó. Quevedo-Teruel, and L. Inclan-Sanchez, "Mutual Coupling Reduction in Patch Antenna Arrays by Using a Planar EBG Structure and a Multilayer Dielectric Substrate," *IEEE Trans. Antennas Propagat.*, vol. 56, no. 6, pp. 1648–1655, Jun. 2008, doi: 10.1109/TAP.2008.923306.
- [24] M. K. Abdulhameed, M. S. M. Isa, Z. Zakaria, M. K. Mohsin, and M. L. Attiah, "Mushroom-Like EBG to Improve Patch Antenna Performance For C-Band Satellite Application," *IJECE*, vol. 8, no. 5, p. 3875, Oct. 2018, doi: 10.11591/ijece.v8i5.pp3875-3881.
- [25] Y. Rahmat-Samii and H. Mosallaei, "Electromagnetic band-gap structures: classification, characterization, and applications," vol. 2, pp. 560–564, Apr. 2001, doi: 10.1049/CP:20010350.

- [26] Y. Rahmat-Samii, "Electromagnetic band gap (EBG) structures in antenna engineering: From fundamentals to recent advances," 2008 Asia-Pacific Microwave Conference, pp. 1–2, Dec. 2008, doi: 10.1109/APMC.2008.4958195.
- [27] A. A. Hurshkainen *et al.*, "Element decoupling of 7 T dipole body arrays by EBG metasurface structures: Experimental verification," *Journal of Magnetic Resonance*, vol. 269, pp. 87–96, Aug. 2016, doi: 10.1016/j.jmr.2016.05.017.
- [28] A. Gandelli, F. Grimaccia, M. Mussetta, P. Pirinoli, and R. Zich, "New evolutionary algorithm for EBG materials optimization," vol. 5648, Feb. 2004, doi: 10.1117/12.582369.
- [29] M. Schuster *et al.*, "An interconnected 2D-TM EBG structure for millimeter and submillimeter waves," *IEEE J. Select. Areas Commun.*, vol. 23, no. 7, pp. 1378–1384, Jul. 2005, doi: 10.1109/JSAC.2005.851179.
- [30] B. Mouris, A. Fernández-Prieto, R. Thobaben, J. Martel, F. Mesa, and O. Quevedo—Teruel, "On the Increment of the Bandwidth of Mushroom-Type EBG Structures With Glide Symmetry," *IEEE Transactions on Microwave Theory and Techniques*, vol. 68, pp. 1365—1375, Jan. 2020, doi: 10.1109/TMTT.2020.2966700.
- [31] E. Rajo-Iglesias, M. Caiazzo, L. Inclán-Sánchez, and P. Kildal, "Comparison of bandgaps of mushroom-type EBG surface and corrugated and strip-type soft surfaces," *Iet Microwaves Antennas & Propagation*, vol. 1, pp. 184–189, Mar. 2007, doi: 10.1049/IET-MAP:20050327.
- [32] F. Caminita *et al.*, "Reduction of Patch Antenna Coupling by Using a Compact EBG Formed by Shorted Strips With Interlocked Branch-Stubs," *IEEE Antennas and Wireless Propagation Letters*, vol. 8, pp. 811–814, Apr. 2009, doi: 10.1109/LAWP.2009.2021589.
- [33] D. Margaret and B. Manimegalai, "Modeling and optimization of EBG structure using response surface methodology for antenna applications," *Aeu-international Journal of Electronics and Communications*, vol. 89, pp. 34–41, May 2018, doi: 10.1016/J.AEUE.2018.03.017.
- [34] R. Craster, T. Antonakakis, M. Makwana, and S. Guenneau, "Dangers of using the edges of the Brillouin zone," *Physical Review B*, vol. 86, p. 115130, Sep. 2012, doi: 10.1103/PHYSREVB.86.115130.
- [35] N. Roozen, L. Labelle, and C. Glorieux, "On the unwrapping of dispersion curves in the irreducible Brillouin zone by means of a spatial Fourier transform approach," *International Journal of Solids and Structures*, Jul. 2020, doi: 10.1016/j.ijsolstr.2020.03.016.
- [36] R. Assier, M. Touboul, B. Lombard, and C. Bellis, "High-frequency homogenization in periodic media with imperfect interfaces," *Proceedings. Mathematical, Physical, and Engineering Sciences*, vol. 476, Oct. 2020, doi: 10.1098/rspa.2020.0402.
- [37] J. Pérez-Escudero, A. Torres-García, R. Gonzalo, and I. Ederra, "A Gap Waveguide-Based Compact Rectangular Waveguide to a Packaged Microstrip Inline Transition," *Applied Sciences*, Jul. 2020, doi: 10.3390/app10144979.
- [38] D. Sun and J.-P. Xu, "Rectangular waveguide coupler with adjustable coupling coefficient using gap waveguide technology," *Electronics Letters*, vol. 53, pp. 167–169, Feb. 2017, doi: 10.1049/EL.2016.4039.
- [39] E. Rajo-Iglesias and P. Kildal, "Groove gap waveguide: A rectangular waveguide between contactless metal plates enabled by parallel-plate cut-off," *Proceedings of the Fourth European Conference on Antennas and Propagation*, pp. 1–4, Apr. 2010.
- [40] A. Berenguer, V. Fusco, M. Baquero-Escudero, and V. B. Esbert, "A frequency-dependent equivalence between groove gap waveguide and rectangular waveguide," 2016

- *IEEE International Symposium on Antennas and Propagation (APSURSI)*, pp. 1095–1096, Jun. 2016, doi: 10.1109/APS.2016.7696255.
- [41] A. Berenguer, V. Fusco, D. Zelenchuk, D. Sánchez-Escuderos, M. Baquero-Escudero, and V. Boria-Esbert, "Propagation Characteristics of Groove Gap Waveguide Below and Above Cutoff," *IEEE Transactions on Microwave Theory and Techniques*, vol. 64, pp. 27–36, 2016, doi: 10.1109/TMTT.2015.2504501.
- [42] B. Ashvanth, "Compact narrow slot antenna with stable radiation pattern and wide bandwidth," *Engineering Research Express*, Aug. 2024, doi: 10.1088/2631-8695/ad6fec.
- [43] S. Nawaz and W. Sethi, "Characteristic Mode Analysis Based Design of a Sub-THz Slotted Patch Antenna for High-Speed Wireless Communication Networks," *2024 International Conference on Engineering & Computing Technologies (ICECT)*, pp. 1–6, May 2024, doi: 10.1109/ICECT61618.2024.10581220.
- [44] A. Youssef, I. Halkhams, R. E. Alami, M. O. Jamil, and H. Qjidaa, "A novel slotted antenna design for future Terahertz applications," *International Journal of Electrical and Computer Engineering (IJECE)*, Jun. 2024, doi: 10.11591/ijece.v14i3.pp2708-2716.
- [45] A. Dastranj and H. Abiri, "Bandwidth Enhancement of Printed E-Shaped Slot Antennas Fed by CPW and Microstrip Line," *IEEE Transactions on Antennas and Propagation*, vol. 58, pp. 1402–1407, Jan. 2010, doi: 10.1109/TAP.2010.2041164.
- [46] A. Dastranj, A. Imani, and M. Naser-Moghaddasi, "Printed Wide-Slot Antenna for Wideband Applications," *IEEE Transactions on Antennas and Propagation*, vol. 56, pp. 3097–3102, Sep. 2008, doi: 10.1109/TAP.2008.929459.
- [47] S.-L. Chen, G. Wu, H. Wong, B. Chen, C. Chan, and J. Guo, "Millimeter-Wave Slot-Based Cavity Antennas with Flexibly-Chosen Linear Polarization," *IEEE Transactions on Antennas and Propagation*, vol. PP, pp. 1–1, 2022, doi: 10.1109/TAP.2022.3161313.
- [48] T. Neebha, S. Dhanasekar, P. Bruntha, A. Andrushia, R. Manjith, and S. Durga, "Analysis of Multilayered Antennas with Slotted Ground for Bandwidth Enhancement," 2021 7th International Conference on Advanced Computing and Communication Systems (ICACCS), vol. 1, pp. 604–607, Mar. 2021, doi: 10.1109/ICACCS51430.2021.9441806.
- [49] V. Rabinovich, B. Al-Khateeb, B. Oakley, and N. Alexandrov, "Experimental studies of printed wide-slot antenna for wide-band applications," *IEEE Antennas and Wireless Propagation Letters*, vol. 3, pp. 273–275, Dec. 2004, doi: 10.1109/LAWP.2004.837510.
- [50] Fadjrianah, Yohandri, and A. Munir, "Radiation Characteristics and Performance Evaluation of A Non-Uniform Slots SIW Antenna," 2023 IEEE International Symposium on Antennas and Propagation and USNC-URSI Radio Science Meeting (USNC-URSI), pp. 507– 508, Jul. 2023, doi: 10.1109/USNC-URSI52151.2023.10238110.
- [51] A. Mazzinghi, A. Freni, and M. Albani, "Influence of the Finite Slot Thickness on RLSA Antenna Design," *IEEE Transactions on Antennas and Propagation*, vol. 58, pp. 215–218, 2010, doi: 10.1109/TAP.2009.2027457.
- [52] H. Yun, D. Lee, and D. Kim, "Effective-zero-thickness terahertz slot antennas using stepped structures.," *Optics express*, vol. 29 14, pp. 21262–21268, Jun. 2021, doi: 10.1364/OE.427061.
- [53] M. Versluis, R. Schulpen, R. Budé, A. Smolders, and U. Johannsen, "Package Thickness Investigation of the U-Slot Patch Antenna for Beyond-5G Antenna-in-Package Applications," 2022 IEEE International Symposium on Antennas and Propagation and USNC-URSI Radio Science Meeting (AP-S/URSI), pp. 1046–1047, Jul. 2022, doi: 10.1109/AP-S/USNC-URSI47032.2022.9886312.

- [54] N. Hussain, K. Kedze, and I. Park, "Performance of a Planar Leaky-Wave Slit Antenna for Different Values of Substrate Thickness," *Journal of electromagnetic engineering and science*, vol. 17, pp. 202–207, Oct. 2017, doi: 10.26866/JEES.2017.17.4.202.
- [55] M. Teresa and G. Umamaheswari, "Compact Slotted Microstrip Antenna for 5G Applications Operating at 28 GHz," *IETE Journal of Research*, vol. 68, pp. 3778–3785, Jun. 2020, doi: 10.1080/03772063.2020.1779620.
- [56] M. A. P. Lazaro and R. Judaschke, "A 150-GHz CPW-fed tapered-slot antenna," *IEEE Microwave and Wireless Components Letters*, vol. 14, pp. 62–64, Feb. 2004, doi: 10.1109/LMWC.2003.822572.
- [57] J. Muldavin and G. Rebeiz, "Millimeter-wave tapered-slot antennas on synthesized low permittivity substrates," *IEEE Transactions on Antennas and Propagation*, vol. 47, pp. 1276–1280, Aug. 1999, doi: 10.1109/8.791943.
- [58] L. Zhang *et al.*, "Wideband 45° Linearly Polarized Slot Array Antenna Based on Gap Waveguide Technology for 5G Millimeter-Wave Applications," *IEEE Antennas and Wireless Propagation Letters*, vol. 20, pp. 1259–1263, Jul. 2021, doi: 10.1109/LAWP.2021.3077286.
- [59] M. Abbak, M. Akıncı, M. Çayören, and I. Akduman, "Experimental Microwave Imaging With a Novel Corrugated Vivaldi Antenna," *IEEE Transactions on Antennas and Propagation*, vol. 65, pp. 3302–3307, Feb. 2017, doi: 10.1109/TAP.2017.2670228.
- [60] A. Dixit, S. Kumar, S. Urooj, and A. Malibari, "A Highly Compact Antipodal Vivaldi Antenna Array for 5G Millimeter Wave Applications," *Sensors (Basel, Switzerland)*, vol. 21, Mar. 2021, doi: 10.3390/s21072360.
- [61] W. Thaiwirot, D. Kamoldej, P. Detchporn, P. Thongdit, and S. Tangwachirapan, "Design of Ultra-Wideband and Constant Gain Antipodal Vivaldi Antenna with Corrugations," *2022 International Electrical Engineering Congress (iEECON)*, pp. 1–4, Mar. 2022, doi: 10.1109/iEECON53204.2022.9741613.
- [62] S. Gupta, Z. Briqech, A. Sebak, and T. A. Denidni, "Mutual-Coupling Reduction Using Metasurface Corrugations for 28 GHz MIMO Applications," *IEEE Antennas and Wireless Propagation Letters*, vol. 16, pp. 2763–2766, Aug. 2017, doi: 10.1109/LAWP.2017.2745050.
- [63] Y. Jin, H. Lee, and J. Choi, "A Compact, Wideband, Two-Port Substrate-Integrated Waveguide Antenna With a Central, Double-Slotted, Metallic Plate Flanked by Two Paired of Corrugations for Radar Applications," *IEEE Transactions on Antennas and Propagation*, vol. 66, pp. 6376–6381, Nov. 2018, doi: 10.1109/TAP.2018.2863263.
- [64] S. Shams and A. Kishk, "Wideband Coaxial to Ridge Gap Waveguide Transition," *IEEE Transactions on Microwave Theory and Techniques*, vol. 64, pp. 4117–4125, Sep. 2016, doi: 10.1109/TMTT.2016.2610421.
- [65] R. Rossi and V. Gatti, "X-Band In-Line Coaxial-to-Groove Gap Waveguide Transition," *Electronics*, Jul. 2022, doi: 10.3390/electronics11152361.
- [66] A. Farahbakhsh, "Wideband Rotary Joint Based on Gap Waveguide Technology," *IEEE Transactions on Microwave Theory and Techniques*, vol. 69, pp. 4385–4391, Oct. 2021, doi: 10.1109/tmtt.2021.3090988.
- [67] A. Farahbakhsh, D. Zarifi, and A. Zaman, "60-GHz Groove Gap Waveguide Based Wideband \$H\$ -Plane Power Dividers and Transitions: For Use in High-Gain Slot Array Antenna," *IEEE Transactions on Microwave Theory and Techniques*, vol. 65, pp. 4111–4121, Jun. 2017, doi: 10.1109/TMTT.2017.2699680.

- [68] A. Pérez-Guimerá, M. Ferrando-Rocher, J. Herranz-Herruzo, and A. Valero-Nogueira, "Half-Mode Groove Gap Waveguide to Coaxial In-Line Transition for mm-Wave Applications," 2023 17th European Conference on Antennas and Propagation (EuCAP), pp. 1–3, Mar. 2023, doi: 10.23919/EuCAP57121.2023.10133760.
- [69] M. Simone, A. Fanti, M. Lodi, T. Pisanu, and G. Mazzarella, "An In-Line Coaxial-to-Waveguide Transition for Q-Band Single-Feed-Per-Beam Antenna Systems," *Applied Sciences*, Mar. 2021, doi: 10.3390/APP11062524.
- [70] S. Peng, Y. Pu, Z. Wu, X. Chen, and Y. Luo, "Embedded Bed of Nails With Robustness Suitable for Broadband Gap Waveguide Technology," *IEEE Trans. Microwave Theory Techn.*, vol. 69, no. 12, pp. 5317–5326, Dec. 2021, doi: 10.1109/TMTT.2021.3116178.
- [71] E. Rajo-Iglesias and P.-S. Kildal, "Numerical studies of bandwidth of parallel-plate cut-off realised by a bed of nails, corrugations and mushroom-type electromagnetic bandgap for use in gap waveguides," *IET Microw. Antennas Propag.*, vol. 5, no. 3, pp. 282–289, Feb. 2011, doi: 10.1049/iet-map.2010.0073.
- [72] E. Rajo-Iglesias, M. Ferrando-Rocher, and A. U. Zaman, "Gap Waveguide Technology for Millimeter-Wave Antenna Systems," *IEEE Commun. Mag.*, vol. 56, no. 7, pp. 14–20, Jul. 2018, doi: 10.1109/MCOM.2018.1700998.
- [73] Z. Shaterian, A. Horestani, and J. Rashed-Mohassel, "Design of slot array antenna in groove Gap waveguide technology," *IET Microwaves, Antennas & Propagation*, Feb. 2019, doi: 10.1049/IET-MAP.2018.5861.
- [74] H. Raza, J. Yang, P. Kildal, and E. Alfonso, "Resemblance between gap waveguides and hollow waveguides," *Iet Microwaves Antennas & Propagation*, vol. 7, pp. 1221–1227, Dec. 2013, doi: 10.1049/IET-MAP.2013.0178.
- [75] L. Herrán, A. A. Brazalez, and E. Rajo-Iglesias, "Ka-band planar slotted waveguide array based on groove gap waveguide technology with a glide-symmetric holey metasurface," *Scientific Reports*, vol. 11, Apr. 2021, doi: 10.1038/s41598-021-88054-5.
- [76] A. Polemi, E. Rajo-Iglesias, and S. Maci, "ANALYTICAL DISPERSION CHARACTERISTIC OF A GAP-GROOVE WAVEGUIDE," *Progress in Electromagnetics Research M*, vol. 18, pp. 55–72, 2011, doi: 10.2528/PIERM11020806.
- [77] W. Wang, Y. Lan, and Y. Wei, "The Analysis of Hole-Gap Helical Groove Waveguide," *International Journal of Infrared and Millimeter Waves*, vol. 21, pp. 1617–1625, Oct. 2000, doi: 10.1023/A:1006663626288.
- [78] R. Maaskant, P. Takook, and P. Kildal, "Fast analysis of gap waveguides using the characteristic basis function method and the parallel-plate Green's function," *2012 International Conference on Electromagnetics in Advanced Applications*, pp. 788–791, Oct. 2012, doi: 10.1109/ICEAA.2012.6328737.
- [79] H. Öztürk, "Wiener–Hopf approach for the coaxial waveguide with an impedance-coated groove on the inner wall," *Journal of Engineering Mathematics*, vol. 124, pp. 75–88, Sep. 2020, doi: 10.1007/s10665-020-10064-5.
- [80] J. Chen, D. Shen, X. Zhang, and Y. Sa, "Integrated substrate groove gap waveguide and application for filter design," *International Journal of RF and Microwave Computer-Aided Engineering*, vol. 31, Aug. 2021, doi: 10.1002/mmce.22830.
- [81] B. Zhang *et al.*, "A Novel Cruciform TE10/TE20 Dual-Mode Power Divider Based on Groove Gap Waveguides," *IEEE Transactions on Microwave Theory and Techniques*, vol. 71, pp. 5246–5256, Dec. 2023, doi: 10.1109/TMTT.2023.3280058.

- [82] A. Morales-Hernández, M. Sánchez-Soriano, M. Ferrando-Rocher, S. Marini, and V. Boria, "In-Depth Study of the Corona Discharge Breakdown Thresholds in Groove Gap Waveguides and Enhancement Strategies for Inductive Bandpass Filters," *IEEE Access*, vol. 10, pp. 129149–129162, 2022, doi: 10.1109/ACCESS.2022.3228111.
- [83] D. M. Pozar, *Microwave engineering*, Fourth edition. Hoboken, NJ: John Wiley & Sons, Inc, 2012.
- [84] I. Zhou, L. Jofre, and J. Romeu, "Technology Assessment of Aperture Coupled Slot Antenna Array in Groove Gapwaveguide for 5G Millimeter Wave Applications," *IEEE Access*, vol. PP, pp. 1–1, 2021, doi: 10.1109/ACCESS.2021.3119748.
- [85] S. Yan *et al.*, "A Wideband Gain-Enhanced Groove Gap Waveguide Slot Antenna Using Metal Pin Array," *IEEE Antennas and Wireless Propagation Letters*, vol. 23, pp. 159–163, Jan. 2024, doi: 10.1109/LAWP.2023.3320667.
- [86] S. Razavi and A. U. Zaman, "A Multi Beam Slot Array Antenna Fed by Contactless Multi-Layered 4×8 Buttler Matrix Using Gap Waveguide Technology for 60GHz Fixed Wireless Access Applications," 2023 17th European Conference on Antennas and Propagation (EuCAP), pp. 1–5, Mar. 2023, doi: 10.23919/EuCAP57121.2023.10133175.
- [87] T. Zhang, R. Tang, L. Chen, S. Yang, X. Liu, and J. Yang, "Ultra-wideband Full-metal Planar Array Antenna with a Combination of Ridge Gap Waveguide and E-plane Groove Gap Waveguide," *IEEE Transactions on Antennas and Propagation*, vol. PP, pp. 1–1, 2022, doi: 10.1109/tap.2022.3165655.